UNIVERSITY OF TRENTO

DOCTORAL THESIS

Brain-wide mapping of fMRI network dynamics in the mouse brain

Gutierrez Barragan, Daniel

Advisor: STEFANO PANZERI

Co-advisor: ALESSANDRO GOZZI

A thesis submitted in fulfilment of the requirements

for the degree of Doctor of Philosophy in the:

Doctoral School in Cognitive and Brain Sciences, University of Trento

Center for Neuroscience and Cognitive Systems,

Istituto Italiano di Tecnologia

12 April 2021

Abstract and declaration

DECLARATION

This dissertation is the result of my own work unless specifically indicated in the text as the outcome of a collaboration, or cited and acknowledged as material from another source. It has not been previously submitted, in part or whole, to any university of institution for any degree, diploma, or other qualification.

Signed:_____

Date:_____

Gutierrez Barragan, Daniel

University of Trento, Doctoral School in Cognitive and Brain Sciences

Istituto Italiano di Tecnologia, Center for Neuroscience and Cognitive Systems

Doctor of Philosophy

Brain-wide mapping of fMRI network dynamics in the mouse brain

DANIEL GUTIERREZ BARRAGAN

Intrinsic brain activity has been widely characterized using the blood-oxygen-level-dependent (BOLD) functional Magnetic Resonance Imaging (fMRI) at rest. There is increasing interest in finding reproducible and robust signatures of large-scale brain synchronization, and pinpointing their neurophysiological substrates and inherent alteration in disease. In this respect, the implementation of dynamic fMRI mapping in laboratory animals represents a major advance, offering the opportunity to unravel the elusive drivers of this phenomenon via the use of cell-type specific manipulations that are off limits in humans.

Multiple investigations have shown that spontaneous brain activity is non-stationary and involves reconfigurations into multiple dynamic states. This research describes a series of studies aimed to map spontaneous fMRI (rsfMRI) network dynamics in the resting mouse brain with voxel resolution. Starting from a proof-of-concept demonstration that canonical resting state fMRI correlations are reliably described by brief instances of regional peak fMRI activity, we devised a novel frame-wise clustering strategy that allowed us to map recurrent fMRI networks states dynamics in the mouse brain. We show that brain-wide patterns of fMRI co-activation can be reliably mapped at the group and subject level, defining a restricted set of recurring brain states characterized by rich network structure. Of particular interest was the observation of opposite co-activation of the mouse default mode network (DMN) and Latero-cortical networks (LCN), two systems that have been proposed to parallel analogous systems of the human brain. Importantly, we also document that these functional states are characterized by contrasting patterns of spontaneous fMRI activity, and exhibit coupled oscillatory dynamics embedded in a common temporal reference marked by infra-slow global fMRI signal oscillations. We next applied this novel framework to a genetic model of autism and show that aberrant patterns of fMRI connectivity in a genetic model of autism reflect the engagement non-canonical brain states, characterized by altered regional topography and oscillatory dynamics. We finally show that pharmacological stimulation of the cholinergic systems results in reduced large-scale brain synchronization, a finding associated with a new set of oscillating states in which the involvement of basal forebrain areas is predominant. Collectively, our results demonstrate the possibility of mapping spatio-temporal dynamics of spontaneous brain activity in the living mouse brain with voxel resolution. Our approach reveals a new set of fundamental principles guiding the spatiotemporal organization of resting state fMRI activity, and its disruption in brain disorders.

.

Acknowledgements

Science is hardly a one-person job. No part of this work was left without the participation of many people surrounding me during these years, either in Rovereto, or in the distance. To start, I would like to thank my advisors and mentors in this project, Stefano Panzeri and Alessandro Gozzi. Stefano, I will always carry important lessons learned throughout these years, and I am honored to have received your guidance. The integrity of your scientific endeavor and your team of highly talented individuals allowed me to engage research in a critical way and learn how diverse the field of computational neuroscience can be. Alessandro, your input and complementary guidance were truly a boosting factor throughout this project. I thank you for giving the opportunity to work amongst your team of truly wonderful individuals, a true demonstration of a synergetic laboratory in which all members complement each other scientifically, but also humanely. Working with both of you has greatly enriched me both professionally and personally, it was a unique experience but most importantly, I thank you for both your patience and the motivation you implanted.

To Alessandro Gozzi and his wonderful research team, thank you for letting me work amongst you. It was a privilege to work alongside such talented and collaborating people: Carola Canella, Alessia di Felice, Marco Pagani, Ludovico Coletta,, and Federico Rocchi, and also previous members: Adam Liska, Nayome Rey Calvo, Gergely David, Richard Gomolka, and Anna Askiuto. A great deal of appreciation goes to Alberto Galbusera for collecting all the datasets I worked with, and for teaching me with great patience the beautiful art of fMRI experimentation.

To my oversight committee, Jorge Jovicich and Uri Hasson, thank you for your critical input during this process, every meeting was a chance to grow professionally and scientifically. To the administrations of IIT and the doctoral school, many thanks for your kind support and patience while dealing with all the stupid questions I had. Leah Mercanti, Rosella Polli, Sara Maistrelli, and Paola Battistoni, thank you all, you made my life much easier.

To all my friends in CIMEC I want to extend my deepest appreciation. Ben, Srikant, Francesco, Evelyn, Luca, Matteo, Elena, and many more, thank you for your unconditional friendship, which I will always cherish.

To my parents, Maria Cristina and Fernando, my sister and brother, Kiss-kiss and Pipe, thank you for your continuous support. I saw you three times during this PhD, but we made each one count as a family.

I want to acknowledge the person who truly took care of me during these years. Marilina Matrogiuseppe, your innate talent for care giving and your spirited smiles are a relief to anyone who has had the privilege to meet you. Your support made me want to strive harder when under pressure. Your continuous encouragement alleviated many sorrows around, but specially, your humorous and enchanting character made my stay in Rovereto a wonderful experience. Let us do some science.

Contents

List of Figures

Nomenclature and Acronyms

ACg – Anterior Cingulate cortex

ALFF – Amplitude of Low-frequency Fluctuations

AUD – Auditory cortex

BF – Basal Forebrain

BOLD – Blood-Oxygen-Level-Dependent

CAP – Co-activation Pattern

CSF – Cerebrospinal Fluid

CPu – Caudate-Putamen

dFC – dynamic Functional Connectivity

DG – Deoxyglucose

DMN – Default-Mode Network

dHCP – Dorsal Hippocampus

DTI – Diffusion Tensor Imaging

EEG – Electroencephalography

fALFF – Fractional Amplitude of Low-frequency Fluctuations

FC – Functional Connectivity

FDR – False-discovery Rate

fMRI – functional MRI

GM – Grey Matter

GS – Global fMRI Signal

HCP – Hippocampal Network

HT – Hypothalamus

ILA – Infra-Limbic area

LAN – Lateral Amygdalar Nucleus

LCN – Latero-cortical Network

LFP – Local Field Potentials

MEG – Magnetoencephalography

MOp – Primary Motor area

MOs – Secondary Motor area

MRI – Magnetic Resonance Imaging

NB – Nucleus Basalis

NBM – Nucleus Basalis of Meynert

ORB – Orbitofrontal cortex

PET – Positron Emission Tomography

PIR – Piriform Area

PL - Pallidum

PLN – Postero-lateral Network

PPA – Point-process Analysis

PSD – Power Spectral Density

Rs – Retrosplenial cortex

rsfMRI – Resting State fMRI

RSN – Resting State Network

SB-CAP – Seed-based CAP

SD – Standard Deviation

SEM – Standard Error of the Mean

SNR – Signal-to-noise Ratio

SS – Somato-sensory cortex

SSp – Primary Somato-sensory cortex

SSs – Secondary Somato-sensory cortex

ST - Striatum

SWC – Sliding-window Correlations

TeA – Temporal Association area

TH – Thalamus

TPN – Task-positive Network

vHPC – Ventral Hippocampus

Veh - Vehicle

VIS – Visual cortex

VSD – Voltage Sensitive Dye

WM – White Matter

Xan - xanomeline

Chapter 1

Introduction

1.1 Motivation for my research

One of the most exciting challenges science faces today is the understanding of the basic principles that govern human brain function. This multidisciplinary endeavor has called upon massive collaborative initiatives such as the Human Brain Project[1] in Europe and the NIH's BRAIN[2] initiative in the United States, which are accelerating at a never-before seen pace the development and application of technologies to shed light into the most fascinating inquiries regarding brain function and its alterations in disease. Specialist in diverse fields of science and medicine are each day producing invaluable knowledge that bridges gaps in the spatial and temporal scales of brain function, leading to better understanding of its organization in health and disease.

Neuroscience is amongst the most multi-faceted research fields, bringing together a broad spectrum of domains such as biology, medicine, physics, mathematics, psychology, engineering, philosophy, chemistry, amongst many others. Recent years have brought forth unprecedented advances in neuroimaging methods to map brain activity. As part of these efforts, functional Magnetic Resonance Imaging (MRI) has emerged as a dominant method to study brain structure and function at rest, and upon administration of tasks. Large-scale

[1] https://www.humanbrainproject.eu
[2] https://braininitiative.nih.gov/

initiatives such as The Human Connectome Project [3] and The 1000 Connectomes Project[4] constitute ambitious data-sharing initiatives aimed to unravel the fundamental mechanisms of brain communication and to deliver novel tools and practices to brain researchers (Glasser et al., 2016), while promoting the sharing of data through standardized platforms. As more and more neuroimaging datasets are being collected, theoretical and experimental domains come into play to generate and empirically test novel hypotheses as to the organization of brain function at multiple levels.

Animal models offer a unique window of opportunity to investigate mechanisms of brain function and address complex questions. With multimodal neuroimaging approaches in animal models, brain function can be investigated and manipulated via genetic, molecular, or optogenetic interventions. The use of these techniques in translational research has been successful in establishing basic principles that cannot be directly observed in the human brain, and address questions regarding the nature and significance of brain (dys)function that cannot be answered by the research paradigms currently employed in humans.

My work during the PhD involved the development of an analytical approach to study whole-brain spontaneous network dynamics in the living mouse brain with voxel resolution, using resting-state functional Magnetic Resonance Imaging (rsfMRI) data. By doing so, I have discovered a new set of principles guiding spontaneous fMRI dynamics, and its breakdown in brain connectopathies. In this Chapter, I will briefly introduce some key concepts our research stands upon, as well as recent advances in the field of fMRI network dynamics. I will also introduce the main research questions addressed in our research, and their relevance to the neuroscientific community.

[3] http://www.humanconnectomeproject.org/
[4] http://fcon_1000.projects.nitrc.org/

1.2 Background literature.

Neuroimaging methods.

The nervous system can be studied with widely different spatio-temporal resolution. **Figure 1.1** summarizes the capacity of some of the most commonly employed methods for neural investigation. Neural activity can be inferred from single intra-cellular recordings to full brain images using readouts that are sensitive to neural activity per se, or that rely on indirect proxies for neuronal function. The emergence of non-invasive neuroimaging modalities in the past decades, such as Electroencephalography (EEG) and fMRI, has allowed researchers to non invasively map the functional organization of the human brain.

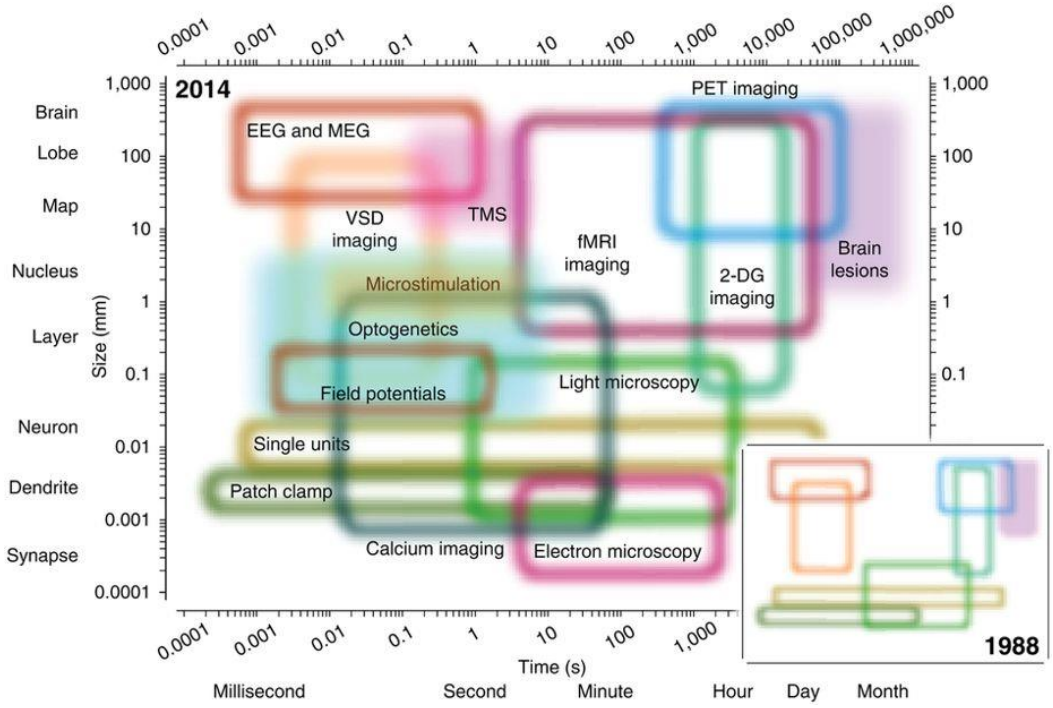

Figure 1.1: The spatial and temporal domains of available methods to study the nervous system by 2014. Each region represents a method or technique and its estimated temporal and spatial resolution. Filled regions represent perturbation methods, and open regions represent data acquisition techniques. The inset represents the estimated spatial and temporal resolution depiction of the limited available techniques by 1988. Abbreviations: EEG - electroencephalography; MEG – magnetoencephalography; PET – positron emission tomography; VSD – voltage-sensitive dye; TMS – transcranial magnetic stimulations; 2-DG – 2-deoxyglucose. From (Sejnowski et al., 2014).

As depicted in **Figure 1.1**, EEG-based mapping offers high temporal resolutions allowing to measure activity at all frequencies of neural firing, but suffers from low spatial resolution, (Abreu et al., 2018; Huster et al., 2012). EEG also lacks sensitivity to record activity from deeper brain regions where most subcortical structures are located (Jackson and Bolger, 2014).

MRI is a neuroimaging technique that leverages the magnetic resonance properties of hydrogen nuclei in water molecules and their response to spatial magnetic gradients to map and differentiate types of soft matter in the brain (white matter, grey matter, cerebro-spinal fluid) (Gore, 2003). MRI can produce high-resolution structural images of the brain and describe its anatomical organization with outstanding versatility. MRI is also widely used to study brain function by using fast sequences that can acquire whole-brain images as a subject undergoes a certain cognitive paradigm or task. fMRI studies make use of the so-called Blood-Oxygen-Level-Dependent (BOLD) contrast as an indirect measure of brain activity (Bandettini et al., 1992; Logothetis et al., 2001; Ogawa et al., 1990). The BOLD effect is a cascade of metabolic events ignited by the energetic demands of local neural activity. As blood delivers oxygen to provide the energy for neural functioning, the local changes in concentration of deoxygenated blood results in an increase in the MRI signal in that specific brain region (Buxton, 2012). Repeated acquisitions of MR images can track relative changes in MRI signals caused by these metabolic gradients, mapping indirectly neural activity (Ogawa et al., 1990). The major advantage of this neuroimaging modality is its capacity to record whole brain images with sub-millimetre resolution in both cortical and deep subcortical regions. On the other hand, fMRI is characterized by low temporal resolution, and the fact that the acquired functional signal is an indirect proxy for neural activity (Logothetis, 2008; Logothetis et al., 2001). Despite these limitations, experimental and theoretical efforts have begun to shed light onto the biophysical mechanisms of the BOLD signal generation and their physiological relevance (Havlicek et al., 2015; Logothetis and Wandell, 2004).

Resting state fMRI and intrinsic brain dynamics

In the last two decades, fMRI has revolutionized cognitive neuroscience, permitting to test the neuroanatomical and functional substrates of diverse cognitive functions (Poldrack, 2012) via the implementation of “task-based” fMRI (Lindquist, 2008; Logothetis, 2008). However, in

the absence of task or stimuli, the brain at rest is continuously active (Buckner et al., 2008), and the energy consumption of the observed ongoing spontaneous fluctuations of neural activity accounts for energy consumption levels comparable to those observed under a cognitive task (Raichle, 2015). Spontaneous neural activity is continuously present in the brain and persists across physiological states (Buzsáki and Draguhn, 2004; Mohajerani et al., 2010). There is therefore an increasing interest in understanding the baseline activity of the brain at rest, and how information is shared amongst brain regions in "task-free" conditions (Raichle, 2015).

In humans, whole-brain patterns of intrinsic brain activity are typically mapped by measuring spontaneous BOLD signals in the resting brain (Power et al., 2014; Yeo et al., 2011), an approach termed resting-state fMRI (rsfMRI) (Biswal et al., 1995; Fox and Raichle, 2007). A large body of experimental work has shown that spontaneous low-frequency fluctuations in fMRI signals are temporally synchronous across multiple functional systems, delineating a set of reproducible topographies known as resting-state networks (RNSs), which can be reliably identified also in primates (Vincent et al., 2007) and rodents (Gozzi and Schwarz, 2016). In the brain imaging field, second-order statistical relationships between signals are typically referred to as "functional connectivity" (FC), a parameter that is often employed as in indirect index of brain synchronization.

Spontaneous low-frequency fluctuations of BOLD signals have long been assumed to be co-variance stationary. However, several studies have demonstrated otherwise (Calhoun and Adali, 2016; Chang and Glover, 2010; Hutchison et al., 2013; Preti et al., 2017). Indeed, accumulating evidence of FC fluctuations in time (Hutchison et al., 2013; Keilholz, 2014) suggests that a comprehensive understanding of large-scale network activity could be reached by further studying dynamic connectivity patterns arising from time-varying correlations. Indeed, information processing in the brain is a highly dynamic process, which requires a tight balance between segregation and integration (Deco et al., 2015). Electrophysiology and theoretical models suggest that large-scale spontaneous neural dynamics is constrained by structural connections, significantly fluctuates at short time-scales, and these fluctuations conform a rich repertoire of coupling states that are recurrent (Breakspear, 2017; Cabral et al., 2017a; Deco et al., 2015).

The assessment of time-varying changes in coherent interregional brain activity from rsfMRI BOLD readouts can be done using different strategies and methodologies, each with inherent advantages and pitfalls. **Figure 1.** presents a summary of the most common methods employed so far (Preti et al., 2017). The use of sliding-window correlations (SWC) represents the most commonly employed method so far. Briefly, this approach entails the computation of interregional Pearson correlations between BOLD time-series within a time-window that is shifted by specific time-steps. This generates so-called dynamic Functional Connectivity (dFC) time-courses for each pair of regions, and produces a connectivity matrix including all pairs of connections for each time-step. These matrices are then clustered and dFC states defined (Allen et al., 2014). Variations of this method include computing instantaneous synchrony either by multiplication of temporal derivatives between time-courses (Shine et al., 2015), or by computing the cosine of the instantaneous phase differences (using the Hilbert transform of filtered time-courses) between signals (Glerean et al., 2012). While largely popular, SWC suffers from the need of defined window-length and shift-length, as well as susceptibility to signal-to-noise ratio (SNR) that can spuriously induce FC fluctuations (Hindriks et al., 2016; Kudela et al., 2017). In addition, brain parcellations are commonly used to reduce dimensionality in the time-varying connectivity matrices, precluding a genuine voxel-wise description of time varying fMRI activity (Hutchison et al., 2013; Liu et al., 2013).

An alternative approach to the investigation of time-varying brain dynamics was proposed based on the observation that spontaneous brain activity may be driven by brief instances of simultaneous activation of various brain regions (Liu and Duyn, 2013; Tagliazucchi et al., 2012). This observation implies that key information about the dynamic structure of resting state activity can be retrieved from individual fMRI volumes (Tagliazucchi et al., 2016, 2012). Based on this notion it was proposed that whole-brain patterns of recurrent BOLD activity could be described by either retaining fMRI frames corresponding to a region's highest BOLD activity and observing recurrent patterns, or by clustering the complete set of frames into recurring whole-brain patterns of BOLD activity (Karahanoğlu and Van De Ville, 2015; Liu et al., 2013). These clustered frames would be then averaged into co-activation patterns (CAPs) (Liu et al., 2013).

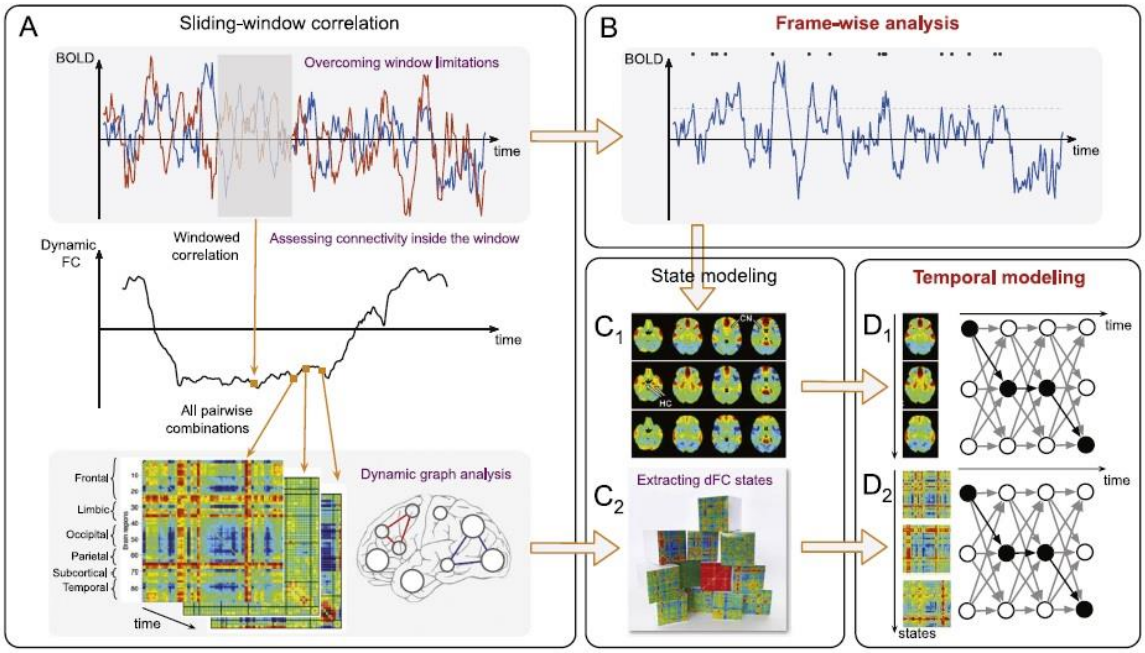

Figure 1.2: Methods to assess time-varying brain rsfMRI dynamics. (A) Sliding-window correlations assesses interregional Pearson correlations between BOLD time-series within a time-window that shifts at specific time-steps. This generates dynamic Functional Connectivity (dFC) time-courses for each pair of regions, and produces a connectivity matrix including all pairs of connections for each time-step. These matrices are then clustered and dFC states defined (Allen et al., 2014). (B) Frame-wise analyses can be done either by retaining fMRI frames corresponding to a region's highest BOLD activity, or by clustering the complete set of frames into recurring whole-brain patterns of BOLD activity. (C) Either the selected fMRI frames or the whole set can be clustered to generate voxel-wise brain states (C1), or co-activation patterns (CAPs) (Liu et al., 2013; Liu and Duyn, 2013) from the averaged samples in each cluster. (C2) dFC matrices can also be clustered into dFC states of similar structure. Temporal characteristics and interactions of recurrent CAPs (D1) or dFC states (D2) can be further inferred, and state trajectories described. From (Preti et al., 2017).

While the above-mentioned class of methods have begun to shed light on the organization of non-stationary rsfMRI dynamics, a precise characterization of how network states interact and dynamic brain reconfigurations occur is lacking. Are spontaneous network transitions organized stochastically, or do they reflect a set of recurring default states? And what are the fundamental principles by which brain-wide patterns of spontaneous fMRI activity reconfigure and interact with each other?

Studying fMRI brain dynamics in animal models

The path towards a greater mechanistic understanding of fMRI dynamics implies the use of model organisms amenable to neural manipulations. The availability of genetically modified

models of many brain disorders, and the strict control over genetic and environmental variability achievable in the mouse make this species a privileged tool to study alterations in brain dynamics associated to brain disorders and the effect of pharmacological treatments (Gozzi and Schwarz, 2016; Jonckers et al., 2015; Keilholz et al., 2017; Liska and Gozzi, 2016). In recent years, reliable detection of RSNs recapitulating anatomical features found in human and primates have been described in the mouse brain using static FC (Jonckers et al., 2015; Liska et al., 2015; Nasrallah et al., 2014; Sforazzini et al., 2014; Zerbi et al., 2015). **Figure 1.3** shows the results of graph-theoretical analyses of voxel-wise fMRI FC, revealing neuro-anatomically distributed networks of synchronous spontaneous brain activity (Liska et al., 2015). Several recent studies have further shown that rodents FC topographies are affected by etiologies associated with human disorders(Jonckers et al., 2015; Liska et al., 2017; Liska and Gozzi, 2016; Sforazzini et al., 2016). Importantly, using sliding-window correlations and dictionary learning, a recent study identified dFC states in a cohort of wildtype mice, showing the presence of functional dynamic states and specific changes in dFC strength in mice undergoing chronic psychosocial stress (Grandjean et al., 2017). The application of dFC methods to rsfMRI in mice may open new avenues towards the description of large-scale dynamic connectivity alterations associated to specific gene mutations, and the elucidation of the neural drivers of spontaneous network reconfiguration.

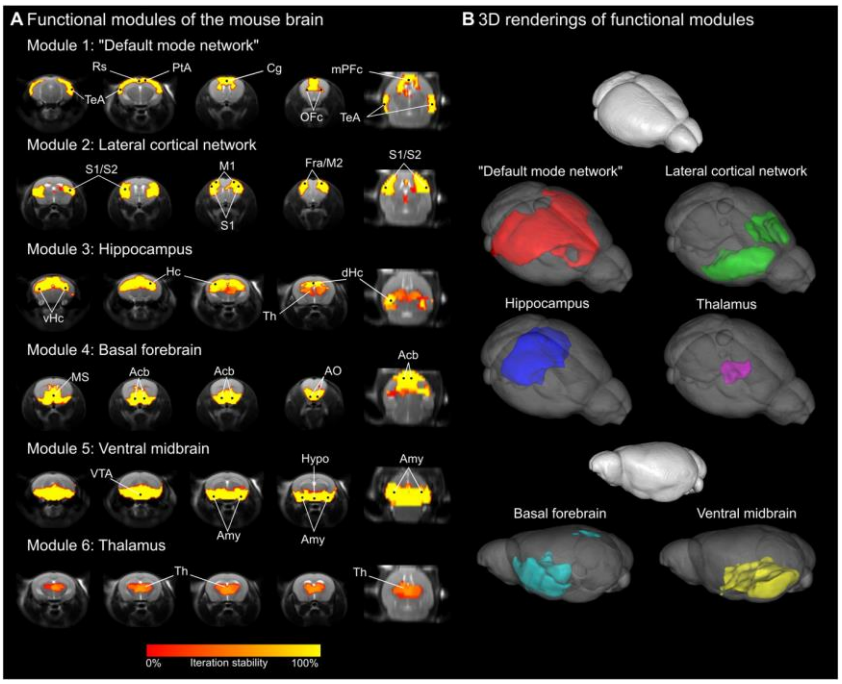

Figure 1.3: Resting state functional modules of the mouse brain. (A) Module stability maps after 100 iterations of a modularity algorithm in n=41 wildtype mice. (B) Representation of modules in a three-dimensional rendering. From (Liska et al., 2015).

Animal models provide a unique window of opportunity to investigate specific genetic variations observed in brain disorders in humans. Resting-state network organization as measured from rsfMRI BOLD signal acquisitions has been proven to be an evolutionary conserved characteristic also observed in the non-human primates (Vincent et al., 2007) and rodents (Gozzi and Schwarz, 2016; Jonckers et al., 2015; Keilholz et al., 2017; Liska and Gozzi, 2016). The pertinent use of genetically controlled species can help disambiguate the complex origin and implications of brain disorders having rsfMRI patterns of brain activity as endophenotypes expressing characteristic features of these disorders (Gozzi and Schwarz, 2016).

1.3 Thesis outline and main contributions.

The present work had three main goals: to design a sound methodological framework to study whole-brain network dynamics in the mouse brain from rsfMRI readouts; to test the sensitivity of the method to detect non-canonical modes of brain function in mouse models of autism; and to test how the method detects pharmacologically induced alterations at the whole-brain level. **Chapter 2** encapsulates the design of the method and tests on its reproducibility, as well as its effectiveness in detecting fMRI dynamic changes in a mouse model of autism. This Chapter has been published as a pre-print and is currently submitted to a peer-reviewed journal. This work was also selected for oral presentations at the Italian Association for Magnetic Resonance in Medicine (AIRMM) of 2018, and the International Society of Magnetic Resonance in Medicine (ISMRM) conference of 2018. It was selected to be part of the 150 dynamic posters available at the Society for Neuroscience (SfN) meeting in 2017, and our current work will also be presented also as a dynamic poster in the 2018 SfN meeting.

Chapter 3 applies the method to investigate the effect of xanomeline, a pro-arousing agent that engaged the brain in a new set of whole-brain states.

Chapter 4 concludes with a brief summary of our findings and their potential impact within the neuroscience community, and with a series of considerations regarding the use of our analytical approach, highlighting future studies and potential uses with diverse datasets.

Chapter 2

Oscillatory brain states govern spontaneous fMRI network dynamics

This Chapter has been published as:

Daniel Gutierrez-Barragan, M. Albert Basson, Stefano Panzeri, Alessandro Gozzi (2018). "Oscillatory brain states govern spontaneous fMRI network dynamics." in: Biorxiv. doi: https://doi.org/10.1101/393389

2.1 Introduction and background.

Spontaneous neural activity is ubiquitously present in the mammalian brain and persists across physiological states (Buzsáki and Draguhn, 2004; Mohajerani et al., 2010). In humans, whole-brain patterns of intrinsic brain activity are typically mapped by measuring spontaneous functional magnetic resonance imaging (fMRI) signal in the resting brain (Power et al., 2014), an approach termed resting-state fMRI (rsfMRI). A large body of experimental work has shown that low-frequency fluctuations in the fMRI signal are temporally synchronous across multiple functional systems, delineating a set of reproducible topographies known as resting-state networks, which can be reliably identified also in primates (Vincent et al., 2007) and rodents (Gozzi and Schwarz, 2016). These observations have prompted a widespread use of inter-regional correlation between rsfMRI signals as an index of functional coupling, or "functional

connectivity" between regions. Importantly, additional studies have further shown that rsfMRI activity is characterized by rich temporal structure, involving dynamic reconfiguration into transient states entailing variations in resting state networks occurring on the time scale of seconds (Hutchison et al., 2013). These studies have promoted a view of the resting brain as an inherently dynamic system, in which highly evolving patterns of instantaneous activity interact over time in a sporadic or stochastic fashion (Braun et al., 2015).

Recent animal studies have linked hemodynamic-based measures of intrinsic brain activity to low-frequency oscillatory neural activity as measured with calcium imaging (Matsui et al., 2016; Schwalm et al., 2017; Xiao et al., 2017). Specifically, optical imaging studies in mice have implicated global waves of neural activity and transient neural co-activations among homotopic areas as key neural drivers of hemodynamic-based measurements of functional connectivity (Matsui et al., 2018, 2016). In keeping with these experimental results, human rsfMRI network activity can be reliably described by brief instances of regional peak fMRI activity (Liu and Duyn, 2013), a feature that has been related to transient variation in calcium co-activation patterns (Matsui et al., 2018). Taken together, these findings suggest that reconfiguration of spontaneous network activity may be guided by transitions between recurring patterns of slow-wave activity. Such an interpretative framework is consistent with the initial recognition of putative temporal sequences of propagated fMRI activity defined as quasi-periodic patterns, or lag threads of propagated fMRI signal in human rsfMRI datasets (Mitra and Raichle, 2016; Yousefi et al., 2018). However, a precise characterization of how network states interact and dynamic brain reconfigurations occur is lacking. Are spontaneous network transitions organized stochastically, or do they reflect a set of recurring default states? And what are the fundamental principles by which brain-wide patterns of spontaneous fMRI activity reconfigure and interact with each other?

Here we devised an optimized frame-wise clustering strategy, combining the identification of recurrent patterns of spontaneous fMRI activity with an analysis of how these spatial patterns are dynamically coupled. We show that this approach enables brain-wide mapping of spontaneous rsfMRI activity with voxel-resolution in the resting mouse brain (Gozzi and Schwarz, 2016; Liska et al., 2015; Sforazzini et al., 2014), and demonstrate the reproducibility of our findings across different rsfMRI datasets. Specifically, we describe a set of recurring

brain-wide functional states that can be reliably mapped at the group and subject level, and show that the dynamics of their transitions can be compactly described as a set of coupled oscillators, each corresponding to a spatial pattern, and each preferentially occurring at specific phases of global fMRI signal (GS) fluctuations. Importantly, we demonstrate that aberrant patterns of fMRI connectivity in a genetic model of autism reflect the engagement of non-canonical brain states, characterized by altered regional topography and oscillatory dynamics. Collectively, our approach points at oscillatory network activity as a fundamental level of organization of spontaneous brain activity, and describes a set of new principles guiding the spatio-temporal organization of resting state activity.

2.2 Methods

Ethical Statement

All in vivo experiments were conducted in accordance with the Italian law (DL 26/214, EU 63/2010, Ministero della Sanità, Roma) and the recommendations in the Guide for the Care and Use of Laboratory Animals of the National Institutes of Health. Animal research protocols were reviewed and consented by the animal care committee of the Istituto Italiano di Tecnologia. All surgical procedures were performed under anaesthesia.

rsfMRI data acquisition

Experiments were performed on a set of n = 40 adult (12-18 week-old) male C57Bl6/J mice. This is the main dataset that we have used throughout our article to describe rsfMRI dynamics, and all results presented below have been generated with this set of rsfMRI images, unless otherwise stated. The animal preparation protocol for experimental measurements has been described in great detail (Ferrari et al., 2012; Sforazzini et al., 2016). Mice were anaesthetized with isoflurane (5% induction), intubated and artificially ventilated (2%, surgery). The left femoral artery was cannulated for continuous blood pressure monitoring and terminal arterial blood sampling. At the end of surgery, isoflurane was discontinued and substituted with

halothane (0.75%). Functional data acquisition commenced 45 min after isoflurane cessation. Mean arterial blood pressure was recorded throughout imaging sessions. Arterial blood gases (paCO2 and paO2) were measured at the end of the functional time-series to exclude non-physiological conditions.

MRI data were acquired with a 7.0 Tesla MRI scanner (Bruker Biospin, Ettlingen) as previously described (Liska et al., 2015), using a 72 mm birdcage transmit coil, and a four-channel solenoid coil for signal reception. For each session, high-resolution anatomical images were acquired with a fast spin echo sequence (repetition time (TR)/echo time (TE) 1200/15 ms, matrix 192 × 192, field of view 2 × 2 cm2, 18 coronal slices, slice thickness 0.60 mm). Co-centered single-shot blood-oxygen level dependent (BOLD) EPI time-series were acquired using an echo planar imaging sequence with the following parameters: TR/TE 1200/15 ms, flip angle 30°, matrix 100 × 100, field of view 2 × 2 cm2, 18 coronal slices, slice thickness 0.50 mm, 500 (n= 21) or 1500 (n = 19) volumes and a total rsfMRI acquisition time of 10 or 30 minutes, respectively. All the group analyses were carried out on the first 500 timepoints (10 min). The single subject CAP analysis was limited to the n = 19 subjects in which we acquired 1500 timepoints.

To corroborate the reproducibility of our findings across independent datasets, we applied the whole analysis to an additional dataset composed of n = 41 male C57Bl6/J mice in which we acquired rsfMRI time-series (n = 300, 6 min) using the same sedation protocol and image parameters employed in the present study. A characterization of functional network organization in this set of animals has been previously described (Liska et al., 2015). We refer to this animal cohort as to dataset 2. Finally, to assess the ability of our analytical approach to detect aberrant states in mouse models of brain pathology, we applied our analytical framework to a cohort of Chd8 haploinsufficient mice, a relevant subtype of autism spectrum disorder, which has been previously described to present aberrant rsfMRI network activity (Suetterlin et al., 2018). Briefly, rsfMRI imaging was performed on 15-18 week old mice (n=23 Chd8+/+; n=19 Chd8+/-, both lines have a C57Bl6/J background), each with 500 volumes (10 min), using the same animal preparation protocol and rsfMRI acquisition parameters of dataset 1. The control group in this third study was employed as a third independent dataset for the validation of our clustering procedure (dataset 3 or Chd8+/+).

Data pre-processing

Data preprocessing was carried out as recently described (Liska et al., 2017). Briefly, fMRI time-series were despiked, motion corrected, and spatially normalized to an in-house mouse brain template (Sforazzini et al., 2014) yielding a final normalized spatial resolution of 0.1 x 0.1 x 0.5 mm3 (192 x 192 x 24 matrix). Head motion traces and the mean ventricular signal (average fMRI time-series within a manually-drawn ventricle mask from the template) were regressed out. The resulting images were spatially smoothed using a Gaussian kernel of 0.5 mm FWHM, band-pass filtered using a 0.01 – 0.1 Hz band, and z-scored voxel-wise.

Seed-based CAP analysis and spatial correspondence with rsfMRI correlation networks

To probe the relationship between networks inferred from conventional rsfMRI seed-based correlation analyses, and those described by high regional fMRI activity at only a few critical time points (Liu and Duyn, 2013; Tagliazucchi et al., 2012), we spatially averaged individual rsfMRI volumes (here referred to as "frames") exhibiting peaks of regional activity in a set of a priori regions of interest. The employed averaging yields spatial maps of averaged spontaneous fMRI activity, which we termed seed-based mean CAPs. Seed location was chosen based on prior rsfMRI mapping in the mouse (Liska et al., 2015; Sforazzini et al., 2014). For each of the probed regions, we also computed a canonical group-level correlation map using the corresponding regional rsfMRI signal as seed. We next computed the spatial correlation between the seed-based CAPs and their corresponding correlation maps by retaining rsfMRI frames exceeding a predefined intensity threshold, covering the whole 0-99th percentile range as previously described (Liu and Duyn, 2013). For illustrative purposes, we generated representative seed-based CAPs by averaging all the fMRI frames with the highest 15% BOLD signal intensity across all subjects (68 ± 5 out of 500 frames, mean ± SD, all subjects), and using a T threshold of 7, corresponding to $p < 0.01$, Bonferroni corrected (Amico et al., 2014; Liu and Duyn, 2013). For each region we also generated a group-level canonical seed-based correlation map, which we thresholded at $T = 7$, corresponding to $p < 0.01$, Bonferroni corrected).

Whole-brain CAP analysis

We used spatial clustering of individual fMRI frames to identify whole-brain patterns of simultaneous co-activation of brain activity with voxel-resolution. Following prior studies (Karahanoğlu and Van De Ville, 2015; Liu et al., 2013; Liu and Duyn, 2013), we carried out frame-wise clustering of brain-wide mouse rsfMRI images by retaining the voxels that were in the top 10% or in the bottom 5% of all BOLD signal in a single time frame, a procedure employed to minimize spurious influence of random, non-physiological signal fluctuations in fMRI time-series (Liu et al., 2013). The preprocessed fMRI frames were formatted into N-dimensional vectors $t = (t_1, t_2, \dots, t_T)$ with T being the number of frames, and N the amount of voxels. Such frames were clustered using the k-means++ algorithm (Arthur and Vassilvitskii, 2007), which partitions the vector-set into k clusters $C = (C_1, C_2, \dots, C_k)$ such that the sum of within-cluster distances D in the following equation is minimized:

$$D = \sum_{i=1}^{k} \sum_{t_j \in C_i} d(t_j, \mu_i)$$

being μ_i the mean of the fMRI frames in each cluster C_i, and $\mathrm{d}(\mathrm{t_j}, \mu_\mathrm{i})$ the distance between the fMRI frame at time i and the cluster mean, measured as one minus the spatial Pearson's correlation coefficient. The k-means++ algorithm provides an optimized initialization of each centroid (seeding), such that distant centroids have a higher chance of being chosen as starting seeds for the clustering procedure. The addition of this step has been shown to outperform conventional k-means with random seeding both in terms of clustering performance and speed (Arthur and Vassilvitskii, 2007).

We note here that the above described intensity masking does not affect the final results, and operating the clustering, as well as all the successive phase analyses, directly on unmasked fMRI data did not change the results qualitatively, either in terms of CAP spatial shape or in terms of phase results. Indeed, clustering the unmasked data led only to a marginal change (fraction 1.64%) in the time frames that were assigned to different clusters by either the masked or the unmasked procedure, and the spatial correlation between the CAPs obtained with or without masking was higher than > 0.98 for all the states.

k-means clustering was carried out on the whole rsfMRI dataset 1 (40 x 500 frames), with k ranging from k = 2 up to 20, using Pearson correlation between fMRI data in different time frames as clustering distance measure, and using 15 replicates with 500 iterations each. Departing from previous investigations in which the number of clusters was selected ad hoc (Karahanoğlu and Van De Ville, 2015; Liu et al., 2013; Liu and Duyn, 2013) we carried out k number selection generalizing a more quantitative procedure, aimed at identifying the most robustly occurring co-activation patterns, which was previously employed to map robust, recurrent states in electrophysiological recordings (Logothetis et al., 2012). Briefly, we first computed, for increasing k, how much variance is explained by the clustering algorithm (**Fig. S2.1-B**), defined as the ratio between the between-cluster variance and the total variance (within-cluster + between-cluster variance). Within-cluster variance was computed as the averaged (over clusters) sum of square distances between elements in a cluster and its centroid. Between-cluster variance was computed as the averaged square distance between a cluster centroid and the centroid of all clusters or centroid of all data (Goutte et al., 1999). Higher values of explained variance correspond to a better description of the dataset, and that optimal k values can be identified in the "elbow" region of the explained variance plot, after which only marginal variance is gained by further refining the partition. We thus selected the value k as the largest value within the elbow region that insured full reproducibility of the corresponding CAPs across the three independently collected datasets used in this study. To this purpose, we progressively increased k until (a) the dataset variance explained by k clusters was larger than the variance explained by k-1 clusters and (b) a replication of the clustering procedure on two additional independent rsfMRI datasets (n = 41, 300 frames, and n = 23, 500 frames, respectively), would result in anatomically equivalent co-activation patterns (defined as between dataset CAP correlation > 0.45, which corresponds to a highly significant correlation, $p < 10^{-5}$, permutation test, **Fig. S2.1**). This procedure identified k = 6 CAPs conserved across all the three rsfMRI datasets (**Fig. 2.3** and **Fig. S2.1**). To compute the centroid of each cluster (which we took as a CAP), the fMRI frames assigned to each cluster were averaged voxel-wise, and normalized to T-scores ($p < 0.01$, Bonferroni corrected), permitting to visualize the mean voxel-wise distribution of fMRI BOLD signal for each of the identified CAP. For visualization purposes, the obtained maps were thresholded to T-scores > 7, corresponding to a $p < 0.01$, Bonferroni corrected. For each CAP we next computed its occurrence rate (i.e. the

proportion of frames assigned to each CAP) and duration (i.e. the average number of consecutive frames belonging to the same CAP at each occurrence) for each of the n = 40 subjects. We also computed between-CAP spatial similarity, defined as pair-wise spatial correlation between all the identified CAPs.

To assess the ability of our approach to detect CAPs also at the subject level, we repeated the clustering analysis in a subset of 19 subjects of the main dataset for which we acquired extended (30 min, 1500 frames) time-series, using the group-level CAPs as initial centroids. The CAPs found in each subject were next matched to the group-level templates using the Hungarian Algorithm (Kuhn, 1955), and their spatial correlation was computed. To illustrate CAP incidence across subjects, we mapped, for each voxel in a CAP, the proportion of subjects which had a significant co-activation (T-test, $p < 0.05$, FDR corrected) and equal co-activation sign (i.e. positive or negative BOLD signal) of the corresponding group-level CAP template.

CAP dynamics

To investigate the dynamics of CAP evolution, we generated a CAP-to-frame correlation time-course (which we term "CAP time-course"). We computed these spatial correlations in each time frame as the Pearson correlation between the centroid of the considered cluster and the masked fMRI activity in the considered time frame of a given subject as previously described (Liang et al., 2015). For plotting purposes, we normalized the CAP time-courses into SD units. This normalization does not affect in any way either the power spectra profile or the distribution of the phase values. To describe the assembly and disassembly dynamics of CAPs, we used the method devised by Liang et al. (2015). Briefly, for each CAP we selected the fMRI frames corresponding to the local maxima within the CAP's time-course, limiting the selection of peak events to 2% of all the concatenated frames, and adjusting this number for each CAP's occurrence rate. For example, for CAP 1 (occurrence rate = 0.18) we sampled 0.18 x 400 frames corresponding to the CAP's time-course local maxima. Each selected frame was set as a time $t = 0$ reference event, and we next sampled frames within a $-30 \leq t \leq 30$ repetition interval. All events were time-lock averaged, leading to a dynamic portrayal of mean temporal evolution of CAP assembly and disassembly in the form of concatenated frames (supplementary movies S1-6).

The temporal structure of the CAP time-courses for each subject was also assessed by computing its power spectrum. The spectra of the Global fMRI Signal (GS) was also computed.

We assessed the relationship between GS oscillations and CAP's by sampling each CAP's occurrence within GS band-filtered cycles. To compute the instantaneous phase of the GS in the infra-slow range, we first band-pass filtered the GS time-courses between 0.01-0.03 Hz. We then used the Hilbert Transform (Montemurro et al., 2008) to decompose the GS signal into an analytical signal with a characteristic instantaneous phase and amplitude. We divided each subject's instantaneous GS phase signal into cycles in the range $[0, 2\pi]$, and within each cycle, collected the GS phase values at each CAP's occurrence. Using the same filter design described above, we filtered and again normalized the CAP time-courses, and sampled the GS phase at each CAP occurrence only when the CAP time-course at that instant was above 1 SD, in order to ensure that a specific frame pertained to a specific CAP. Using the Matlab CircStats toolbox (Berens et al., 2009), we computed circular statistics of the obtained distribution of GS phases at each CAP, and represented their dispersion in a cosine cycle representing a GS oscillation, using the circular variance to quantify dispersion around the circular mean. To probe the presence of phase-coupling between CAP occurrence and GS oscillatory dynamics, we computed the angular differences (phase differences) of the GS between occurrences of a given CAP within a GS cycle, and occurrences of another CAP within the previous, current, and subsequent cycle. Again, GS phase samples at each CAP were only considered if their filtered values at that instant were above 1 SD at the corresponding instances.

CAP dynamics in a genetic model of autism

The same analytical approach described above was applied to rsfMRI time-series recorded in n = 23 Chd8+/+ and n=19 Chd8+/- littermates (Suetterlin et al., 2018) after performing the same preprocessing steps applied to the other datasets. CAPs were computed independently in each group. We used k = 6, as this value ensured highest cross-dataset reproducibility of the identified clusters as described in the Results section (**Fig. S2.1**). Inter-group CAP maps were matched using the Hungarian algorithm according to their spatial similarity. Inter-group differences in CAP anatomy were mapped using a two-sample t-test and family-wise error (FWE) cluster correction ($p < 0.05$, cluster-defining threshold $T(40) = 2.8$). We then computed

CAP features and CAP time-courses for all subjects in each strain, and sampled the filtered GS-phase distributions at each CAP occurrence for each group of mice independently. Differences between preferred GS-phase at CAP occurrences were computed using a William-Watson test for circular mean homogeneity, Bonferroni corrected for six comparisons. We also sampled the angular differences (phase differences) of the GS between occurrences of a given CAP within a GS cycle, and occurrences of another CAP within the previous, current, and subsequent cycle. Again, GS phase samples at each CAP were only considered if their filtered values at that instant were above 1 SD at the corresponding instances.

Finally, to assess the involvement of individual CAPs in the seed-based rsfMRI correlation differences previously described between hippocampal and motor-sensory areas (Suetterlin et al., 2018), we computed differences in whole-brain correlation maps between a 3 x 3 X 1 voxel seed placed bilaterally in the somato-sensory cortex. Inter-group differences were assessed using a two-sample t-test and family-wise error (FWE) cluster correction ($p < 0.05$, cluster-defining threshold $T(40) = 2.8$). We then recomputed Pearson correlation between this seed and selected foci of over-connectivity in the hippocampus. The rsfMRI correlation profiles were computed before and after regressing each CAP's time-course independently in each subject. Differences in rsfMRI correlations were assessed by means of a repeated measures two-way ANOVA.

2.3 Results

Selective fMRI frame averaging recapitulates networks of correlated activity

The observation that spontaneous brain activity may be driven by brief instances of simultaneous activation of various brain regions (Matsui et al., 2016) implies that key information about the dynamic structure of resting state activity can be retrieved from individual fMRI frames. It has been previously shown that selective averaging of fMRI frames exhibiting regional peaks of BOLD activity can closely recapitulate rsfMRI connectivity

networks obtained via seed-based correlation analysis (Liu and Duyn, 2013; Tagliazucchi et al., 2012). As a first step towards a voxel-wise mapping of spontaneous fMRI signal dynamics in the mouse, we probed whether this relationship holds true also in this species. To this aim, we measured rsfMRI network activity in 40 adult male mice over a time window of 10 minutes (500 timepoints, main dataset). We used pre-defined anatomical regions as rsfMRI correlation seeds, and spatially averaged individual fMRI frames as a function of their peak intensity signal, to produce seed-based mean co-activation patterns (CAPs). We next compared the obtained "seed-based mean CAPs" with canonical rsfMRI correlation maps (**Fig. 2.1**). Consistent with previous observations, we found that previously-described rsfMRI networks, including the mouse hippocampal, latero-cortical, auditory-temporal and default-mode networks (DMN, see **Fig. 1.3**) (Liska et al., 2015), can be spatially reproduced by averaging a limited number (e.g. 15%, **Fig. 2.1A**) of fMRI frames exhibiting peak BOLD activity in corresponding anatomical seed locations.

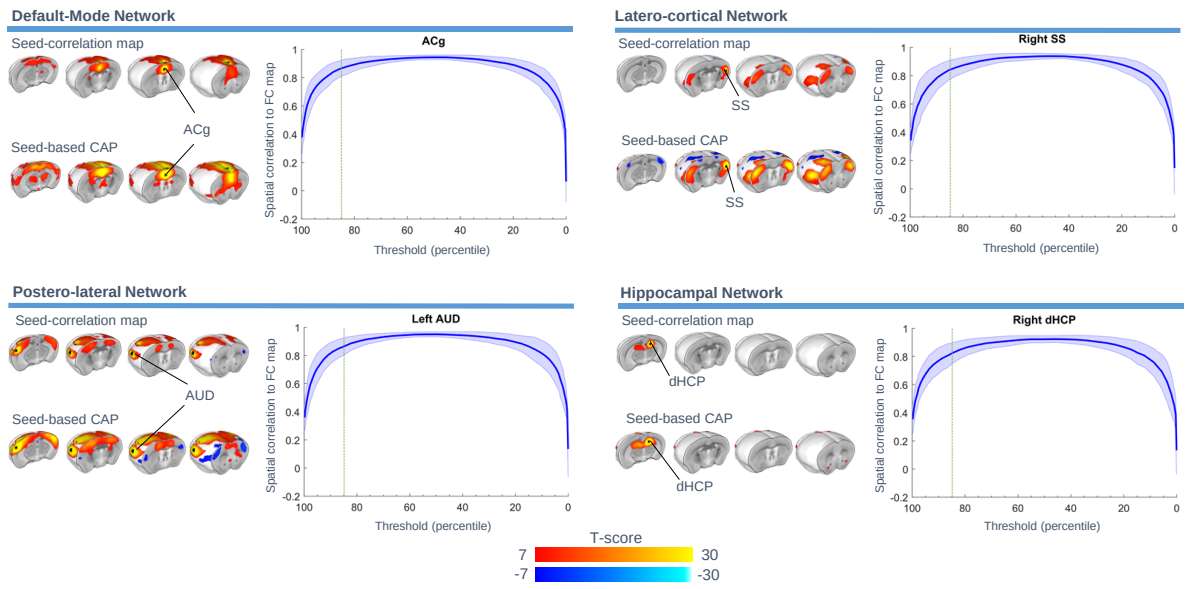

Figure 2.1: Selective fMRI frame averaging recapitulates rsfMRI network activity. rsfMRI networks obtained via seed-based correlation are spatially recapitulated by averaging fMRI frames exhibiting peak regional BOLD fMRI activity (seed-based CAPs). This relationship is illustrated for four representative mouse rsfMRI networks mapped via seed-based correlation analysis (ACg, anterior cingulate, SS, somatosensory cortex, AUD, auditory cortex, dHCP, dorsal hippocampus). Plots on the right illustrate the spatial overlap between seed-based correlation maps and seed-based CAPs, as a function of the percentage of frames used for the computation of the

latter (group mean +/- SEM). The dashed green line indicates the 15-percentile threshold employed for seed-based CAP visualization.

Whole-brain fMRI frame clustering reveals a set of recurring functional brain states

The observation that regional peaks of fMRI activity drive spatially-structured network topographies is consistent with spontaneous neural activity being a non-stationary phenomenon, in which evolving brain-states undergo recurring reconfiguration. To obtain a regionally-unbiased characterization of these states and their transition dynamics in the mouse brain, we devised a k-means clustering analysis of all the individual rsfMRI frames, without any a priori temporal, anatomical or intensity-based restriction (**Fig. 2.2**). As opposed to describing co-activated networks as a set of spatially-correlated patterns of activity, this approach identifies, as prototypes of each of k spatial activity clusters, the different types of simultaneous single time-frame co-activation patterns (shortened hereafter as CAPs or "functional states") that recur in the data (**Fig 2.2-C**). In contrast to seed-guided selective fMRI frame averaging, this strategy does not require the a priori selection of regions of interest or the use of fMRI intensity thresholds, and can identify composite functional states characterized by both patterns of simultaneous co-activation (above fMRI signal baseline) and co-deactivation (below fMRI signal baseline, **Fig. 2.2**). Importantly, because our approach classifies activity in all time-frames, it permits to reliably detect multiple brain-wide patterns of spontaneous brain activity, and not only those that occur at either local or global peaks of regional BOLD activity.

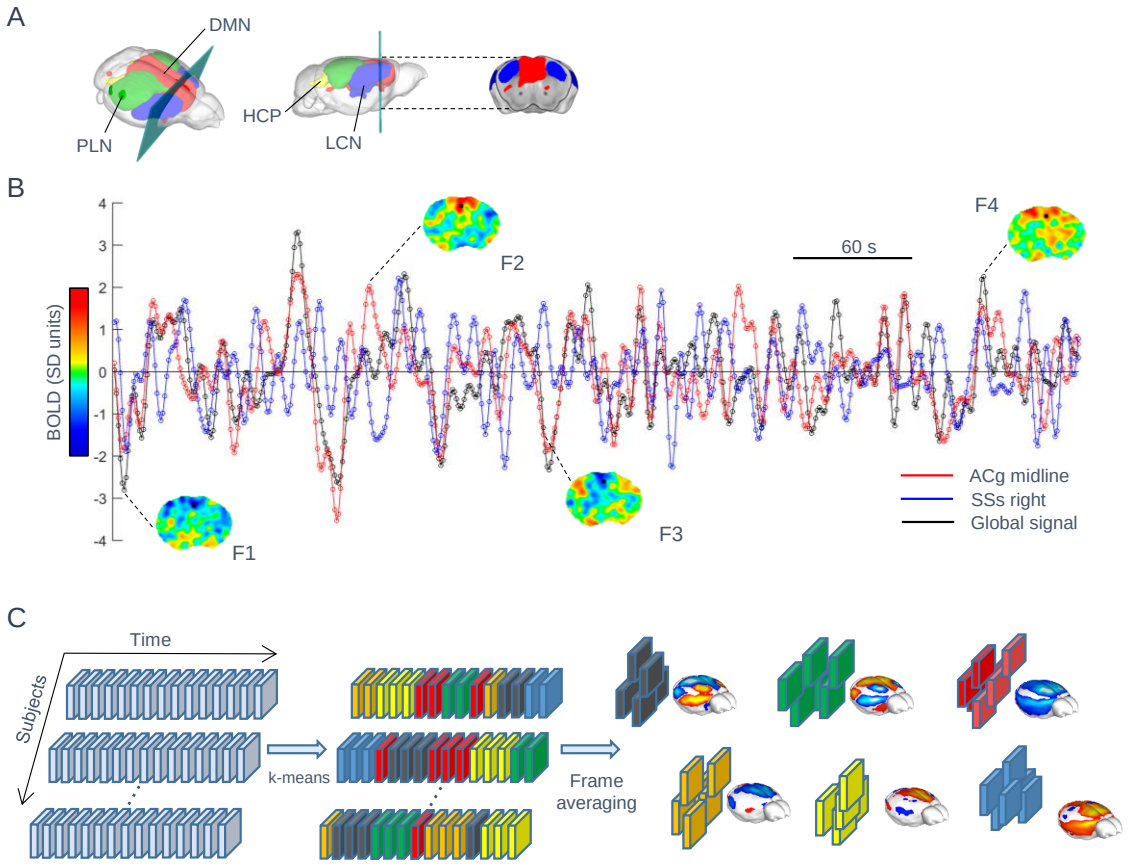

Figure 2.2: Identification of recurring brain states via whole-brain fMRI frame clustering. (A) Glass brain representation of the seed-based resting-state networks described in Figure 1 (DMN: default mode network, HCP: hippocampal network, LCN: latero-cortical network, PLN: postero-lateral network). (B) Illustrative fMRI BOLD time-course (SD units) in the anterior cingulate (ACg, red), somatosensory cortex (SSs, blue) as well as fMRI global-signal (black) in a representative subject (brain slice illustrated in panel A). Note the presence of peaks of concordant or diverging BOLD activity in cingulate and somatosensory areas across time, suggestive of time-varying network reconfiguration; cingulate and somatosensory regions are concurrently co-activated and co-deactivated in F1 and F4, but they exhibit opposing BOLD activity in F2 and F3. (C) These dynamic transitions can be captured and classified into recurring brain states by clustering fMRI frames into spatially congruent patterns (CAPs), using the k-means algorithm.

The use of an unsupervised algorithm like k means poses the problem of selecting an appropriate number of clusters. Our goal was to partition the dataset into whole-brain fMRI states that are robust and reproducible, and to ensure that each selected cluster could be trusted to reflect a genuine set of coactive brain regions. To this aim, we first computed, for increasing k, how much variance is explained by the clustering algorithm (**Fig. S2.1-B**). The explained variance curve, computed for the main dataset, revealed an elbow region encompassing the range k = 4 – 10 in which variance was still increasing (thus using more cluster yielded a better

description of the datasets), but its increase was progressively smaller (denoting that the importance of adding more clusters was getting smaller and smaller, **Fig. S2.1-B and C**). We selected the value k as the highest value within the elbow region that still ensured maximal between-dataset reproducibility of the corresponding CAPs with respect to two additional independently collected rsfMRI datasets (n = 41 and n = 23, respectively).

With this procedure, we identified k = 6 states which were robustly conserved across the three rsfMRI datasets, and necessary for describing the datasets with high accuracy (**Fig. 2.3** and **Fig. S2.1**). Further credibility for the robustness of these six states as sets of genuinely coactive fMRI voxels, is given by the identification of the same CAPs at the single subject level (described below), and the fact that these 6 patterns were present also when partitioning the main dataset into a higher number of clusters (**Fig. S2.1**). While fMRI clustering with k = 7 and 8 revealed additional plausible states, we restricted our subsequent analyses to the first 6 clusters, as this appears to be the finest partition exhibiting the highest cross-dataset reproducibility. It should however be noted that there was a seventh state, plotted in **Figure S2**, that appeared to be very stable across the two larger control ("wild-type") datasets (n = 40 and n = 41), but that exhibited low reproducibility on the third, smaller, reference image set (n = 23). Although we did not include this seventh state in any further analyses here, our observations raise the possibility that this CAP, being found very robustly in the two largest independent datasets, may reflect a less stable, yet functionally meaningful state, and so we briefly document its properties in the **supplemental information section**.

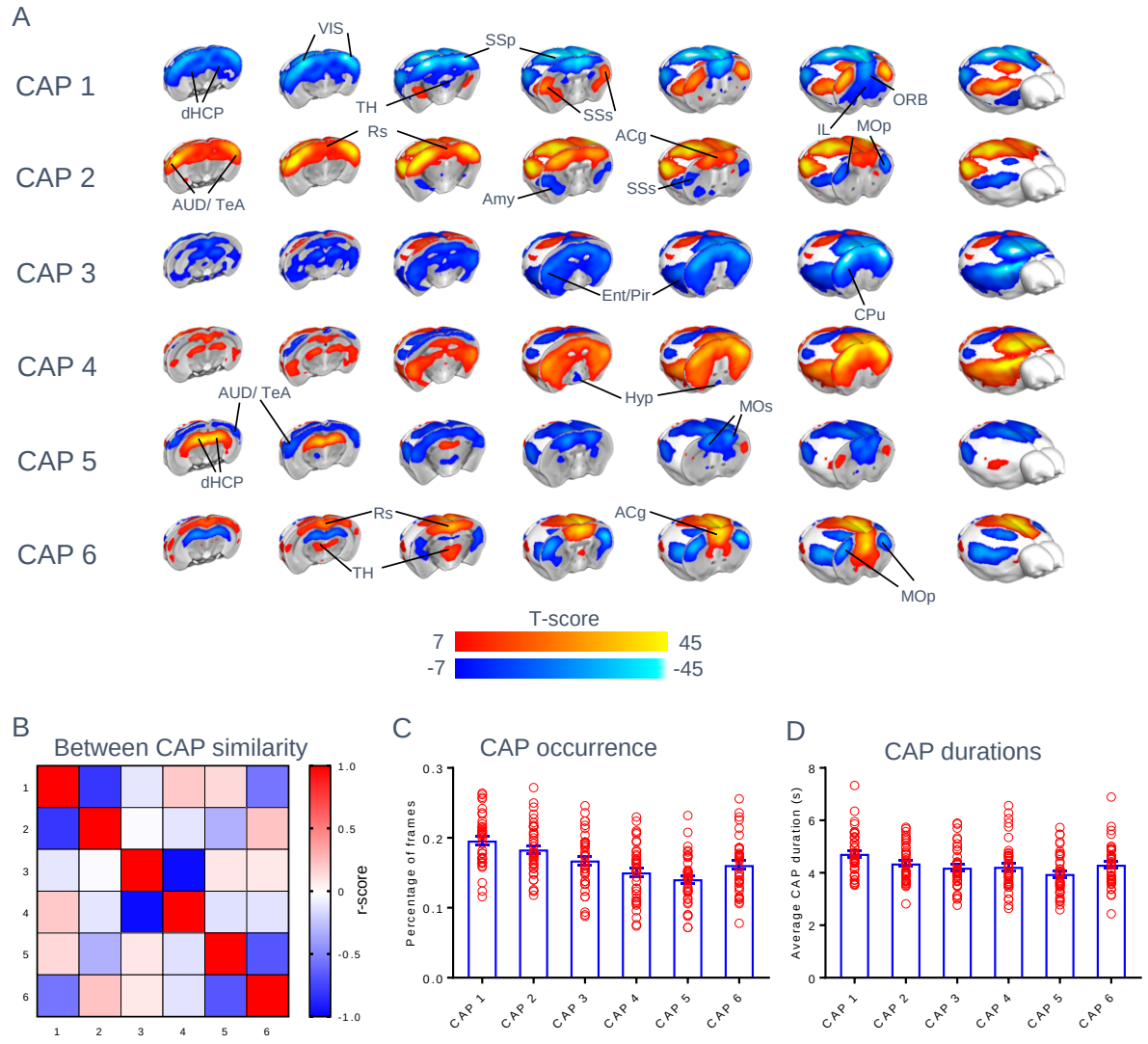

Figure 2.3: Recurring functional states of the mouse brain. (A) Whole brain representation of the functional brain states (CAPs) we identified at the group level. Red/yellow indicates co-activation (i.e. high fMRI BOLD signal) while blue indicates co-deactivation (i.e. low fMRI BOLD signal) ($p < 0.01$, Bonferroni corrected). CAPs have been ordered based on their spatial properties by numbering consecutively states characterized by opposing BOLD co-activation patterns (i.e. 1-2, 3-4 and 5-6), as denoted by the negative correlations in panel (B). Panels (C) and (D) illustrate CAP occurrence rate and mean duration, respectively (mean +/- SEM). Abbreviations: ACg – Anterior Cingulate cortex; AUD – Auditory cortex; CPu – Caudate-Putamen; dHCP – dorsal Hippocampus; vHCP – ventral Hippocampus; HT – Hypothalamus; ILA – Infralimbic Area; LAN – Lateral Amygdalar Nucleus; MOp – primary Motor cortex; MOs – secondary Motor cortex; ORB –Orbitofrontal cortex; PIR – Piriform Area; PL – Pallidum; Rs – Retrosplenial cortex; SSp – primary Somatosensory cortex; SSs – secondary Somatosensory cortex; ST – Striatum; TeA – Temporal Association area; TH – Thalamus; VIS – Visual cortex.

fMRI states encompass known connectivity networks of the mouse brain and can be identified at the single subject level

An illustration of the six identified states is reported in **Figure 2.3-A**. One defining characteristic of all the six CAPs is their configuration as a composite assembly of regional substrates encompassing previously-described distributed resting-state networks of the mouse brain. For example, CAP 1 shows a clear co-activation of primary and secondary motor-sensory areas belonging to the mouse latero-cortical network (LCN) together with deactivation of cortico-limbic regions and peri-hippocampal constituents of the mouse DMN. Similarly, CAP 5 encompasses co-deactivation of the DMN, and co-activation of the hippocampal network. These correspondences are illustrated in **Figure S2.3**, in which we report an empirical decomposition of some of these CAPs into a set of putative constituting rsfMRI networks. The presence of spatially-prominent contributions of known rsfMRI connectivity networks in the identified states, plus their duration in the in the order of a few seconds (Fig. 2.3-D), implicate the observed patterns as time-varying functional states underlying rsfMRI network dynamics as assessed with correlational techniques.

To investigate whether the selected six states are representative of spontaneous brain dynamics identifiable at the single subject level, we repeated our state-detection using k = 6 on a subset of nineteen mice for which we acquired rsfMRI images over a 30-minute window. We next spatially matched each subject-level state with the corresponding CAP obtained at the group-level analyses (**Figure S2.3-A**), to obtain a voxel-wise CAP incidence maps. These analyses revealed that all 6 states can be reliably identified at the single subject level, with foci of very high cross-subject incidence in key network locations (**Fig. 2.4-A**). Importantly, the spatial distribution of the observed CAPs at the subject level (**Fig. 2.4-B**) closely recapitulates the features that we observed with group-level clustering (**Fig. 2.4-B**). These correspondences suggest that the six identified CAPs correspond to genuine brain states, representative of spontaneous functional reconfigurations occurring at the single subject level.

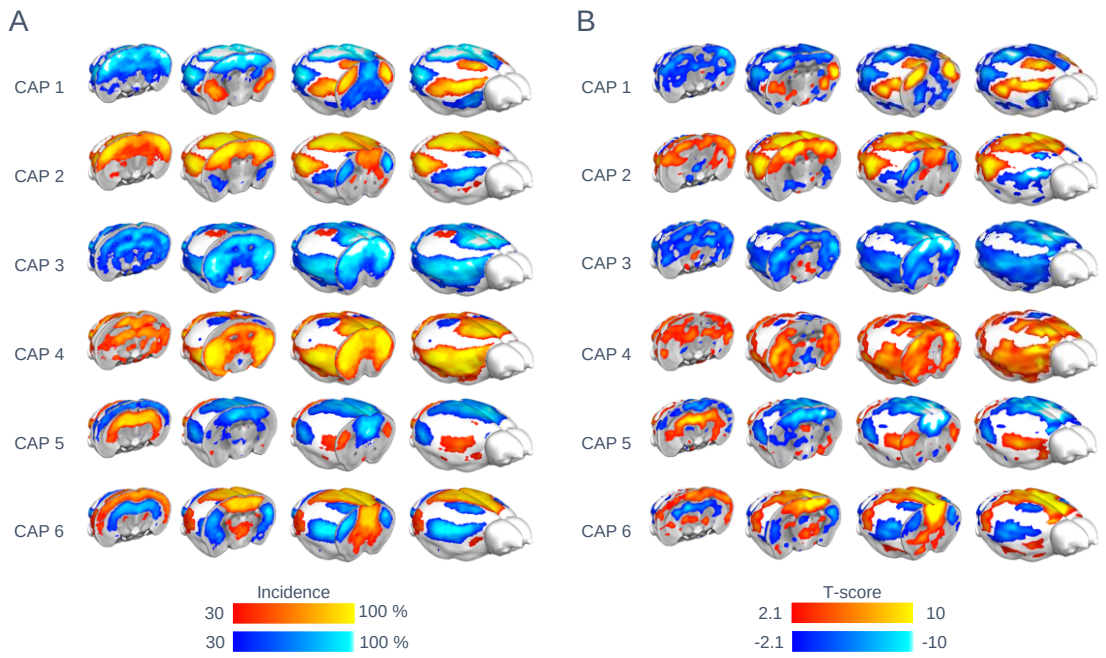

Figure 2.4: Brain states can be detected at the single-subject level. Left: incidence map of each CAP at the subject level (k = 6, 30 min rsfMRI acquisitions, $p < 0.05$, FDR corrected). Each voxel represents the proportion of subjects with significant co-activation ($p < 0.05$, FDR corrected) as its corresponding group-level CAP template. Right: Spatial distribution of CAPs detected in a representative subject ($p < 0.05$, FDR corrected). Yellow indicates regional co-activation, blue regional co-deactivation.

The use of sedation in mouse fMRI acquisitions allows for tight control of motion-related artefacts (Gozzi and Schwarz, 2016). We nevertheless assessed the role of potential frame displacements in our datasets by re-computing group-level CAPs upon strict censoring of putative "motion-affected" frames. To this purpose, we employed a frame-wise displacement (FD) threshold of 75 and 100 µm, leading to a rejection of 24% and 10% putative "high-motion" frames, respectively. Despite the use of disproportionately strict motion censoring, the resulting CAPs were spatially undistinguishable from what observed by using uncensored frames (**Fig. S2.4-A and B**). We also computed the assignment of putative "motion-affected" frames to each CAP using the above-mentioned FD thresholds, and did not observe any CAP being dominantly enriched in motion contaminated frames (one -way ANOVA, $p = 0.51$ and 0.91 respectively, **Fig. S2.4-C and D**). These results argue against a significant contribution of motion artefacts to our imaging results.

Functional states can be classified into opposing, oscillating patterns of co-activation

A notable feature of the identified CAPs, is their configuration into state and anti-state pairs characterized by opposing patterns of functional co-activation (**Fig. 2.3-A, and B**). This feature was especially prominent in CAPs 3 and 4 (r = -0.96), involving a contrasting co-activation of neocortical regions, but was also apparent in CAPs 1 and 2 (r = -0.80), and CAPs 5 and 6 (r = -0.66), the first pair being characterized by a clear anti-correlation between the DMN and LCN, the latter between hippocampal areas and the DMN (**Fig. 2.3-A, and B**). Importantly, the observation of opposite spatial configurations was not necessarily expected, or resulting from the employed clustering procedure. This attribute suggests that the networks expressed by these states continue to be similarly correlated or anti-correlated with other elements of the network not only when these elements are co-activated, but also when they are co-deactivated. This could happen if the state anti-state pairs undergo an ongoing oscillation, with opposite states reflecting peaks and troughs of these network fluctuations.

Based on the above results, we hypothesized that the dynamics of transition between CAPs could be described in oscillatory terms. To test this hypothesis, we computed at each instant of time the spatial correlation between each CAP and the BOLD fMRI signal in that time frame (**Fig. 2.5-A**). The obtained index, hereafter referred to as "CAP time-course", assesses the spatial match between spontaneous brain activity and the specified CAP in the considered time frame. When we computed the power spectra of each CAP time-course (**Figure 2.5-B**), we observed a clear peak of power in the 0.01-0.03 Hz frequency band, indicating that that brain-wide spontaneous brain activity undergoes transitions between network configurations described by CAPs, with infra-slow oscillatory dynamics. To capture and visualize the spatio-temporal dynamics of CAP assembly and disassembly across consecutive frames, we next computed the average of the whole-brain BOLD frames time-locked around each CAP time-course's local maxima. These results, which are best visualized in the form of movies (Supplementary movies 1-6), clearly show how each state builds-up and disassembles with spatial patterns that strikingly resemble wave-like propagating activity observed with calcium imaging in the mouse dorsal cortex (Matsui et al., 2018).

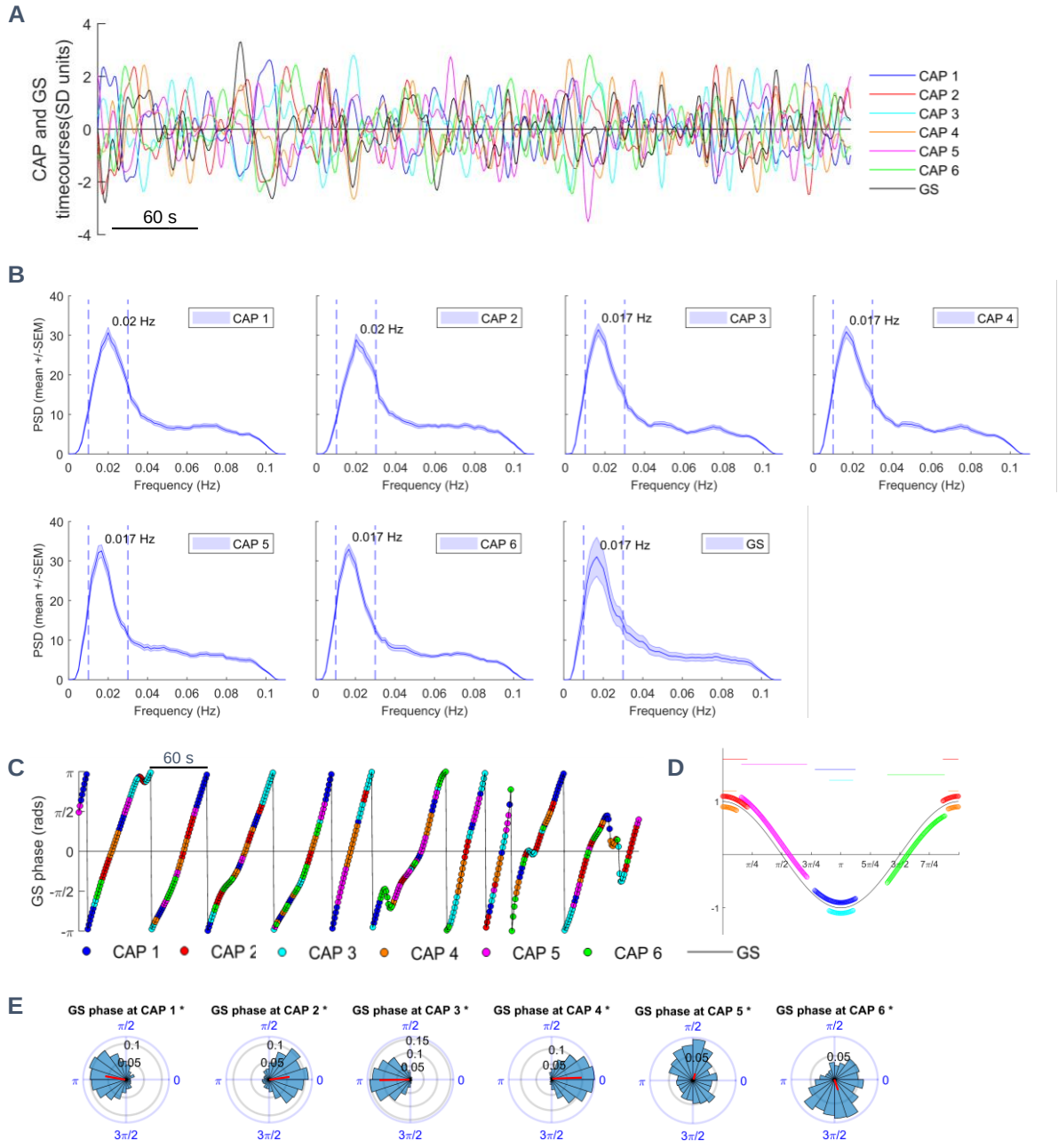

Figure 2.5: Functional states exhibit oscillatory dynamics. (A) Illustrative CAP (or the GS) time-course from in a representative subject. (B) Mean power spectral density of CAPs and the GS (mean +/- SEM). Blue dashed vertical lines delimit the 0.01-0.03 Hz frequency band employed in subsequent phase analyses. (C) Instantaneous phase of the GS in a representative subject. Colored dots mark the occurrence of each CAP. (D) CAPs occur at specific phases of global signal oscillations. Phase dispersion plotted as circular variance around the circular mean (top horizontal bars). CAP encoding is described according to color scheme in (C). (E) Circular distribution of GS phases at each CAP's occurrence within a GS cycle. For each distribution, the resulting vector (magnitude and phase) is shown as a black radial line.

Functional states transitions occur at specific phases of global fMRI signal

Interestingly, our power analyses also revealed that the fMRI global signal (GS) presents a power spectrum peak in the same infra-slow oscillatory band that characterizes CAP oscillations (**Fig 2.5-B**). This finding raises the question of how CAP oscillatory dynamics may relate to that of the GS. We hypothesized that intrinsic oscillations in GS may not reflect global, spatially undifferentiated, ups and downs of whole-brain activity, but, on the contrary, each phase of the GS may encompass the specific activation of selected subsets of possible brain states, each characterized by a characteristic profile of brain activity. To test this hypothesis, we measured the frequency of CAP occurrence at different phases of the fMRI GS oscillations, by filtering the GS signal in the infra-slow band and computing the phase at each instant (Montemurro et al., 2008). With the phase convention we used, phase values of 0 and π corresponded to peaks and troughs of the GS, respectively (**Fig. 2.5-D**). To understand whether different sections of GS oscillation cycles correspond to different states, we next computed the circular distribution of GS phases at which each CAP occurred. Notably, we found that the occurrences of all 6 CAPs were not distributed uniformly across the GS infra-slow cycle (**Fig. 2.5-C and D**). Rather, CAP occurrences were concentrated at specific ranges of the GS phase cycle, with all distributions exhibiting a significant deviation from circular uniformity (Raleigh test, $p < 0.05$, Bonferroni corrected). Specifically, CAP pairs 3 and 4 as well as 1 and 2 tended to occur around the trough and the peak of GS fluctuations, respectively (**Fig. 2.5-D and E**), albeit with different spread of phases, while occurrences of CAPs 5 and 6 were concentrated around time points in which the GS phase was $\pi/2$ and $-\pi/2$ respectively, corresponding to intermediate, off-peak GS levels. The observation that off-peak GS values correspond to a well-defined spatial structure lends strong support to our hypothesis that different phases of the GS oscillations do not reflect just spatially-unstructured ups and downs of global brain activity. The qualitative differences highlighted above were confirmed by quantitative tests, with evidence of significant differences between GS mean phases of all CAPs (Watson-Williams test, $p < 0.05$, Bonferroni corrected), with the only exception of CAPs 2 and 4.

Functional states act as coupled oscillators

Although the above analysis suggests that CAPs act as oscillating networks, it does not fully clarify whether they act independently, or as coupled oscillators that covary according to specific phase relationships between each other, and with respect to the global fMRI signal. If the latter is the case, phase relationships between CAPs must be observed not only when pooling all phase occurrences together (as in **Fig. 2.5-E**), but also when considering phase relationships between occurrences of different CAPs within the same (or immediately adjacent) GS cycle. We thus computed the GS phase angular difference between CAP occurrences in the same GS cycle or across GS cycles that were immediately adjacent in time (i.e. next or previous GS cycle, **Fig. S2.5**). We found that GS phase difference between occurrences of the same CAP (diagonal panels, **Fig. S2.5**) were concentrated around zero, suggesting that a given state appears in general for a short range of adjacent phases during a given cycle. Moreover, reciprocal CAPs appeared with a phase difference of π in the same cycle, suggesting that each GS cycle reflects at least in part the alternation between peaks and troughs of a specific spatially-structured network. Finally, we found significantly locked distribution of phase differences between non-reciprocal CAP pairs (e.g. between CAPs 4 and 5, and CAPs 3 and 6). Collectively, these results show that the identified brain-wide functional states act like coupled infra-slow oscillators, and suggest that GS fluctuations, rather than being the result of unstructured changes of activity, reflect coupled dynamics of interacting structured networks along the entire oscillation cycle.

Altered patterns of rsfMRI connectivity entail non-canonical functional state dynamics

The relationship between patterns of spontaneous fMRI activity and correlational rsfMRI network topographies (**Fig. 2.1**) offers the opportunity to reframe aberrant rsfMRI connectivity in terms of altered spatial-temporal structure of instantaneous fMRI states. As an illustrative example of this novel interpretative framework, we mapped functional states in mice haploinsufficient for the chromatin-remodeling gene Chd8. This mutation recapitulates a major genetic risk factor for autism spectrum disorders (ASD), and is characterized by rsfMRI over-

connectivity between hippocampal and motor cortical areas, as assessed with conventional steady-state rsfMRI mapping (Suetterlin et al., 2018).

As described above, brain state identification using k = 6 in control animals (Chd8+/+; n = 23) recapitulated the states observed in our two larger control datasets **(Fig. S2.1**). However, corresponding CAPs in Chd8 mutants (Chd8+/-; n = 21) were characterized by several notable non-canonical spatial features, entailing dysfunctional or aberrant engagement of specific regional substrates (**Fig. 2.6-B**, $T(40) > 2.8$, cluster corrected, $p < 0.05$). Specifically, CAPs 1 and 2 in Chd8+/- mice exhibited an aberrant reciprocal involvement of thalamic and dorsal hippocampal regions. Similarly, cingulate and mid-thalamic recruitment appeared to be defective in CAPs 3 and 4 of Chd8+/- mice and foci of aberrant motor sensory and prefrontal co-activation were found in CAPs 5 and 6. These results provide evidence of non-canonical state recruitment in mice harboring a key ASD-risk mutation.

We next investigated the presence of between-group alterations in CAP oscillatory phase dynamics (**Fig. 2.6-C**), by mapping the occurrence of each states with respect to GS phase in control and Chd8 mutants. Interestingly, we found that, although the CAPs of Chd8+/- mutants happened along the phase cycle in the same order as the corresponding state of control mice, there were significant genotype-dependent differences in CAP dynamics. Specifically, all the functional states of Chd8+/- mice exhibited a significantly delayed occurrence ($-30.9° < \Delta\varphi < -46.5°$) with respect to GS oscillation phases (**Fig. 2.6-C**, $p < 0.01$, William-Watson test), with the exception of CAP 3, in which no genotype-dependent phase delay was observed. Similarly, the distribution of phases happening within the same or adjacent GS cycles (**Fig. 2.6**) showed that all such phase distributions significantly deviate from circular uniformity in both mutant and control mice (Raleigh test, $p < 0.05$, Bonferroni corrected), showing that CAPs evolve as coupled oscillators in both cohorts. However, there was a significant genotype-dependent difference in the circular mean of the phase distributions of functional states occurring within same or adjacent cycles, with the only exception of phase relationships between CAPs 1-4 and 2-4 (Williams-Watson test, $p < 0.05$, Bonferroni corrected), with major GS phase differences occurring between CAP 3 and CAPs 4-6. Collectively, these findings suggest that ASD risk mutations can alter rsfMRI connectivity via the recruitment of non-canonical brain states, and by altering coupled oscillatory dynamics of individual brain states.

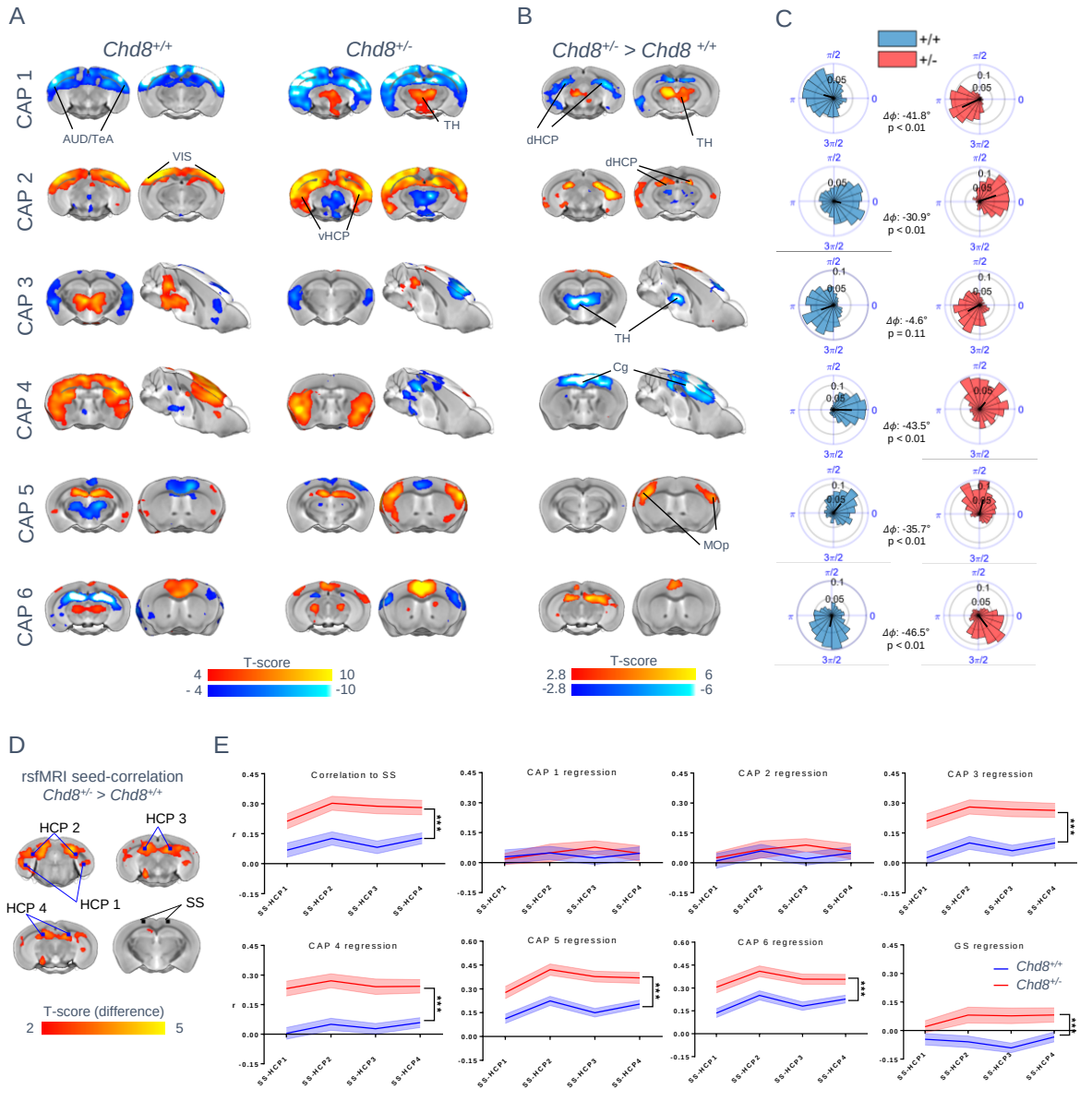

Figure 2.6: Altered brain states in a genetic mouse model of autism. (A-B) CAPs exhibit non-canonical patterns of co-activation and de-activation in Chd8+/- mutants ($p < 0.05$, FWE cluster corrected). (C) Delayed CAP occurrence within GS cycles with respect to control mice in Chd8+/- mutants ($p < 0.01$, William-Watson test for circular mean homogeneity, Bonferroni corrected, all CAPs, except for CAP3). (D). Seed-based rsfMRI correlation differences in Chd8 mutants. Inter-group differences ($p < 0.05$, FWE cluster corrected) are depicted with respect to a seed-pair in the somatosensory cortex (SS) to replicate the rsfMRI findings reported in (Suetterlin et al., 2018) . The location of hippocampal (HPC) seed used for correlational profiling is also illustrated (HPC1, 2 and 3) (E) Seed-based correlation profiling upon regression of individual CAP time-courses or the GS in both groups (*** $p < 0.001$, two-way repeated measures ANOVA, mean +/- SEM). Abbreviations: Cg – Cingulate cortex; AUD – Auditory cortex; HCP – Hippocampus; dHCP – Dorsal hippocampus; vHCP – ventral hippocampus; MOp – primary Motor cortex; SS – somatosensory cortex< TH – Thalamus.

To better relate dysfunctional state dynamics to aberrant rsfMRI connectivity as assessed with conventional correlation-based measurements, we next investigated whether specific non-canonical states could account for the increased cortico-hippocampal rsfMRI coupling previously described in Chd8+/- mice (Suetterlin et al., 2018). To this purpose, we anatomically profiled rsfMRI correlations between the affected somatosensory and hippocampal areas before and after regressing each CAP's time-course independently (**Fig. 2.6-E**). Notably, we observed that independent regression of the timecourse of either CAP 1 or 2 (a CAP, anti-CAP pair) was sufficient to eliminate inter-group differences in cortico-hippocampal rsfMRI connectivity observed with seed-based correlation analyses ($p > 0.6$, repeated measures two-way ANOVA, genotype-effect, **Fig. 2.6-E**). Regression of all the other individual states, or the GS, did not substantially affect somatosensory-hippocampal rsfMRI coupling ($p < 0.0005$, all remaining CAPs and GS, repeated measures two-way ANOVA, genotype-effect, **Fig. 2.6-E**). These results demonstrate that rsfMRI disconnectivity observed in Chd8 mutants can be explained by the involvement of brain states characterized by aberrant co-activation topographies, opening the way to an interpretative reframing of rsfMRI disconnectivity in terms of non-canonical state engagement.

2.4 Discussion

Here we describe time-varying patterns of spontaneous brain activity in terms of simple dynamical rules. We show that brain-wide patterns of fMRI activity can be classified into recurring states exhibiting coupled oscillatory activity. We further describe the temporal structure of these network transitions, and show that they occur at specific phases of global fMRI signal fluctuations, acting as coupled oscillators. We finally show that patterns of aberrant connectivity relevant for autism are associated with altered state topography and oscillatory dynamics.

Dynamic characterizations of rsfMRI signal via sliding window correlation have led to the description of spontaneous brain activity as a non-stationary phenomenon (Allen et al., 2014; Grandjean et al., 2017; Hutchison et al., 2013). Our approach expands these investigations by revealing a set of fundamental principles guiding the spatiotemporal structure of resting state

fMRI activity, implicating oscillatory transitions of recurring functional states as a fundamental level of organization of intrinsic brain activity. Importantly, the use of raw BOLD fMRI signal as the basis for the employed fMRI frame clustering provides an easily-interpretable and physiologically-relevant readout for describing time-varying patterns of spontaneous brain activity in non-correlative terms, and without computational constraints requiring the use of brain parcellations. Departing from other CAP-based approaches (Karahanoğlu and Van De Ville, 2015; Liu et al., 2013), we also introduce a series of empirical criteria to narrow down the selection of cluster numbers to increase the generalizability of our findings.

The identified brain states exhibit a composite spatial structure, providing novel insights into the macroscale functional organization of spontaneous network dynamics in the mouse brain. The presence of opposing DMN and LCN co-activation recapitulates a cardinal feature of human DMN organization (Fox et al., 2005), and supports the presence of a tight inverse coupling between these two neocortical systems (Gozzi and Schwarz, 2016; Popa et al., 2009). Interestingly, autoregressive pattern-finding algorithms have recently revealed a similarly competing relationship between DMN regions and constituents of the human task-positive network (TPN) (Yousefi et al., 2018), implicating the mouse LCN as a putative rodent homologue of the human TPN (Sforazzini et al., 2014). Importantly, the same states also provide a spatial delineation of the rodent DMN in non-correlative terms. The observed topography fully supports initial descriptions of this network to comprise in rodents thalamo-frontal as well as temporal associative and peri-hippocampal components (Gozzi and Schwarz, 2016; Sforazzini et al., 2014). The presence of opposing hippocampal and DMN activity in CAPs 5 and 6 is consistent with prior research implicating a functional interplay between these network systems in primates (Kaplan et al., 2016; Logothetis et al., 2012).

The observation of two global states characterized by widespread neocortical co-activation/de-activation provides key mechanistic clues as to the neural determinants of the oscillating states we described in this work. Optical imaging in awake and lightly anesthetized mice have revealed that spontaneous neural activity entails slow (< 0.1 HZ) neural waves spanning the entire cortex, as well as transient co-activations within neuro-anatomically constrained patterns of activity (Matsui et al., 2016; Mohajerani et al., 2010; Vanni et al., 2017). Concurrent hemodynamic and neural measurements have convincingly linked the two phenomena,

demonstrating that transient co-activations embedded in global waves are converted into hemodynamic responses travel across homotopic dorso-cortical areas (Matsui et al., 2016; Schwalm et al., 2017). This relationship has been expanded to relate cortical co-activation patterns of calcium activity with spatially-structured hemodynamic fluctuations (Matsui et al., 2018), revealing recurring dorso-cortical CAPs that remarkably reproduce the contrasting involvement of DMN and LCN areas we described here (supplementary movies 1-2, 5-6). These spatial correspondences are consistent with a neural origin of the identified fMRI states, and support a view in which brain-wide fMRI fluctuations are inherently guided by intrinsic oscillatory cycling between slowly propagating neural activity. Non-conventional analyses of human rsfMRI network dynamics support this hypothesis. For example, five recurrent network configurations have been recently described using phase coherence as instantaneous connectivity metric using a regional parcellation of the human brain (Cabral et al., 2017b). Similarly, data-driven approaches have uncovered putative temporal sequences of fMRI activity defined as lag threads of propagated fMRI signal in the human brain (Mitra and Raichle, 2016) as well as two dominant, alternating quasi-periodic patterns involving DMN and TPN regions, reminiscent of our states 1 and 2 (Belloy et al., 2018; Majeed et al., 2011; Yousefi et al., 2018). Finally, whole-brain fMRI decomposition of human rsfMRI signal into CAPs produced a set of states that, although not recognized by the authors of the work as such, exhibit mirroring spatial configurations consistent with the oscillatory dynamics we describe here (see Figure S3 in Liu et al., 2013).

It should be emphasized that the light sedation regimen employed in our mouse rsfMRI datasets preserves cortical responsivity, without producing slow-waves or cortical hyper-synchronization (Gozzi et al., 2012; Orth et al., 2006). Moreover, this regimen is associated with high network specificity, and preserves thalamo-frontal fMRI connectivity (Sforazzini et al., 2014), a functional signature that is representative of conscious states (Liang et al., 2013). These lines of evidence suggest that the states we describe here and their oscillatory dynamics are representative of the repertoire of network configurations occurring during quiet wakefulness in the resting rodent brain. In keeping with this notion, seed-based CAP mapping of prefrontal and somatosensory regions in awake, restrained rats, revealed three non-redundant

states, exhibiting remarkable spatial correspondence with our CAPs 2, 4, and 6, respectively (Liang et al., 2015)

A wave of recent investigations have linked fluctuations of the fMRI GS to vigilance (Wong et al., 2013), glucose metabolism (Thompson et al., 2016) and arousal mediated by ascending nuclei (Liu et al., 2018; Turchi et al., 2018). Our results are consistent with the hypothesis that the GS (when devoid of prominent artefactual contributions) encodes for key neuronal-relevant information, and support a view, in which each GS cycle is the sum of different, partially overlapping, network configurations. While the intrinsic drivers of these reconfigurations remain elusive, the observation of foci of co-deactivation in basal forebrain areas in CAP 3 (Fig. 2.3) recapitulates similarly contrasting patterns of global activity in cortical and basal forebrain regions observed in humans (Liu et al., 2018), and is consistent with a role of ascending modulatory activity in driving these oscillations (Turchi et al., 2018) The combined use of cell-type specific manipulations and rsfMRI (Giorgi et al., 2017) may permit to probe this mechanistic hypothesis, by enabling causal manipulations of ascending neurotransmitter systems.

Finally, the observation of altered state topography and oscillatory dynamics in a mouse line harboring an autism-associated mutation provides a novel interpretative framework for the description and interpretation of dysfunctional connectivity in brain disorders. Altered steady-state rsfMRI connectivity has been widely document in autism (Di Martino et al., 2014), and can be effectively recapitulated in mouse lines harbouring mutations in ASD risk genes (Bertero et al., 2018; Liska et al., 2017; Michetti et al., 2017; Sforazzini et al., 2016). Our findings suggest that aberrant rsfMRI functional coupling reflect non-canonical patterns of regional co-activation and impaired state dynamics, thus providing a spatio-temporal description of brain dysfunction that can be used to relate basic neurophysiological mechanism (e.g. defective neural co-activation) to the deficient inter-regional communication observed in brain connectopathies. Notably, the statistical significance of the observed inter-strain differences appear to greatly exceed the sensitivity of conventional steady-state rsfMRI mapping. This finding opens the way to the use of multi-dimensional spatio-temporal mapping as a possible, clinically relevant criterion for patient stratification. Further investigation of the neural basis of canonical and altered state dynamics are warranted to pinpoint the exact neural

drivers of these oscillating states and their aberrant topographies in models of human pathology.

In summary, our work documents a set of recurring oscillating brain states that govern the spatio-temporal organization of intrinsic brain function in the mammalian brain, allowing to describe time-varying patterns of spontaneous brain activity in terms of simple dynamical rules. These findings points at brain-wide oscillatory network activity as a fundamental level of organization of spontaneous brain activity, and add a novel interpretative dimension to the investigation of spontaneous brain activity, and its breakdown in brain disorders.

2.5 Supplementary Information

Description of CAP 7

Further partitions of our datasets into k = 7 clusters revealed another brain state which had no apparent anti-state when partitioning with higher number of clusters (k = 8 and above). This state, even though reproducible amongst dataset 1 and 2 (spatial correlation of 0.76 as shown in Figure S2.1), was not found in the third dataset, and for this reason we did not include it in the full manuscript. We map in Figure S2.3 the detailed anatomical description of all the 7 CAPs we found in dataset 1 and 2. The additional state, here denoted as CAP 7, exhibits the activation of temporal parietal areas together with deactivation of basal ganglia and the mouse insular-prefrontal salience network (Sforazzini et al., 2014). Even though it did not appear to have an anti-state, this cluster appeared to be mostly anti-correlated with CAP 1 (spatial correlation of -0.37), as shown in Figure S2.3B. It should be noted here that uncertainty as to the stability and significance of this additional state does not detract from the robustness of the six CAPs we describe in the manuscript, as all the six states were found to be present and stable in all datasets with k = 7 and 8, and as such capture neural reconfigurations dominant in the resting mouse brain.

Supplementary figures

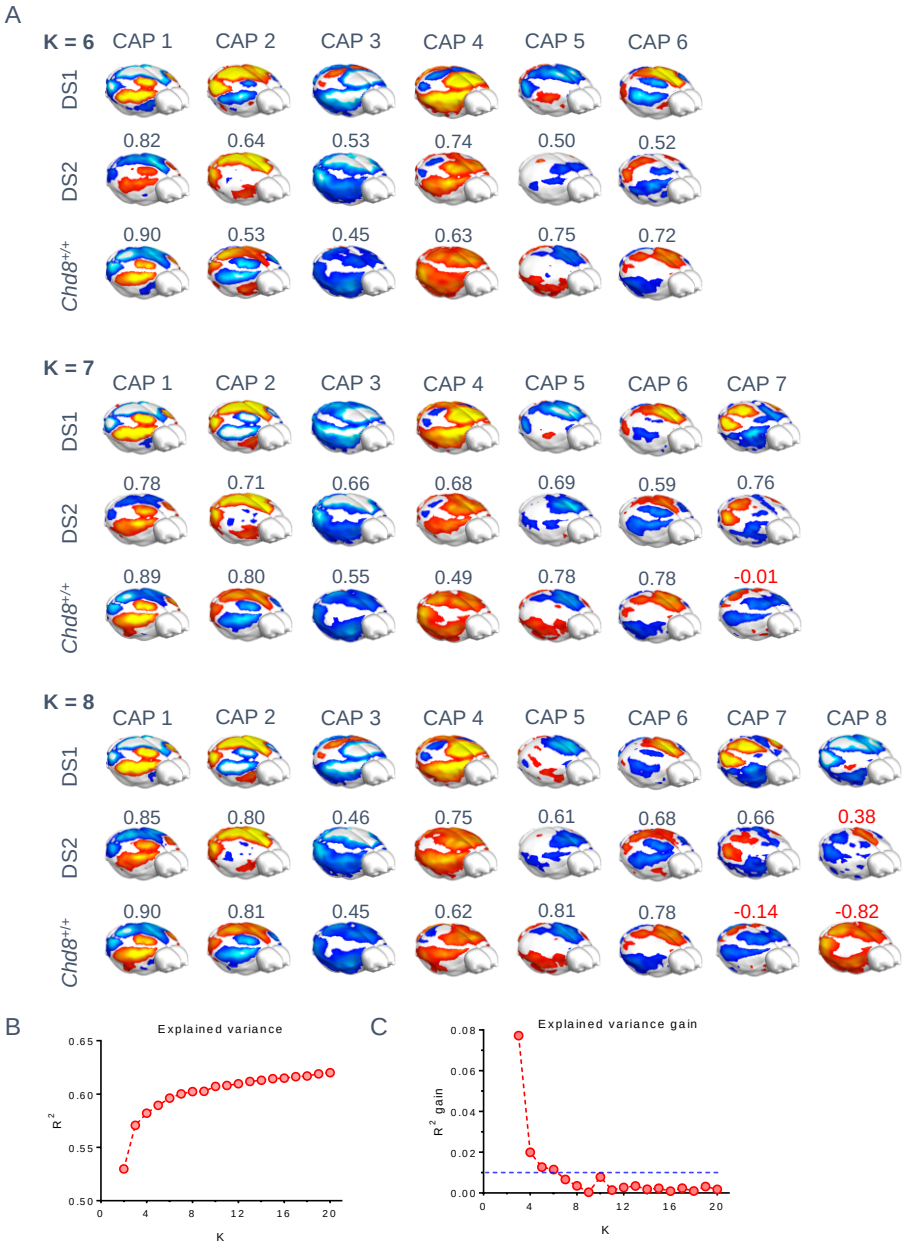

Figure S2.1: Selection of optimal number of clusters. (A) Whole-brain representations of CAPs found with k = 6, 7, and 8 in dataset 1 (n = 40, 500 fMRI frames per subject), and their matched CAPs found in dataset 2 (n = 41, 300 frames per subject) or dataset 3 (CHD8+/+ control mice, n = 23, 450 frames per subject). Note that CAPs 1-6 are recurrently found in all datasets with k = 7 and 8, while additional CAPs are less reproducible across datasets. (B) Variance explained by clustering dataset 1 with k = 2 – 20. (C) Percentage gain in variance explained when advancing from k-1 to k.

Fig. S2

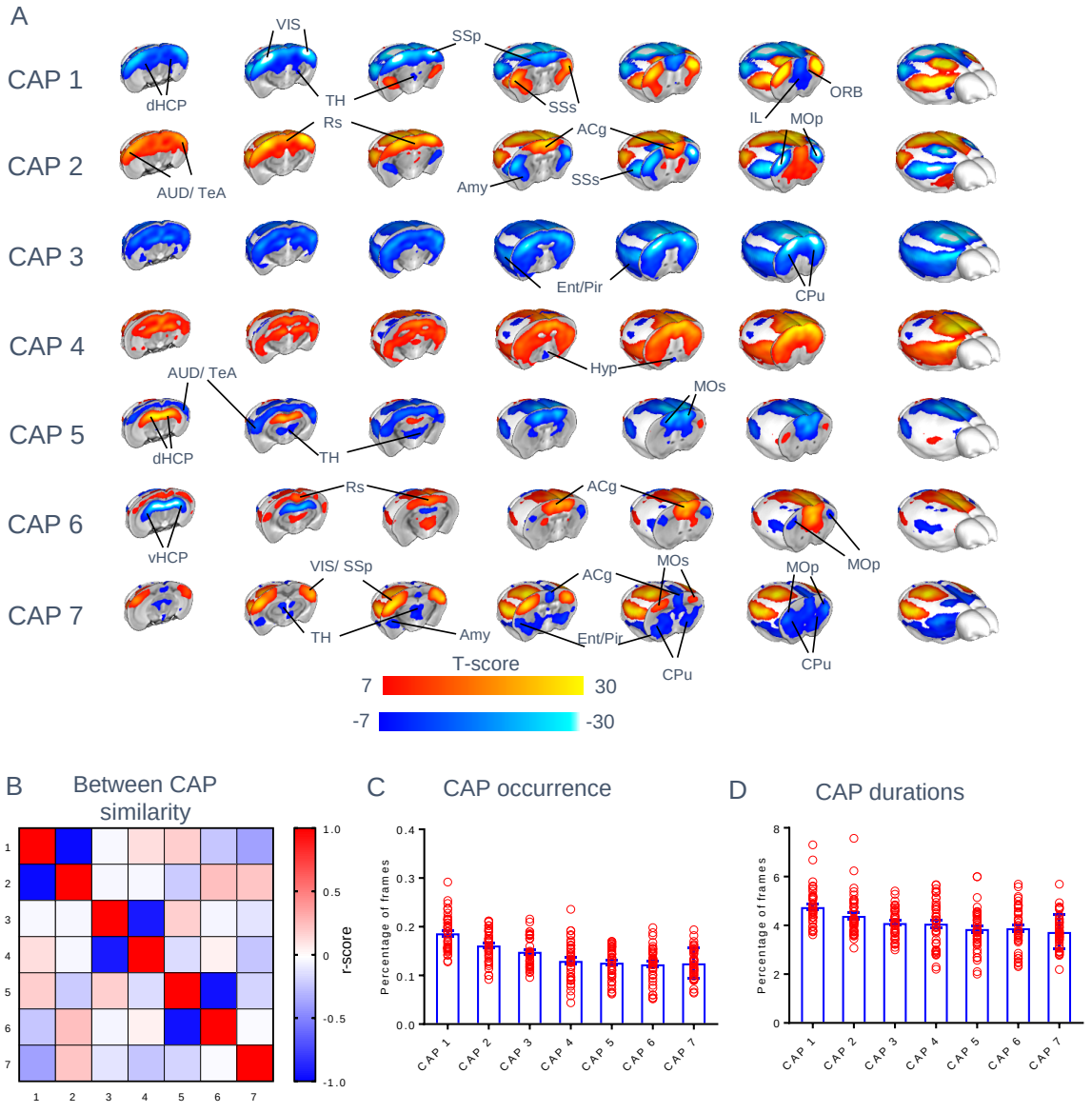

Figure S2.2: Brain states obtained with k = 7. (A) Whole brain representation of the 7 brain states (CAPs) we identified at the group level in dataset 1, using k = 7. Red/yellow indicates co-activation (i.e. high fMRI BOLD signal) while blue indicates co-deactivation (i.e. low fMRI BOLD signal) ($p < 0.01$, Bonferroni corrected). Panels (C) and (D) illustrate CAP occurrence rate and mean duration, respectively (mean +/- SEM). Abbreviations: ACg – Anterior Cingulate cortex; AUD – Auditory cortex; dHC – dorsal Hippocampus; vHC – ventral Hippocampus; HT – Hypothalamus; ILA – Infralimbic Area; LAN – Lateral Amygdalar Nucleus; MOp – primary Motor cortex; Mos – secondary Motor cortex; ORB – Orbitofrontal cortex; PIR – Piriform Area; PL – Pallidum; Rs – Retrosplenial cortex; SSp – primary Somatosensory cortex; SSs – secondary Somatosensory cortex; ST – Striatum; TeA – Temporal Association cortex; TH – Thalamus; VIS – Visual cortex.

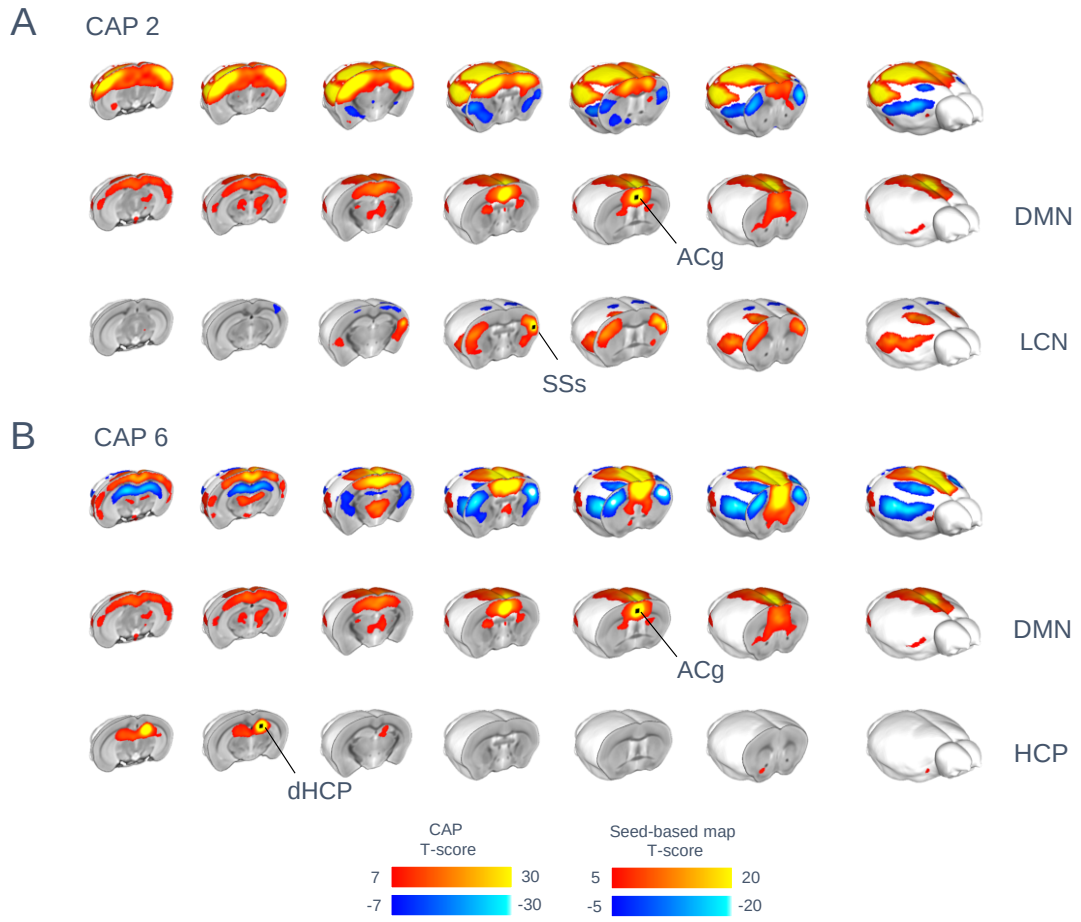

Figure S2.3: Brain functional states encompass known rsfMRI networks of the mouse brain. CAP spatial patterns (top row) can be decomposed into conventional rsfMRI network constituents generated with a seed based analysis (seed location indicated by black dots). (A) For example, CAP 2 (top row) shows co-activation of regions of the mouse DMN and co-deactivation in the mouse latero-cortical networks (LCN). Similarly, CAP 6 (B) exhibits contrasting involvement of regions of the DMN, and dorsal hippocampal network (HCP).

Fig. S4

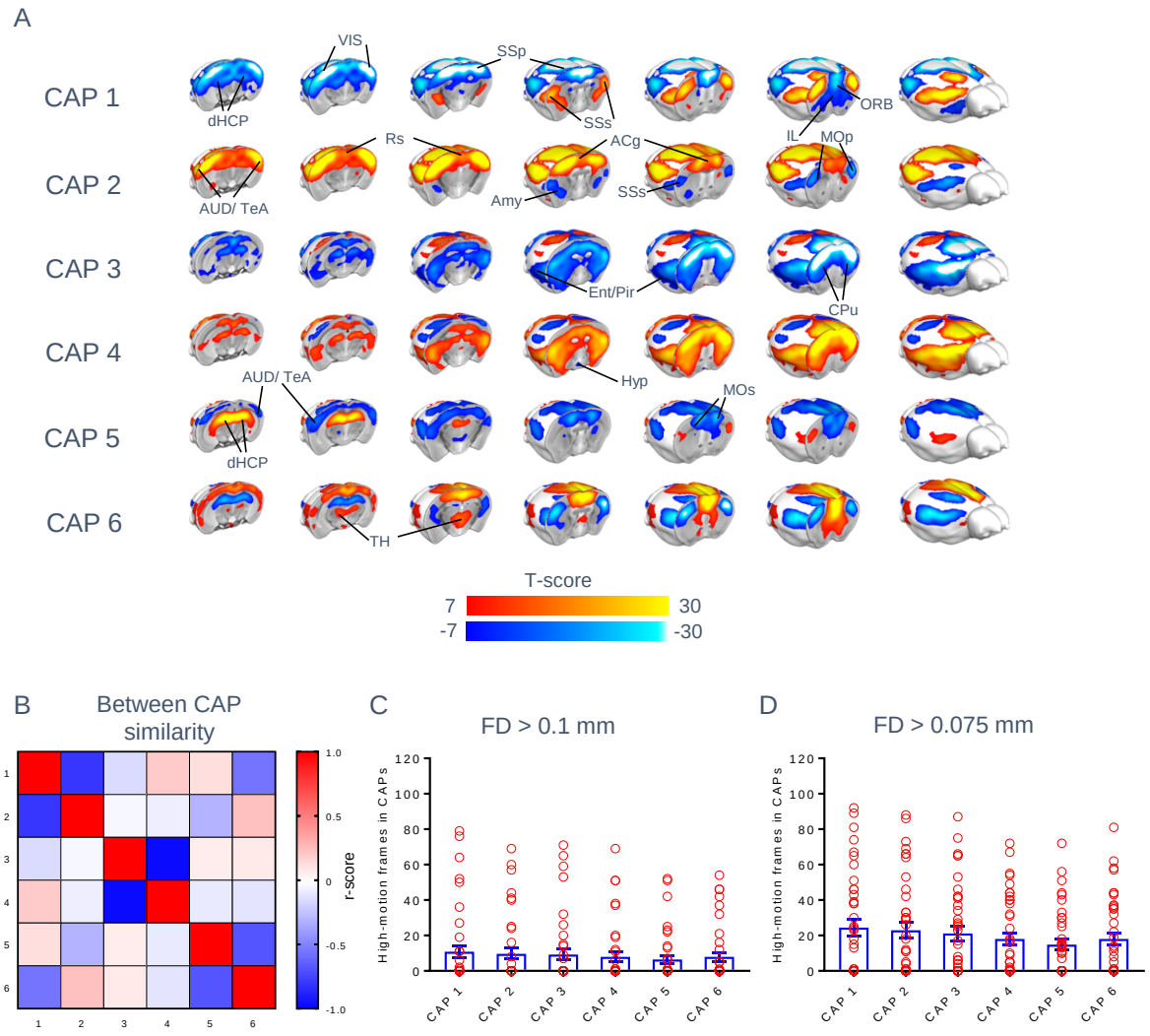

Figure S2.4: CAPs are not contaminated by motion. (A) CAPs obtained by clustering rsfMRI frames upon censoring of putative motion-contaminated frames using a frame-wise displacement (FD) threshold of 75 µm. (B) Between-CAP spatial similarly (correlation coefficient). (C-D). Distribution of putative motion-contaminated frames across CAPs at two strict FD thresholds (means +/- SEM).

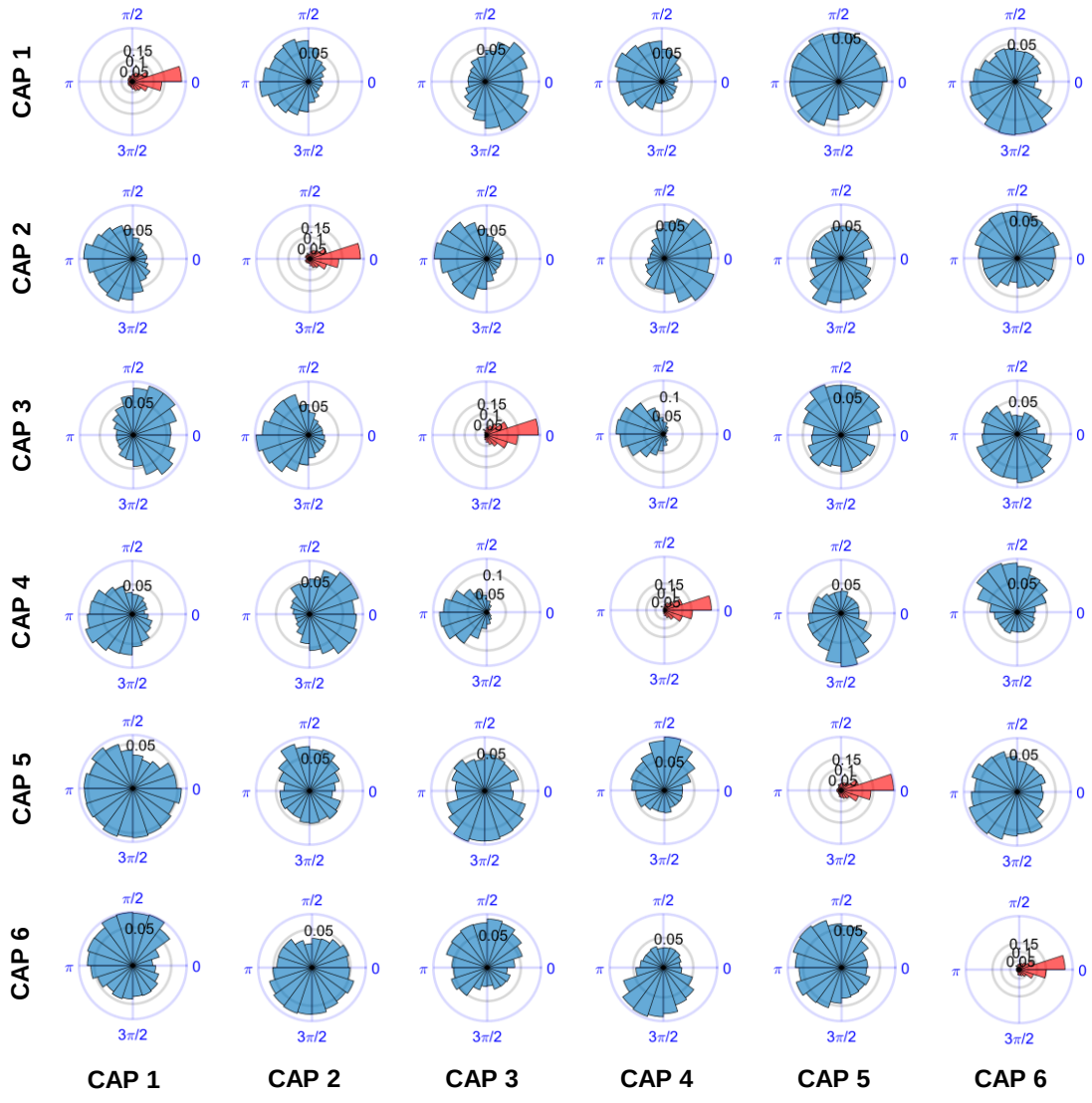

Figure S2.5: Functional states act as coupled oscillators. Global signal phase differences between CAP occurrences. Each panel corresponds to the circular distribution of GS phase differences between occurrences of a CAP inside a GS-cycle (rows), and the occurrences of another CAP within the same cycle and across GS cycles that were immediately adjacent in time (columns). All distributions significantly deviate from circular uniformity (Raleigh test, $p < 0.05$).

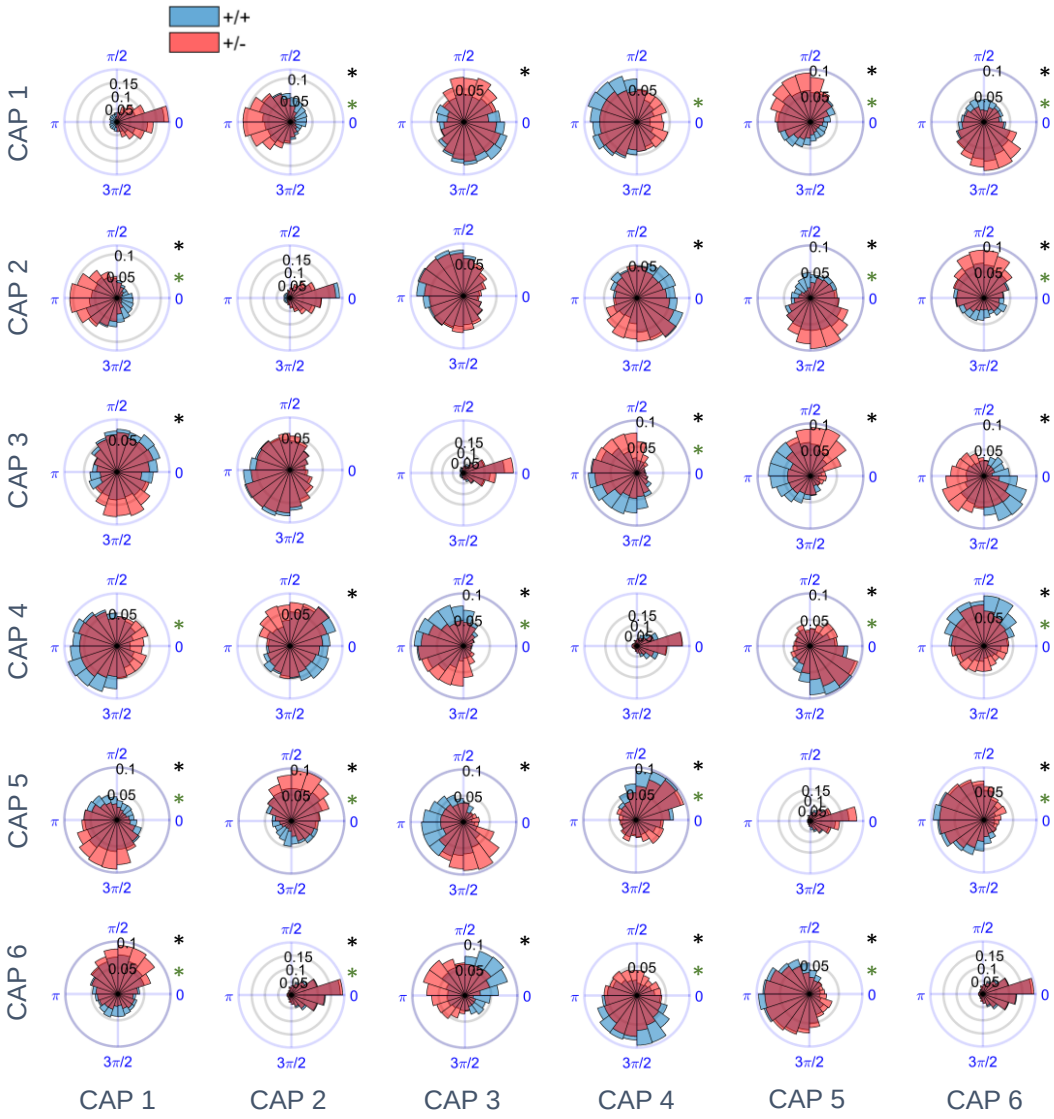

Figure S2.6: Altered GS phase difference between CAPs in a genetic model of autism. Each panel corresponds to the circular distribution of GS phase differences between occurrences of a CAP inside a GS-cycle (rows), and the occurrences of another CAP within the same cycle, and across GS cycles that were immediately adjacent in time (columns). All distributions significantly deviate from circular uniformity (Raleigh test, $p < 0.05$). Blue distributions correspond to CAPs from the control group (Chd8+/+), and red overlaid distributions correspond to CAPs from the mutant group (Chd8+/-). Black asterisks denote significant differences between circular means in each panel (William Watson test, $p < 0.05$).

Chapter 3

Pharmacological modulation of cholinergic activity alters spontaneous brain dynamics

3.1 Introduction and background.

Translational science has the goal of improving the success of pharmacological interventions to relevant patient treatments of disease. An inherent challenge in this field is the identification of translational endpoints that determine if pharmacological interventions reach the desired cellular targets, and if their intended pharmaco-dynamic effects (i.e. downstream pharmacological and physiological effects related to mechanisms or putative clinical effect) are translatable in both experimental animals, and relevant human patient populations (Wehling, 2011). Functional neuroimaging methods such as rsfMRI offer the potential to detect collective changes elicited by pharmacological interventions in brain function. This technique is characterized good spatial resolution, and can be broadly used in animal species and humans (Gozzi and Schwarz, 2016; Liska et al., 2015; Sakoğlu et al., 2011; Sforazzini et al., 2014; Woo et al., 2017). These features give rsfMRI the potential to improve translatability of pharmacological mechanism from preclinical models to clinical outcome (Gozzi and Schwarz, 2016; Liska and Gozzi, 2016; Sakoğlu et al., 2011; Schwarz et al., 2007).

Xanomeline is a muscarinic acetylcholine receptor agonist derived from a natural muscarinic agonist, arecoline, an active ingredient of betel nut. Xanomeline selectively targets cholinergic receptor subtypes M1 and M4 (Andersen et al., 2003; Mirza et al., 2006; Shannon et al., 2000). Specific properties of this active component have promoted its use to treat negative cognitive symptoms of both Alzheimer's disease and Schizophrenia (Avery et al., 1997; Bodick et al., 1997; Si et al., 2010; Wang et al., 2011), as well as behavioral disturbances in Alzheimer's

disease patients (Melancon et al., 2013). The drug has also been shown to produce parallel behavioral responses in rodents similar to those observed with traditional antipsychotic treatment (Shannon et al., 2000, 1999; Stanhope et al., 2001). These properties define xanomeline as an effective and well-characterized agent for the selective stimulation of cholinergic (muscarinic) systems in the living brain. Owing to the close link between arousal, and cholinergic activity (Turchi et al., 2018), the use of xanomeline can enable the investigation of how whether and how spontaneous brain dynamics is affected by a prominent ascending modulatory system. This question is of great relevance for the research of my PhD, in the light of the emerging evidence linking arousal to the global fMRI signal dynamics (Liu et al., 2018; Turchi et al., 2018).

In the present study, we used rsfMRI to assess the brain-wide effects of xanomeline on spontaneous low-frequency fluctuations of the BOLD signal in the mouse brain and its underlying brain-wide dynamics. We investigated how the drug affects regional hemodynamic fluctuations and their long-range interregional correlations. In addition, using the approach described in **Chapter 2** (Gutierrez-Barragan et al., 2018), we mapped the spatio-temporal network dynamics produced by acute xanomeline administration. We found that xanomeline produces a generalized reduction in the power of infra-slow fluctuations, as well as a generalized reduction in within and between network long-range rsfMRI connectivity. Importantly, we found that xanomeline alters spontaneous brain state dynamics, producing a new set of oscillatory states characterized by a predominant involvement of sensory-motor, hypothalamic and basal forebrain substrates. Our findings demonstrate that pro-arousing cholinergic stimulation alters spontaneous brain dynamics, hence link ascending neuromodulatory activity to whole-brain fMRI network dynamics.

3.2 Methods

Ethical statement

All in vivo experiments were conducted in accordance with the Italian law (DL 26/214, EU 63/2010, Ministero della Sanità, Roma) and the recommendations in the Guide for the Care and Use of Laboratory Animals of the National Institutes of Health. Animal research protocols were reviewed and consented by the animal care committee of the Istituto Italiano di Tecnologia. All surgical procedures were performed under anaesthesia.

Animal preparation and rsfMRI data acquisition

Experiments were performed on adult (12 week-old) male C57Bl6/J mice. Nineteen mice received a subcutaneous injection of vehicle (Saline), while twenty-one mice received a subcutaneous dose of xanomeline (30 mg/Kg). The animal preparation protocol for rsfMRI measurements has been described in detail elsewhere (Ferrari et al., 2012; Sforazzini et al., 2016). Briefly, mice were anaesthetized with isoflurane (5% induction), intubated and artificially ventilated (2%, surgery). The left femoral artery was cannulated for continuous blood pressure monitoring and terminal arterial blood sampling. At the end of surgery, isoflurane was discontinued and substituted with halothane (0.75%). Functional data acquisition commenced 40 min after isoflurane cessation. Mean arterial blood pressure was recorded throughout imaging sessions. Arterial blood gases (p_aCO_2 and p_aO_2) were measured at the end of the functional time-series to exclude non-physiological conditions.

MRI data were acquired with a 7.0 Tesla MRI scanner (Bruker Biospin, Milan) as previously described (Liska et al., 2015), using a 72 mm birdcage transmit coil, and a four-channel solenoid coil for signal reception. For each session, high-resolution anatomical images were acquired with a fast spin echo sequence (repetition time (TR)/echo time (TE) 1200/15 ms, matrix 192 × 192, field of view 2 × 2 cm2, 18 coronal slices, slice thickness 0.60 mm). Co-centered single-shot blood-oxygen level dependent (BOLD) EPI time-series were acquired using an echo planar imaging sequence with the following parameters: TR/TE 1200/15 ms, flip angle 30°, matrix 100 × 100, field of view 2 × 2 cm2, 18 coronal slices, slice thickness 0.60

mm, 1500 volumes and a total rsfMRI acquisition time of 30 min. All the analyses were carried out on the last 1000 timepoints (20 min), after removing the first 500 volumes previous to vehicle or xanomeline administration. Four subjects from the xanomeline group were removed due to high motion at the end of the scan as measured with Frame-wise displacement (FD > 0.1 mm in over 20% of the frames), resulting in the final xanomeline cohort being composed of n = 17 subjects.

To corroborate the reproducibility of our findings in the control (vehicle) group across independent datasets, and restrict our cluster selection procedure, we used the results obtained in dataset 1 (n = 40, 500 timepoints per subject) of **Chapter 2** (main dataset in Gutierrez-Barragan et al., 2018). As previously described, we also assessed the reproducibility with respect to two independent datasets: dataset 2 (n = 41, 300 timepoints per subject), and dataset 3 (n =23, 500 timepoints per subject).

Image data pre-processing

Data pre-processing was carried as previously described (Liska et al., 2017). Briefly, fMRI time-series were despiked, motion corrected, and spatially normalized to an in-house mouse brain template (Sforazzini et al., 2014) yielding a final normalized spatial resolution of 0.1 x 0.1 x 0.5 mm^3 (192 x 192 x 24 matrix). Head motion traces and the mean ventricular signal (average fMRI time-series within a manually-drawn ventricle mask from the template) were regressed out. The resulting images were spatially smoothed using a Gaussian kernel of 0.5 mm FWHM, band-pass filtered using a 0.01 – 0.1 Hz band, and z-scored voxel-wise.

Interregional correlations and amplitude of spontaneous low-frequency fluctuations of the BOLD signal

To explore how interregional long-range rsfMRI correlations (i.e. functional connectivity) between key network regions is affected by xanomeline treatment, we extracted the mean BOLD signal from a set of pre-defined seeds. These seeds are located within previously described network and sub-network systems of the mouse brain (Laterocortical – LCN; Default mode – DMN; Posterolateral – PLN; Hippocampus – HCP; Thalamus – TH; Hypothalamus –

HT; Striatum – STN; and Basal Forebrain – BF) (Gutierrez-Barragan et al., 2018; Liska et al., 2015; Sforazzini et al., 2014), as shown in **Figure 3.1-A**. For each subject in each group, we computed the Pearson correlation between the time-series of each pair of regions, and built mean group correlation matrices, normalized to T-scores ($p < 0.05$, FDR corrected). We then compared each edge in the graphs with a two-sample T-test ($p < 0.05$, FDR corrected), and depicted all significant correlation differences (xanomeline > vehicle) in a T-score matrix.

We next carried spectral analysis by computing the power spectrum of the BOLD signal with voxel-resolution and by computing the fractional Amplitude of Low-frequency Fluctuations (fALFF), defined here as the proportion of power in the filtered band (0.01-0.1 Hz) that is in the infra-slow band 0.01-0.03 Hz (Zou et al., 2008). Our choice of the infra-slow frequency band was guided by our previous observation that whole-brain functional states in the mouse brain undergo oscillations peaking in the considered frequency band (Gutierrez-Barragan et al., 2018) (see **Fig. 2.5B**). For visualization purposes, we also compared the power spectrum of selected regions belonging to the mouse basal forebrain.

Regional whole-brain correlations and average co-activation maps

We previously reported that networks in the mouse brain obtained with conventional rsfMRI seed-based correlation analyses can be reliably described from first order statistics (selective averaging) of fMRI frames corresponding to high regional BOLD activity (Liu and Duyn, 2013; Tagliazucchi et al., 2012). To probe whether this principle holds under xanomeline treatment, we repeated the seed-based analysis in a set of selected regions of interest (or seeds) within key anatomical substrates belonging to the Co-activation Patterns (Gutierrez-Barragan et al., 2018) (see **Fig. 2.3**). These seeds are contained within previously described network and sub-network systems of the mouse brain (Laterocortical – LCN; Default mode – DMN; Posterolateral – PLN; Hippocampus – HCP; Thalamus – TH; Hypothalamus – HT; Striatum – STN; and Basal Forebrain – BF) (Liska et al., 2015; Sforazzini et al., 2014). The employed averaging yields spatial maps of averaged spontaneous fMRI activity, which we previously termed seed-based mean co-activation patterns (SB-CAPs). For each of the probed regions, we also computed a canonical correlation map using the corresponding regional rsfMRI signal as seed. We next computed the spatial correlation between the identified SB-CAPs and

corresponding seed-based maps to assess the similarity between the patterns obtained with these two complementary approaches. This relationship was investigated across-subjects by probing SB-CAPs obtained by retaining rsfMRI frames exceeding a predefined intensity threshold, covering the whole 0-99th percentile range as previously described (Liu and Duyn, 2013). We illustrate this concept on two key integrative hubs of the mouse DMN and the LCN (Liska et al., 2015), characterized by co-activations within the prefrontal cortex (PFC), and the primary motor areas (MOp). A third region corresponding to the nucleus basalis (NB) was probed in order to assess the effect of xanomeline treatment on BOLD co-activations in acetylcholine production sites. For illustrative purposes, we generated a representative SB-CAP map for each of the regions probed by averaging all the fMRI frames with the highest 15% BOLD signal intensity across all subjects and using a T threshold of 6, corresponding to $p < 0.01$, Bonferroni corrected (Amico et al., 2014; Liu and Duyn, 2013). Finally we assessed the differences in whole-brain BOLD co-activation evoked by each region in the xanomeline group using a two-sample t-test and family-wise error (FWE) cluster correction ($p < 0.05$, cluster-defining threshold $T(34) = 3$).

Clustering of fMRI frames into co-activation patterns (CAPs)

As described in **Chapter 2**, network dynamics in the mouse brain is a non-stationary phenomenon that can be described by decomposing whole-brain fMRI activity into recurring functional states of BOLD co-activation. We applied our analytical design to both the vehicle and xanomeline groups independently (see **Fig 2.2**), leading to the identification of a set of instantaneous spatial co-activation patterns (CAPs). Following prior studies (Liu et al., 2013; Liu and Duyn, 2013), we carried out frame-wise clustering of brain-wide mouse rsfMRI images by retaining the voxels that were in the top 10% or in the bottom 5% of all BOLD signal in a single time frame, a procedure employed to minimize spurious influence of random, non-physiological signal fluctuations in fMRI time-series. The preprocessed fMRI frames were formatted into N-dimensional vectors $t = (t_1, t_2, \dots, t_T)$ with T being the number of frames, and N the amount of voxels. Such frames were clustered using the k-means++ algorithm (Arthur and Vassilvitskii, 2007), which partitions the vector-set into k clusters $C =$

$(C_1, C_2, \dots, C_k)$ such that the sum of within-cluster distances D in the following equation is minimized:

$$D = \sum_{i=1}^{k} \sum_{t_j \in C_i} d(t_j, \mu_i)$$

being μ_i the mean of the fMRI frames in each cluster C_i, and $\mathrm{d}(\mathrm{t_j}, \mu_\mathrm{i})$ the distance between the fMRI frame at time i and the cluster mean, measured as one minus the spatial Pearson's correlation coefficient.

Clustering was performed on the concatenated rsfMRI vehicle (19 subjects x 1000 frames) and xanomeline (17 subjects x 1000 frames) groups, with k ranging from k = 2 up to 20, using Pearson correlation between fMRI data in different time frames as clustering distance measure, and using 15 replicates with 500 iterations each. Following our previously designed k-selection strategy, we identified robust occurring patterns, previously employed to map robust, recurrent states in electrophysiological recordings (Logothetis et al., 2012). Briefly, we first computed, for increasing k, how much variance is explained by the clustering algorithm (**Fig. S3.1-B**), defined as the ratio between the between-cluster variance and the total variance (within-cluster + between-cluster variance). Within-cluster variance was computed as the averaged (over clusters) sum of square distances between elements in a cluster and its centroid. Between-cluster variance was computed as the averaged square distance between a cluster centroid and the centroid of all clusters or centroid of all data (Goutte et al., 1999). Higher values of explained variance correspond to a better description of the dataset, and that optimal k values can be identified in the "elbow" region of the explained variance plot, after which only marginal variance is gained by further refining the partition.

We thus selected the value k as the largest value within the elbow region that insured full reproducibility of the corresponding CAPs with the ones found in three independent datasets (**Fig S3.1**). To this purpose, we progressively increased k until (a) the dataset variance explained by k clusters was larger than the variance explained by k-1 clusters and (b) a replication of the clustering procedure on three additional independent rsfMRI datasets (n = 40, 500 time points, n = 41, 300 frames, and n = 23, 500 frames, corresponding to datasets 1, 2, and 3 in **Chapter 2**, respectively), would result in anatomically equivalent co-activation

patterns (defined as between dataset CAP correlation > 0.45, which corresponds to a highly significant correlation, $p < 10^{-5}$, permutation test, **Fig S3.1**) (Gutierrez-Barragan et al., 2018). This procedure identified k = 6 CAPs conserved across all the three rsfMRI datasets (**Fig. 3.3** and **Fig S3.1**). To compute the centroid of each cluster (which we took as a CAP), the fMRI frames assigned to each cluster were averaged voxel-wise, and normalized to T-scores ($p < 0.01$, Bonferroni corrected), permitting to visualize the mean voxel-wise distribution of fMRI BOLD signal for each of the identified CAP. For visualization purposes, the obtained maps were thresholded to T-scores > 6, corresponding to a $p < 0.01$, Bonferroni corrected. For each CAP we next computed its occurrence rate (i.e. the proportion of frames assigned to each CAP) and duration (i.e. the average number of consecutive frames belonging to the same CAP at each occurrence) for each of the 19 vehicle and 17 xanomeline -treated subjects. We also computed between-CAP spatial similarity, defined as pair-wise spatial correlation between all the identified CAPs.

Dynamic characterization of Co-activation Patterns and their relation with Global fMRI signal fluctuations

Following our analytical approach, we investigated the dynamics of CAPs from each group by first computing a CAP time-course, by considering spatial correlations in each time-frame as the Pearson correlation between the centroid of the considered cluster and the masked fMRI activity in the time frame of a given subject as previously described (Liang et al., 2015). We then assessed the temporal structure of CAP time-courses for each subject by computing its power spectrum. In order to compare global fMRI fluctuations (GS) in each dataset, we also computed the power spectrum of the GS in each subject of each dataset, and its respective fALFF, and evaluated significant group differences in fALFF by means of two-sample t-test.

We assessed how CAP occurrences in each group were embedded within GS oscillations by sampling the GS instantaneous phase at a CAP's occurrence. To compute the instantaneous phase of the GS in the infra-slow oscillation range, we first band-pass filtered the GS time-courses between 0.01-0.03 Hz using Matlab's filtfilt zero-phase forward and reverse digital

filter of order 20. We then used the Hilbert Transform (Montemurro et al., 2008) to decompose the GS signal into an analytical signal with a characteristic instantaneous phase and amplitude. We divided each subject's instantaneous GS phase signal into cycles in the range [0, 2π], and within each cycle, collected the GS phase values at each CAP's occurrence. Using the same filter design described above, we filtered and again normalized the CAP time-courses and sampled the GS phase at each CAP occurrence only when the CAP time-course at that instant was above 1 SD, in order to assure that the frame pertained to the specific CAP. Using the Matlab CircStats toolbox (Berens et al., 2009), we next computed circular mean and concentration parameters of the obtained distribution of GS phases at each CAP. Finally, in order to probe the presence of phase-coupling between CAP occurrence and GS oscillatory dynamics, we computed the angular differences (phase differences) of the GS phase between occurrences of a given CAP within a GS cycle, and occurrences of another CAP within the previous, current, and subsequent cycle. Again, GS phase samples at each CAP were only considered if their filtered values at that instant were above 1 SD at the corresponding instances.

3.3 Results

Pharmacological stimulation of cholinergic activity reduces long-range fMRI synchronization and decreases the power of low-frequency BOLD fluctuations

To probe the effect of xanomeline of steady-state rsfMRI fluctuations we selected a set of regional seeds (3 x 3 x 1 voxels) covering known rsfMRI networks systems of the mouse brain within each of these systems. **Figure 3.1-A** shows the anatomical location of the selected seeds. Each seed is color coded to the functional system or network it belongs to accordingly brain (blue: Latero-cortical Network-LCN; green: Postero-lateral Network-PLN; blue: Default-mode Network-DMN; yellow: Thalamus-TH; purple: Hippocampal Network-HCP; black: Striatum-STN; light blue: Hypothalamus-HT; orange: Nucleus Basalis-NB). The Pearson correlation between the extracted time-courses of each seed were computed for each subject in each group, and their mean was normalized to T-scores (T-test, $p < 0.05$, FDR corrected). Differences between the vehicle and xanomeline were then computed and mapped (two-sample T-test, $p < 0.05$, FDR corrected). **Figure 3.1-B** shows (left and middle panels) the mean rsfMRI connectivity matrix for the control and xanomeline -treated cohort, as well as its corresponding inter-group differences. This analysis highlighted a generalized reduction in rsfMRI connectivity upon xanomeline administration. The observed connectivity decrease was particularly strong within the latero-cortical, postero-lateral, default-mode, and hippocampal networks, as well as in most of the sampled regions within the striatum.

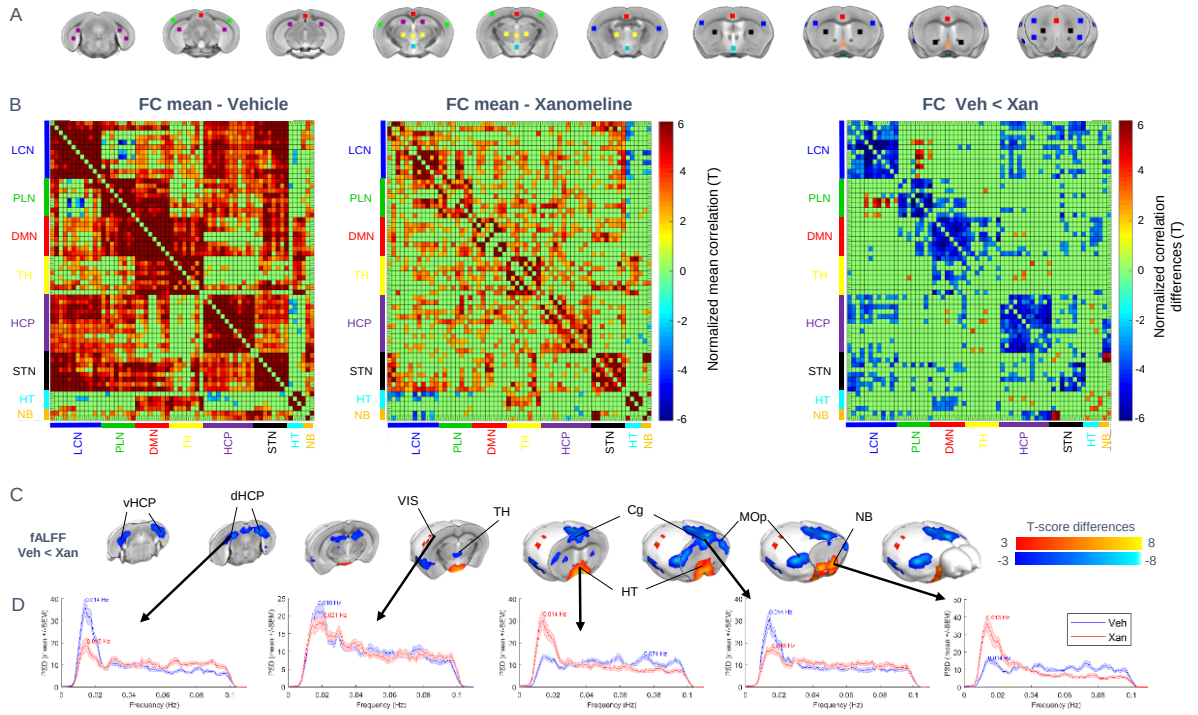

Figure 3.1: xanomeline induces rsfMRI desynchronization reduces amplitude of low frequency BOLD fluctuations. (A) Anatomical location of selected seeds corresponding embedded in known functional systems in the mouse brain (blue: Latero-cortical Network-LCN; green: Postero-lateral Network-PLN; blue: Default-mode Network-DMN; yellow: Thalamus-TH; purple: Hippocampal Network-HCN; black: Striatum-STN; light blue: Hypothalamus-HT; orange: Nucleus Basalis-NB). (B) Between-seed normalized mean correlation (functional connectivity) of vehicle (left) and xanomeline (middle) treated animals (T-test, $p < 0.05$, FDR corrected), and mean between group difference (right) in correlation (two-sample T-test, $p < 0.05$, FDR corrected). Non-significant edges were not displayed. (C) Amplitude of Low-frequency Fluctuations (ALFF, 0.01-0.03 Hz band) difference map (vehicle vs. xanomeline) treated-mice (two-sample T-test, cluster-corrected, $p < 0.01$, T-threshold = 2.8). (D) Mean group level power-spectra for selected regions exhibiting significantly higher (dHCP, Cg), lower (HT, NB) fALFF in in the control group with respect to xanomeline. An example of a region exhibiting non-significant fALFF changes is also plotted (visual cortex). Abbreviations: Cg – cingulate cortex; dHCP – dorsal hippocampus; HT – Hypothalamus; MOp – primary motor area; NB – nucleus basalis; TH – thalamus; vHCP – ventral hippocampus; VIS – visual cortex.

Spontaneous low-frequency fluctuations of BOLD signal constitute the backbone of resting state network dynamics as measured with rsfMRI (Damoiseaux et al., 2006). In **Chapter 2** we report that whole-brain co-activation patterns undergo oscillations peaking in the 0.01-0.03 Hz band. We assessed the fractional power of computing fractional ALFF, defined as the ratio of the power in the 0.01-0.03 Hz, and the total power in the 0.01-0.1 Hz band. **Figure 3.1-C** shows a heat map describing inter-group changes in fALFF (two-sample t-test, family-wise error

(FWE) cluster correction, $p < 0.05$, cluster-defining threshold $T(34) = 3$). We found foci of reduced fALFF in xanomeline -treated mice peaking in prefrontal cortical sites in primary motor areas as well as thalamus and hippocampus. Interestingly, fALFF appears instead to be robustly and consistently increased in the hypothalamus and the basal forebrain of xanomeline –treated mice (**Fig 3.2-D**). Interestingly, we did not observe significant changes in the amplitude of infra-slow spontaneous BOLD oscillations within most somatosensory regions. Collectively, these results suggest that ascending cholinergic activity results in robust rsfMRI desynchronization, an effect associated with increased local hemodynamic fluctuations in basal forebrain areas, and reduced fluctuations nuclei in the hypothalamus and the basal forebrain engage in consistently stronger hemodynamic fluctuations under the effect of Xanomeline, while significantly reducing fluctuations in specific neocortical and hippocampal substrates

To visualize the local and global effects of xanomeline on regional co-activations with voxel resolution, we next mapped the mean whole-brain co-activations of the fMRI frames corresponding to the highest 15% BOLD activity of a seed. We previously showed that these seed-based mean CAPs (SB-CAPs) retrieve seed-based correlation maps (Gutierrez-Barragan et al., 2018). Consistent with our previous findings, we found that canonical rsfMRI networks, such as the mouse DMN and LCN (Liska et al., 2015) are reliably reproduced by averaging a limited number (e.g. 15%, **Fig. 3.2**) of fMRI frames exhibiting peak BOLD activity in corresponding anatomical seed locations.

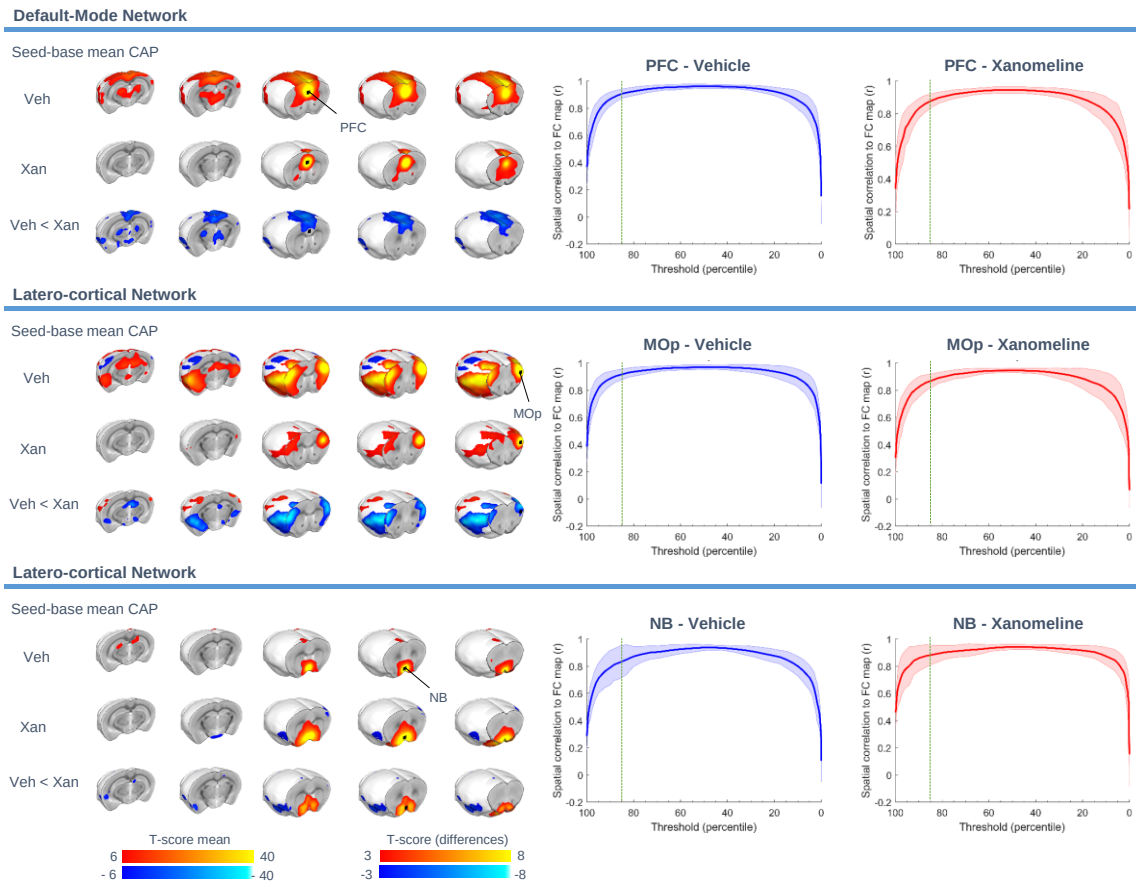

Figure 3.2: Seed-based mean CAPs and spatial similarity to seed-based correlation maps. Maps were computed by averaging for each subject, the fMRI frames corresponding to the 15% highest seed BOLD activity. Each map was computed independently for each treatment group, and the group mean was normalized to T-scores (T-test, $p < 0.01$, Bonferroni corrected). Difference maps are also shown in T-scores (two-sample T-test, cluster-corrected, $p < 0.01$, T-threshold = 2.8). Panels on the right show the mean correlation between seed-based mean CAPs and their corresponding seed-based correlation maps at increasing percentage of frames using for the calculation of the mean CAP. Green dashed lines denote the 15% threshold used for voxel-based mapping. Abbreviations: MOp – primary motor area; NB – nucleus basalis; PFC– prefrontal cortex.

In accordance with our previous findings, seed-based mean CAPs in control mice recapitulate previously described resting state networks of the mouse brain such as the DMN and LCN. **Figure 3.2** also shows that xanomeline administration results in reduced long-range cortical connectivity (and co-activation) of key integrative nodes of the mouse brain, such as the prefrontal cortex (top panel). Interestingly, co-activations with a seed in the basal forebrain (NB) revealed an opposite effect, involving the extended co-activation of basal forebrain areas upon xanomeline administration. The selection of this seed region is based on the notion that most acetylcholine producing sources in the rodent brain reside in these nuclei, and project to cholinergic sites in the cortex, which xanomeline targets agonistically via M1 and M4

receptors. These results corroborate the notion that cholinergic activation results in an overall long-range rsfMRI desynchronization of neocortical regions, and suggest that that this effect is accompanied by an increased network structure in basal forebrain areas.

Whole-brain fMRI frame clustering

The observed local and global changes in rsfMRI coupling may affect whole-brain spatio-temporal network dynamics. To investigate this aspect and asses how cholinergic stimulation affects recurrent rsfMRI configurations, we applied the approach described in **Chapter 2**, and the strategy to select the appropriate amount of clusters (Gutierrez-Barragan et al., 2018). Specifically, we first computed, for increasing k, how much variance is explained by the clustering algorithm for both the control (vehicle) and xanomeline groups (**Fig. S3.1-B**). The explained variance curve revealed in both cohorts an elbow region encompassing the range k = 4 – 8, within in which variance was still increasing (thus using more cluster yielded a better description of the datasets), but its increase was progressively smaller (denoting that the importance of adding more clusters was getting smaller and smaller, **Fig. S3.1-B and C**). We next selected the value k as the highest value within the elbow region that still ensured maximal between-dataset reproducibility of the corresponding CAPs with respect to the three datasets previously used in **Chapter 2** (dataset 1: n = 41, dataset 2: n = 23, and dataset 3, n = 23, respectively).

With this procedure, we identified in the vehicle cohort k = 6 states which are robustly conserved across the three reference rsfMRI datasets, and necessary for describing the datasets with high accuracy (**Fig. 3.3** and **Fig. S3.1**). Further credibility for the robustness of these six states as sets of genuinely coactive fMRI voxels was lent by the observation that gradually increasing the number of clusters (k) beyond k = 7 resulted in a gained explained variance consistently lower than 1% (**Fig. S3.1-C**), and that these 6 patterns were present also when partitioning the datasets into a higher number of clusters (**Fig. S3.1**). The same number of clusters was also retained for the xanomeline group, given the similar profile of explained variance curve across treatment groups. In this latter group of subjects, we however could not

use similarity with previously described CAPs as a selection criterion, given that the spatial topography of some the observed states was different from what observed in control conditions (see below). We also note here that an additional possibly stable seventh cluster was observed in both datasets. This additional state is not formally described here as it was found to be less stable across datasets as previously described (Gutierrez-Barragan et al., 2018).

Pharmacological stimulation of cholinergic system alters functional state topography

An illustration of the six identified states in both groups is reported in **Figure 3.3**. One defining characteristic of all the six CAPs in the vehicle dataset is, as was found in **Chapter 2**, is their configuration as a composite assembly of regional substrates encompassing previously described distributed resting-state networks of the mouse brain. We will not provide here a detailed description of CAPs 1-6 in the control group, as they recapitulate features we widely described in **Chapter 2**. Importantly, rsfMRI clustering of the xanomeline (**Fig. 3.3-B**) dataset revealed a new set of recurrent co-activation states, most of which demonstrate the involvement strong co-activations and co-deactivations of the basal forebrain, hypothalamus, and postero-lateral cortical regions. Specifically, CAP 1 revealed a co-activation of the prefrontal cortex with selected areas the primary motor system, part of the LCN; weak co-deactivation of posterolateral regions; and strong co-deactivations of throughout the basal forebrain and hypothalamus. A spatially opposite pattern was observed in CAP 2. CAP 4 revealed, as in the Vehicle dataset, generalized global cortical co-activations, but with robust BOLD co-deactivations in the hypothalamus and thalamus. Once again, CAP 3 showed an opposite pattern of co-activation. CAP 5 showed strong and distributed co-deactivations of the basal forebrain, the striatum, and hypothalamus, accompanied by co-activations in postero-lateral somato-sensory substrates. The presence of divergent spatial features between these caps is corroborated by the low spatial correlation when matched using the Hungarian algorithm (CAPs 1-6, 0.28, 0.41, 0.52, 0.69, 0.31, and 0.28, respectively).

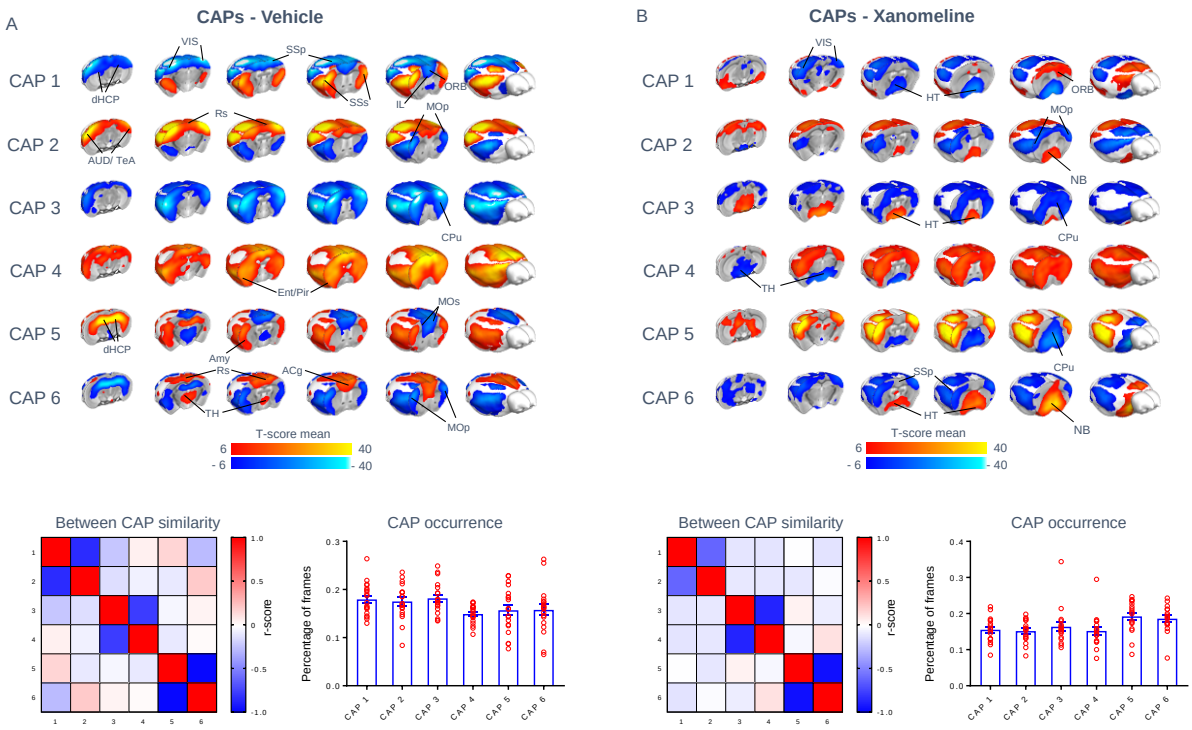

Figure 3.3: Xanomeline administration alters functional states topography in the mouse brain. (A) Whole-brain CAP representations in the vehicle dataset recapitulate six reproducible functional states previously described in the mouse brain. Red/yellow indicates co-activation (i.e. high fMRI BOLD signal), while blue indicates co-deactivation (i.e. below baseline fMRI BOLD signal) ($p < 0.01$, Bonferroni corrected). CAPs have been ordered based on their spatial properties by numbering consecutively states characterized by opposing BOLD co-activation patterns (i.e. 1-2, 3-4 and 5-6), as denoted by the negative correlations in the lower panel. (B) CAPs in the xanomeline dataset represent a set of independent states of average BOLD activity ($p < 0.01$, Bonferroni corrected), organized into pairs of opposing BOLD co-activation patterns (i.e. 1-2, 3-4, and 5-6), with most of them having non comparable spatial features to the vehicle CAPs. Only CAPs 3 and 4 share a relative spatial similarity and comparable network interventions. Abbreviations: ACg – Anterior Cingulate cortex; AUD – Auditory cortex; CPu – Caudate-Putamen; dHCP – dorsal Hippocampus; vHCP – ventral Hippocampus; HT – Hypothalamus; ILA – Infralimbic Area; LAN – Lateral Amygdalar Nucleus; MOp – primary Motor cortex; MOs – secondary Motor cortex; ORB –Orbitofrontal cortex; PIR – Piriform Area; PL – Pallidum; Rs – Retrosplenial cortex; SSp – primary Somatosensory cortex; SSs – secondary Somatosensory cortex; ST – Striatum; TeA – Temporal Association area; TH – Thalamus; VIS – Visual cortex.

To assess how different network systems contribute to the new set of functional states observed in xanomeline -treated mice, we performed an empirical decomposition of xanomeline CAPs into some putative constitutive networks using seed-based CAPs (see **Fig 3.2**) as a proxy for seed-based correlation maps. We illustrate these correspondences for CAPs 1,2, 5, and 6 in **Figure 3.4**.

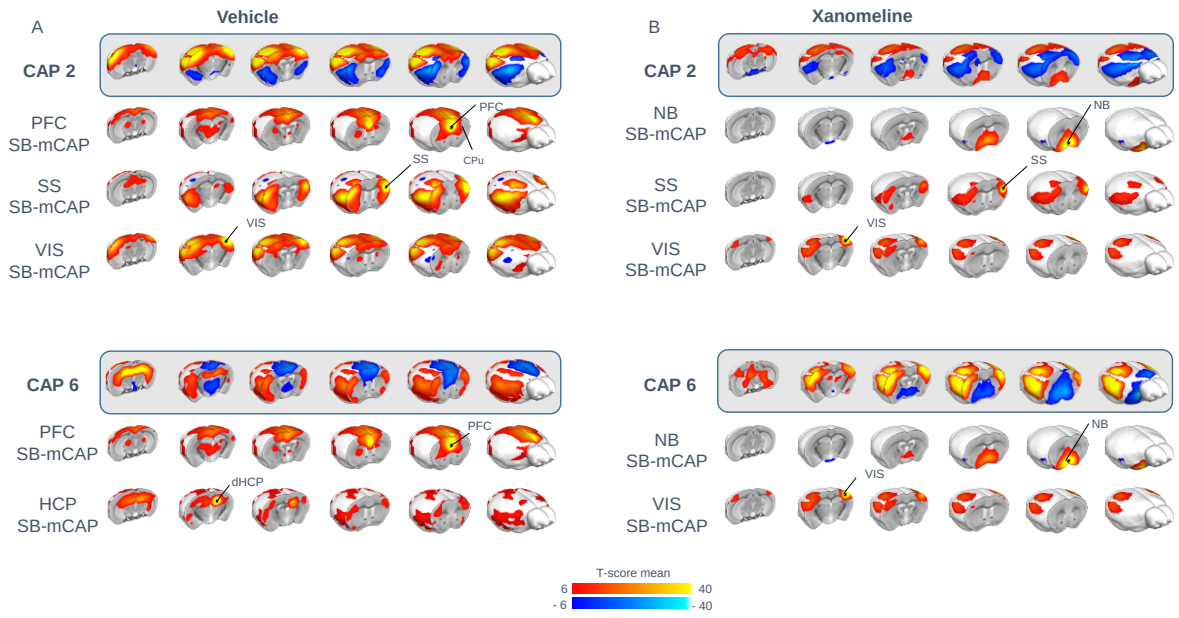

Figure 3.4: Decomposition of CAPs into putative constituent network systems. (A) CAPs (enclosed within shaded area) can be decomposed into candidate rsfMRI network constituents generated with a seed based mean CAP analysis (seed location indicated by black dots). For example, CAP 2 (top row) shows co-activation of regions of the mouse DMN and co-deactivation in the mouse latero-cortical networks (LCN). Similarly, CAP 6 exhibits contrasting involvement of regions of the DMN, and dorsal hippocampal network (dHCP). (B) CAPs in xanomeline-treated animals can similarly decomposed into a set of functional systems, which however differ from what observed in control animals. For example, CAP 2 shows co-activation of basal forebrain, hypothalamus, and postero-lateral network (PLN) regions, and co-deactivations of select regions of the LCN. CAP 6, shows prominent co-deactivation of the basal forebrain, hypothalamus, but with opposite co-activation of the PLN system.

As mentioned above, major differences in the network's configuration of the observed functional states were apparent. For example, in CAP 2, as opposed to a co-activation of the DMN and PLN as observed in control mice, xanomeline administration resulted in a strong co-activation of the basal forebrain and reduced involvement of prefrontal nodes of the mouse DMN. Similar rearrangements were observed in CAP 6. Taken together, these results suggest that cholinergic modulation of spontaneous neural activity significantly alter the topography of functional fMRI states.

A key feature of the CAPs found in both groups is their configuration into state and anti-state pairs characterized by opposing patterns of functional co-activation (**Fig. 3.3**). In keeping with our previous results, this feature was prominent in CAPs 1-2 (r = -0.-83), CAPs 3-4 (r = -0.77), and CAPs 5-6 (r = -0.97) of the control vehicle group) and CAP pairs 1-2 (r = -0.61), CAPs 3-

4 (r = -0.86), and CAPs 5-6 (r = -0.94) of xanomeline treated animals. The presence of diametric functional configurations is in keeping with our previous reporting of oscillatory dynamics in rsfMRI functional states. We again tested this assumption here by computing the power spectrum of CAP time-courses, which we built by computing the instantaneous spatial correlation of a CAP centroid to each fMRI frame (**Figure 3.5).** In excellent agreement with our previous findings, all CAPs exhibited oscillatory activity with clear peaks of power within the infra-slow 0.01-0.03 Hz band (**Fig 3.5-A and B**).

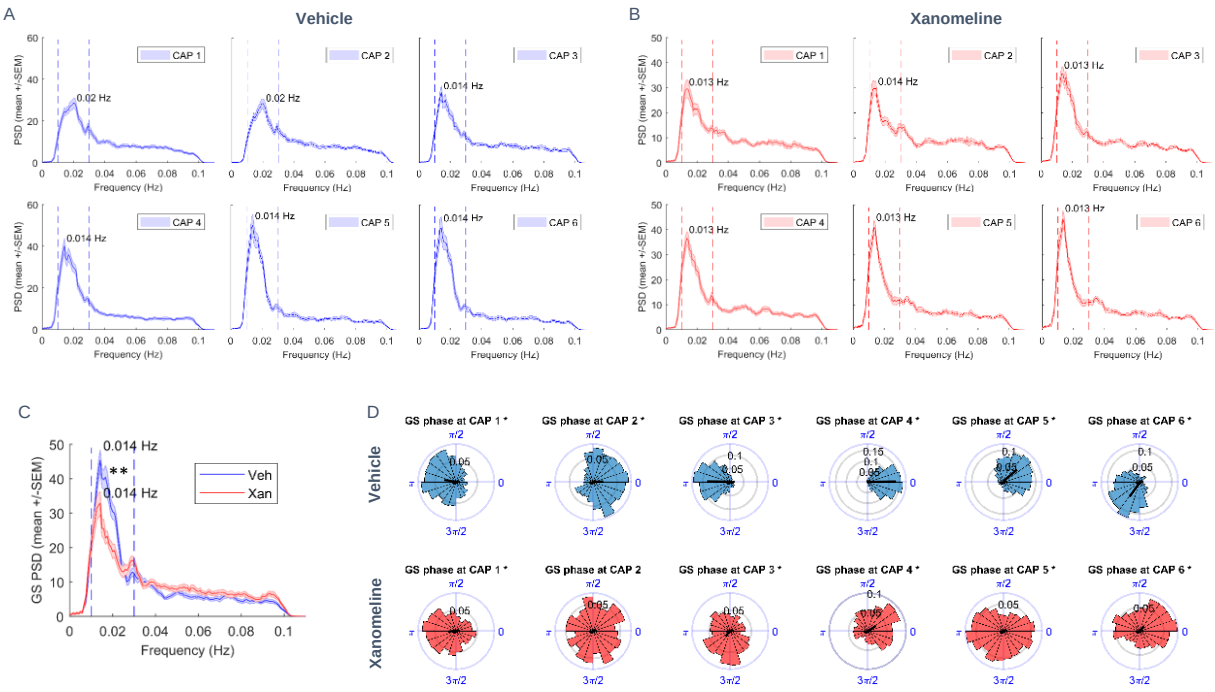

Figure 3.5: All the identified functional states exhibit oscillatory dynamics. (A) Mean power spectral density of CAPs (mean +/- SEM) from the Vehicle (blue) group and (B) xanomeline (red) groups. Dashed vertical lines delimit the 0.01-0.03 Hz frequency band employed in subsequent phase analyses. Inset numbers represent the peak frequency. (C) Mean power spectral density of the GS (mean +/- SEM) from the Vehicle (blue) and xanomeline (red) groups, showing a significant decrease in fALFF of the GS in the xanomeline group (** p = 0.002). (D) Circular distribution of GS phases at each CAP's occurrence within a GS cycle in each group. For each distribution, the resulting vector (magnitude and phase) is shown as a black radial line. GS phase distributions at the occurrence of all CAPs significantly deviated from circular uniformity, with exception of CAP 2 in the xanomeline group (Raleigh test, * p < 0.01, Bonferroni corrected).

Our power spectrum analyses also revealed that the global fMRI signal (GS) undergoes oscillations peaking in the 0.01-0.03 Hz range (Fig. 3.5 C) as we previously described(Gutierrez-Barragan et al., 2018). We however observed a significant decrease in the

amplitude of infra-slow oscillations (fALFF) in xanomeline treated mice, as measured by the fractional amplitude of low frequency oscillations ($p = 0.002$).

These findings again raise the question of how CAP oscillatory dynamics may relate to that of the fMRI GS. We already tested the hypothesis that intrinsic oscillations in GS may not reflect global, spatially undifferentiated, ups and downs of whole-brain activity, but, on the contrary, each phase of the GS may encompass the specific activation of selected subsets of possible brain states, each characterized by a characteristic profile of brain activity (Gutierrez-Barragan et al., 2018). To test again this hypothesis on the control dataset, we measured the frequency of CAP occurrence at different phases of the fMRI GS oscillations, by filtering the GS signal in the infra-slow band and computing the phase at each instant (Montemurro et al., 2008). With the phase convention we used, phase values of 0 and π correspond to peaks and troughs of the GS. To understand whether different sections of GS oscillation cycles correspond to different states, we next computed the circular distribution of GS phases at which each CAP occurred. Consistent with our previous findings, CAP occurrences in control animals were concentrated at specific ranges of the GS phase cycle, with all distributions exhibiting a significant deviation from circular uniformity (Raleigh test, $p < 0.05$, Bonferroni corrected). Specifically, CAPs pairs 3 and 4 as well as 1 and 2 tended to occur around the trough and the peak of GS fluctuations, respectively (**Fig. 3.5-D**, top panels). As previously reported, CAPs 5 and 6 tend to occur at intermediate off-GS peak levels, near $\pi/2$ and $-\pi/2$ respectively.

By contrast, brain states under xanomeline exhibited a widely more distributed occurrence across phases of GS cycles (**Fig. 3.5-D**, bottom panels). For example, while CAP 1 tends to occur more frequently at troughs of the GS, a smaller but non-negligible proportion of its occurrences took place also at GS peaks. Similarly, CAP 2 does not show a significant deviation from circular uniformity (Raleigh test, $p = 0.17$), and hence appears with equal probability across all phases of the GS cycle. CAPs 5 and 6 tend to appear in a bimodal fashion at peaks and troughs of the GS cycle, but still hold a significant deviation from circular uniformity. We finally observed that CAPs 3 and 4, which are spatially reminiscent of analogous patterns of global cortical co/deactivation observed in control animals, exhibited a more widespread range of phases (Kappa-test, $p < 0.01$, Bonferroni corrected), and tend to

occur with a mean delay of 58° and 35° with respect to their corresponding GS troughs and peaks, as compared with control animals, respectively.

Functional states act as coupled oscillators

To probe whether the observed CAPs act as coupled oscillators as we previously described (Gutierrez-Barragan et al., 2018), we computed the GS phase angular difference between CAP occurrences in the same GS cycle or across GS cycles that were immediately adjacent in time (i.e. next or previous GS cycle, **Fig. S3.2**). Keeping with our previous work, we found that GS phase difference between occurrences of the same CAP in control animals (diagonal panels, **Fig. S3.2**) were concentrated around zero, suggesting that a given state appears in general for a short range of adjacent phases during a given cycle. Moreover, reciprocal CAPs appeared with a phase difference of π in the same cycle, suggesting that each GS cycle reflects at least in part the alternation between peaks and troughs of a specific spatially-structured network. Finally, we found significantly, densely concentrated, locked distribution of phase differences between non-reciprocal CAP pairs (e.g. between CAPs 4 and 5, and CAPs 3 and 6). These results replicate our previous findings in **Chapter 2**, by showing that the identified brain-wide functional states act like coupled infra-slow oscillators.

When carried out in xanomeline-treated mice (**Fig. S3.3**), the same analyses revealed that GS phase differences between occurrences of the same CAP (diagonal panels, **Fig. S3.3**) were concentrated around zero. This results suggests that, even though xanomeline-induced states are embedded within GS oscillations in a weaker fashion than under control conditions, they do similarly occur for a short range of adjacent phases during a given GS cycle as well. Albeit with a wider spread of phases as compared with the Vehicle CAPs, reciprocal CAPs under xanomeline appeared with a phase differences near π in the same cycle, suggesting that each GS cycle reflects at least in part the alternation between peaks and troughs of a specific spatially-structured network. There are significant, yet highly spread, locked distribution of GS phase differences between non-reciprocal CAP pairs (e.g. between CAPs 3 and 5, and CAPs 3 and 6). Together with the observation that xanomeline significantly reduces the amplitude of

GS infra-slow oscillations (**Fig 3.5-C**); these findings collectively suggest that the input of xanomeline on selective cholinergic receptors engages the brain in a set of functional states which are weakly coupled to the GS.

3.4 Discussion

Xanomeline targets muscarinic agonist receptors M1 and M4 and has been proposed as a potential cholinergic stimulant of potential therapeutic activity in Alzheimer disease (Avery et al., 1997; Bodick et al., 1997; Si et al., 2010; Wang et al., 2011). . In this study, we show that cholinergic stimulation produced by xanomeline results in large-scale rsfMRI desynchronization (e.g. functional connectivity) and reduced spontaneous low-frequency fluctuations of the BOLD signal. We also show that xanomeline administration results in a set of prototypical functional states characterized by distinctive topology and oscillatory dynamics, and a weaker coupling with infra-slow global fMRI signal oscillations. Our steady-state rsfMRI mapping revealed robust and widespread reduction in within and between network functional connectivity in subjects receiving xanomeline. While the specific electrophysiological correlates of such a decreased rsfMRI synchronization are unknown, this effect is consistent with an increased cholinergic tone, which promotes s arousal and leads to neocortical disinhibition at timescales ranging from tens of milliseconds to several seconds (Poorthuis et al., 2014). It is therefore conceivable that the observed reduction in neocortical rsfMRI connectivity may reflect a transition between slow, synchronized oscillations, to the desynchronized, stochastic discharge that characterizes the aroused state (Lawrence, 2008). Moreover, our results suggest a general disaggregation of recurrent oscillatory brain states with the global fMRI signal (GS), a signature consistent with findings that the GS has reduced power with increasing arousal (Liu et al., 2018; Turchi et al., 2018). Interestingly, xanomeline also produced a noticeable increase in functional connectivity within key-regions of the basal forebrain and the ventro-medial prefrontal cortex. While the origin of these effects remain to be determined, it is interesting to note that the affected regions are very rich in cholinergic nuclei (Li et al., 2017). We speculate that the observed activation may reflect cholinergic-

induced modulation of dopaminergic areas (Bruinsma et al., 2018), or cholinergic disinhibition produced by activation of muscarinic auto-receptors. Independent of the neuromodulatory drivers of these effects, this observation is consistent with a pro-cholinergic action of this compound, and support its use as a pharmacological tool to modulate ascending modulatory systems involved in arousal. Previous findings of spatially opposing state and anti-state configurations of rsfMRI BOLD co-activation in the human brain (see Figure S3 in Liu et al., 2013), and partial recapitulation of our findings using seed-based CAPs in the awake rat (Liang et al., 2015), suggest that the oscillatory patterns we described here are not a direct consequence of the light sedation employed in our measurements, (Deshpande et al., 2010; Greicius et al., 2008; Hutchison et al., 2011; Margulies et al., 2009; Vincent et al., 2007) (see Gozzi and Schwarz, 2016 for a recent review). From a methodological standpoint, a more relevant interpretational caveat for our findings is a possible direct vascular effect of the employed drug. Indeed, cholinergic modulators can affect the vasculature directly, with cholinergic agonists causing vasodilatation and cholinergic antagonists causing vasoconstriction (Sato and Sato, 1995). Moreover, the administration of acetylcholine in muscarinic M5 knock out mice does not produce any vasodilatation in the cerebral vasculature, suggesting that the M5 – receptor subtype is a key mediator of the vasoactive functions of acetylcholine in the brain (Yamada et al., 2003, 2001). As xanomeline acts also as a partial agonist at the M5 receptor, a contribution of direct perivascular effects to the readouts mapped in our study cannot be entirely ruled out (Grant, 2005). Previous evidence of the efficacy of xanomeline in counteracting the behavioral effect of NMDA receptor antagonism MK801 strongly argue against a purely vascular effect of xanomeline (Barak and Weiner, 2011). We also note that, whatever action cholinergic modulation exerts in the awake brain, it is likely to involve analogous vasotonic effects, as these are intrinsically related to the stimulation of neural and perivascular cholinergic receptors. Our results are therefore of translational and mechanistic relevance independent of the specific vascular contribution of xanomeline and cholinergic agonism.

Using scopolamine, a muscarinic acetylcholine receptor antagonist, rsfMRI experiments in mice showed that the agent causes functional connectivity disruption in cingulate and prefrontal regions, an effect that that was prevented by milameline, a cholinergic agonist (Shah

et al., 2015). It is interesting to note that these rsfMRI results data are directionally consistent with the functional desynchronization we observed with xanomeline, despite the seemingly divergent pharmacological profile (antagonist vs. agonist) of these two compounds. However, the complex and composite pre- and post-synaptic distribution of muscarinic receptors does not permit to establish whether scopolamine functionally silence or increase cortical cholinergic tone. So the possibility that scopolamine exerts cholinergic post-synaptic stimulation comparable to that produced by xanomeline cannot be ruled out. In this respect, we also note that oral administration of galantamine, an acethyl–cholinesterase inhibitor, produced mostly decreased functional activity in human testing, an effect consistent with a dominant desynchronizing effect of cholinergic stimulation (Klaassens et al., 2017). This notion is corroborated by an EEG study we performed in the lab, showing that xanomeline robustly induces EEG power across a wide range of bands (data not shown).

A recent study in macaques showed that inactivation with muscimol infusion of the nucleus basalis of Meynert (NBM), the principal source of widespread cholinergic and GABAergic projections to the cortex, produced a prominent ipsilateral decrease in the relative amplitude of cortex-wide spontaneous BOLD fluctuations, without altering static resting state network structure (Turchi et al., 2018). In keeping with these findings, we report a considerable reduction of global fMRI signal fluctuations upon xanomeline administration. This result is consistent with an increasing body of evidence linking arousal to the amplitude of global signal fluctuations (Liu et al., 2018, 2015; Wong et al., 2013). Within this interpretative framework, our findings corroborate a key contribution of cholinergic tone to the control of arousal, and arousal-related neurophysiological signals (Turchi et al., 2018). Our work also provides a first description of the effect of cholinergic modulation on large-scale network dynamics in the mouse brain. We first show that pharmacological stimulation of cholinergic activity produces a significant increase in local BOLD fluctuations of the projecting sites of the basal forebrain, resulting in desynchronization of resting-state network structure. Importantly, we also report that cholinergic stimulation engages brain-wide spontaneous brain activity in a set of unique oscillating network states, involving the contrasting co-activation of posterolateral cortical regions and basal forebrain areas. As expected, the topography of these states substantially

differs from that observed under basal conditions, a finding consistent with the reconfiguration of brain dynamics as a function of arousal levels (Wang et al., 2016).

In conclusion, we document that the M1/M4 receptor-preferring agonist xanomeline induces a widespread decreases functional connectivity in the cortex of the mouse brain, but increases local connectivity of the basal forebrain. We also detected localized decreases in the amplitude of low-frequency fluctuations in key cholinergic receptor sites, while significant increases were found in ascending nuclei of the basal forebrain and hypothalamus. Finally, we document that recurrent states of whole-brain network co-activation are significantly reconfigured upon cholinergic stimulation, involving the recruitment of basal forebrain nuclei as a leading functional system for most of the CAPs. These results document that oscillatory brain states we describe in **Chapter 2** (Gutierrez-Barragan et al., 2018), undergo prominent spatial reconfiguration as a function of modulatory and arousal states, providing the basis for a description of spontaneous brain activity in terms of oscillatory fluctuations of patterns of instantaneous activity that are morphed by internal and external inputs

3.5 Supplementary Information

Supplementary figures

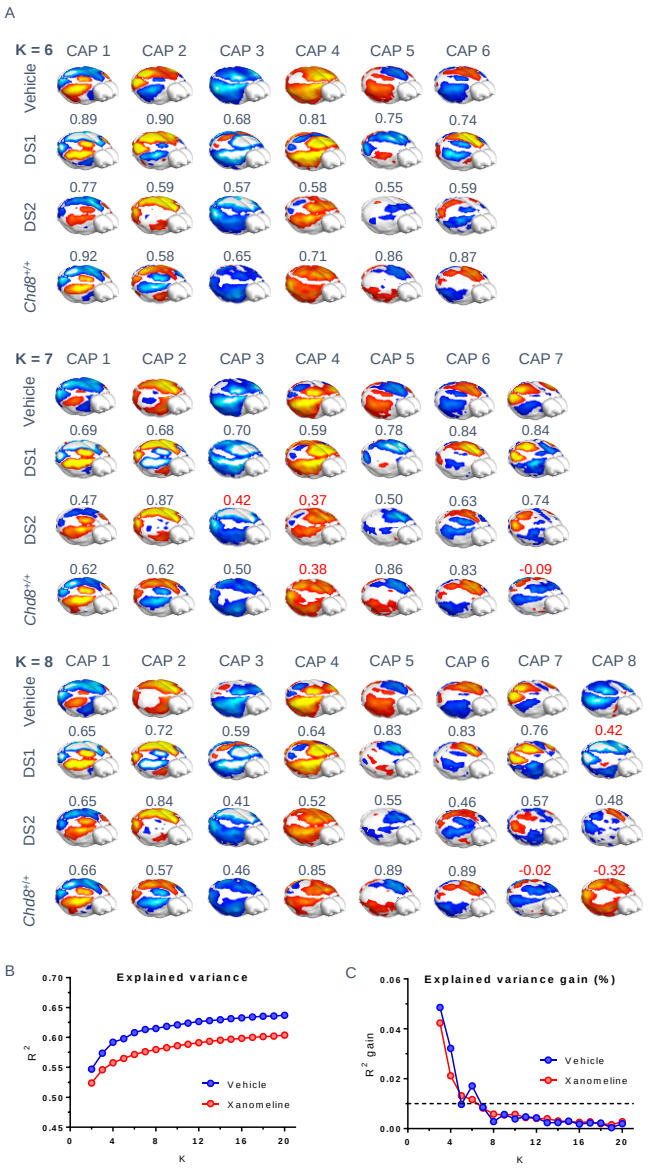

Figure S3.1: Selection of optimal number of clusters. (A) Whole-brain representations of CAPs found with k = 6, 7, and 8 in the Vehicle dataset (n = 19), and their matched CAPs found in dataset 1 (n = 40, 500 fMRI frames per subject), dataset 2 (n = 41, 300 frames per subject) or dataset 3 (CHD8+/+ control mice, n = 23, 450 frames per subject) of Chapter 2. Spatial correlations to the Vehicle dataset are shown above each CAP. Note that CAPs 1-6 are recurrently found in all datasets with k = 7 and 8, while additional CAPs are less reproducible across datasets. (B) Variance explained by clustering dataset 1 with k = 2 – 20. (C) Percentage gain in variance explained when advancing from k-1 to k.

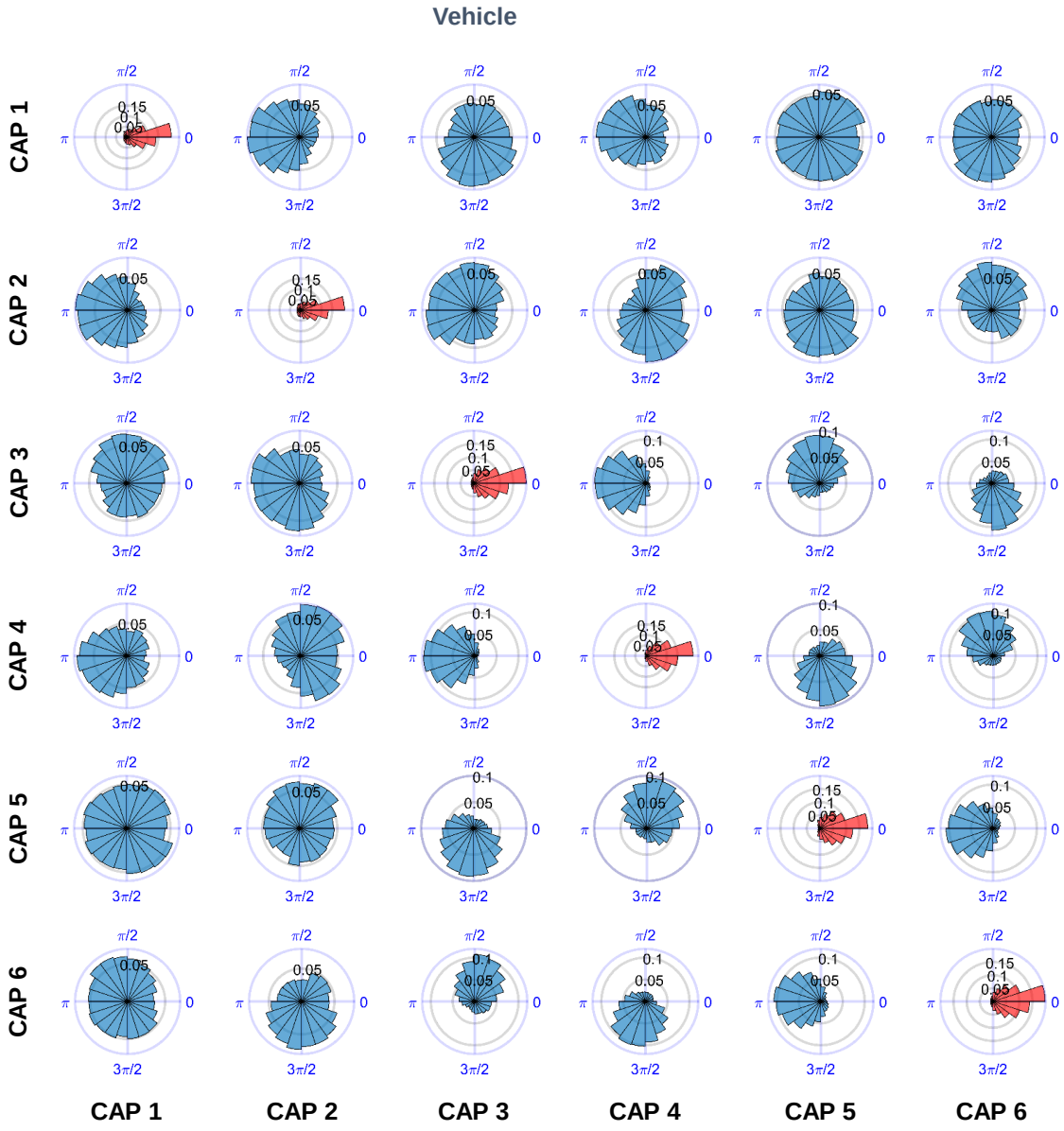

Figure S3.2: Functional states that act as coupled oscillators in control (vehicle) subjects. Global signal phase differences between CAP occurrences. Each panel corresponds to the circular distribution of GS phase differences between occurrences of a CAP inside a GS-cycle (rows), and the occurrences of another CAP within the same cycle and across GS cycles that were immediately adjacent in time (columns). All distributions significantly deviate from circular uniformity (Raleigh test, $p < 0.05$).

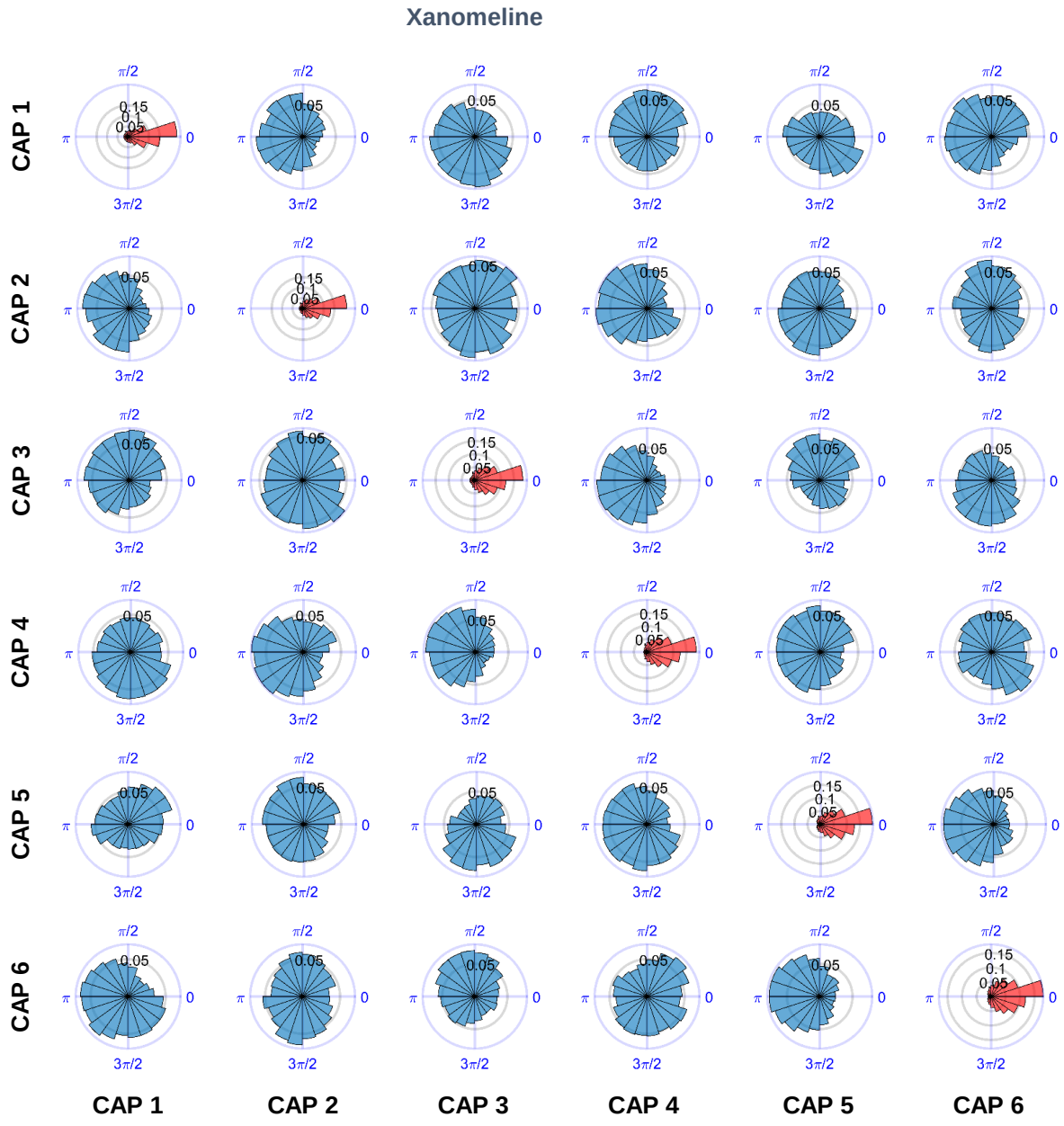

Figure S3.3: Functional states act as coupled oscillators in xanomeline-treated subjects. Global signal phase differences between CAP occurrences. Each panel corresponds to the circular distribution of GS phase differences between occurrences of a CAP inside a GS-cycle (rows), and the occurrences of another CAP within the same cycle and across GS cycles that were immediately adjacent in time (columns). All distributions significantly deviate from circular uniformity (Raleigh test, $p < 0.05$).

Chapter 4
Conclusions

Rodent models and advanced neurogenetic methods offer a comprehensive set of tools to study the central nervous system at different temporal and spatial scales, with unprecedented precision. The possibility of translating human-based measurements of neural activity like rsfMRI can now be exploited to investigate the organizational principles and neural drivers of spontaneous brain activity in the mammalian brain, hence critically informing human researchers on the origin and significance of neural signals widely measured in clinical settings. In this project, we employed mouse rsfMRI datasets to probe the intrinsic dynamics of spontaneous state network activity in the resting brain, and discovered in the process a set of new principles guiding the organization and spatio-temporal organization of rsfMRI network activity.

4.1 Overview of results

The present research project was initially aimed to map brain-wide patterns of dynamic rsfMRI connectivity with voxel-resolution in the mouse brain. To this aim, we devised an optimized an approach for the description of time-varying patterns of spontaneous network activity leveraging recent advances in the description of brain dynamics in terms of co-activation patterns of instantaneous brain activity. Our observation that selective averaging of a few fMRI frames corresponding to peaks in regional BOLD activity reliably maps canonical seed-based correlation maps in the mouse brain (**Fig. 2.1**), a finding recapitulating analogous human rsfMRI mapping (Liu and Duyn, 2013; Tagliazucchi et al., 2012), provided a robust theoretical foundation for our approach. Specifically, we reasoned that recurrent brain states of network activity could be best captured by classifying whole-brain fMRI volumes into homogeneous spatial patterns (CAPs), without a predefined regional selection (seed). We subsequently devised a robust empirical strategy to select recurrent patterns of spontaneous rsfMRI activity

that reliably describe the variance of whole-brain data, resulting in reproducible states across independent datasets. This strategy led to the identification of six dominant states, which can be mapped both at the group, and at the single-subject level. Importantly, by applying this approach we discovered that network transitions involve recurring patterns characterized by opposing BOLD co-activation topographies, and that their dynamic transitions can be effectively described in oscillatory terms. These findings allowed us to probe whether these states were inscribed within a common temporal framework, and found that they occur at specific phases of the global fMRI signal (GS), acting as coupled oscillators. These results also imply that intrinsic oscillations of the fMRI GS may not reflect global, spatially undifferentiated, ups and downs of whole-brain activity, but, on the contrary, each phase of the GS may encompass the specific activation of selected subsets of possible brain states, each characterized by a characteristic profile of brain activity.

We then applied our approach to describe static and dynamic alterations in rsfMRI coupling associated with a prominent autism-associated mutation, namely haploinsufficient for the chromatin remodeling gene Chd8. This mutation recapitulates a major genetic risk factor for autism spectrum disorders (ASD), and is characterized by rsfMRI over-connectivity between hippocampal and motor cortical areas, as assessed with conventional steady-state rsfMRI mapping (Suetterlin et al., 2018). We demonstrated that aberrant patterns of fMRI functional connectivity (Suetterlin et al., 2018) in this genetic model of autism reflect the engagement of non-canonical brain states characterized by altered regional topography and oscillatory dynamics.

By using a pharmacological approach, we finally show that oscillatory patterns of brain activity reconfigure in response to manipulations of ascending modulatory activity. Specifically, we report that the selective muscarinic acetylcholine receptor agonist, xanomeline, desynchronizes neocortical steady-state rsfMRI activity, while increasing fMRI connectivity within the basal forebrain and hypothalamus. This effect was associated with a new set of oscillatory fMRI states involving a prominent recruitment of basal forebrain regions, as the leading recurrent functional system of most CAPs. These states were found to exhibit altered spatio-temporal dynamics and weaker coupling with global fMRI oscillations, in keeping with recent evidence linking arousal states to the fluctuations in globally synchronized spontaneous fMRI activity.

Collectively, our approach reveals a new set of fundamental principles guiding the spatiotemporal organization of resting state fMRI activity, and its disruption in brain disorders such as autism.

4.2 Limitations

All datasets used in this research project were acquired under light sedation, presenting a potential limitation in the translational power of our results to human studies, as most of them are performed in awake subjects. The use of light anesthesia allows for a strict control of motion and physiological state stability, both shown to critically affect stationary as well as dynamic measures of brain connectivity (Parkes et al., 2018). A strict control of motion is also paramount to increase confidence in the use of GS as a physiologically relevant signal, as opposed to a nuisance regressor contaminated by spurious peripheral contributions (Liu et al., 2017; Wong et al., 2013). We also note here that light sedation has been shown to marginally affect resting state network structure in rodents (Gozzi and Schwarz, 2016), and studies in awake humans using other frame-wise approaches have detected putative anti-state patterns (Liu et al., 2013; Yousefi et al., 2018) that, although not described in oscillatory terms, are consistent with our findings and interpretative model. The extension of our approach to human datasets and awake rsfMRI datasets is undergoing.

Another limitation of our studies is the lack of robust neural or electrophysiological measures on regions predominantly involved in the identified co-activation patterns. Concurrent local-field potential (LFP) recordings could help disambiguate the neurophysiological signatures associated with the observed brain states.

4.3 Future directions

Our work points towards three major lines of future investigations. The first entails the use of multi-modal neuroimaging approaches and their combination with advanced neural manipulations, with the aim of pinpointing the neural drivers of the network transitions we described here. Plans to complement our cholinergic measurements with cell-specific

manipulations through optogenetics or chemogenetics are underway in the Gozzi laboratory, with the aim to establish causal links between the activity of specific neural populations and the observed whole-brain patterns of BOLD co-activation, as recently described (Giorgi et al., 2017). This approach could be instrumental to the disambiguation of the role of cell-specific types in orchestrating large-scale network BOLD co-activations and their underlying dynamics.

A second line of investigation is the use of our approach as a sensitive alternative to static rsfMRI mapping to describe altered fMRI coupling in brain connectopathies. In this respect we point out here that the magnitude of statistical differences we found in Chd8 mutants largely exceed those previously described using conventional steady state rsfMRI metrics, e.g. functional connectivity (Suetterlin et al., 2018), paving the way to the sue of these metrics as more reliable and sensitive classifiers of pathological states in humans.

Finally, from a mechanistic point of view, there is increasing interest in developing generative models that can predict the observed large-scale dynamics of the BOLD signal, starting from nodal models of neural population activity (Deco et al., 2015). In **Chapter 2,** we devised an empirical strategy to select a finite set of recurrent CAPs that accounted for a reasonable amount of variance in the data, and were reproducible in independent datasets. Our results could be further complemented by generative models that can describe whole-brain oscillatory states constrained by structural connectivity, providing a comprehensive mechanistic description of the emergence of oscillatory phenomena we describe here.

In summary, our results suggest a set of fundamental principles of whole-brain function as described by rsfMRI in the mouse brain, and lead the way to further experimental and theoretical approaches that can establish causal links between the observed underlying dynamics, and their neural underpinning, which we expect will open the way to refined modelling and descriptions of spontaneous brain dynamics at the whole brain level.

Bibliography

Abreu, R., Leal, A., Figueiredo, P., 2018. EEG-Informed fMRI: A Review of Data Analysis Methods. Front. Hum. Neurosci. 12, 1–23. doi:10.3389/fnhum.2018.00029

Allen, E.A., Damaraju, E., Plis, S.M., Erhardt, E.B., Eichele, T., Calhoun, V.D., 2014. Tracking whole-brain connectivity dynamics in the resting state. Cereb. Cortex 24, 663–676. doi:10.1093/cercor/bhs352

Amico, E., Gomez, F., Di Perri, C., Vanhaudenhuyse, A., Lesenfants, D., Boveroux, P., Bonhomme, V., Brichant, J.F., Marinazzo, D., Laureys, S., 2014. Posterior cingulate cortex-related co-activation patterns: A resting state fMRI study in propofol-induced loss of consciousness. PLoS One 9, 1–9. doi:10.1371/journal.pone.0100012

Andersen, M.B., Fink-Jensen, A., Peacock, L., Gerlach, J., Bymaster, F., Lundbæk, J.A., Werge, T., 2003. The muscarinic M1/M4receptor agonist xanomeline exhibits antipsychotic-like activity in cebus apella monkeys. Neuropsychopharmacology 28, 1168–1175. doi:10.1038/sj.npp.1300151

Arthur, D., Vassilvitskii, S., 2007. K-Means++: the Advantages of Careful Seeding. Proc. eighteenth Annu. ACM-SIAM Symp. Discret. algorithms 1027–1025. doi:10.1145/1283383.1283494

Avery, E.E., Baker, L.D., Asthana, S., 1997. Potential role of muscarinic agonists in Alzheimer's disease. Drugs and Aging 11, 450–459. doi:10.2165/00002512-199711060-00004

Bandettini, P.A., Wong, E.C., Hinks, R.S., Tikofsky, R.S., Hyde, J.S., 1992. Time-course EPI of human brain function during task activation. Magn. Reson. Med. 25, 390–7. doi:10.1002/mrm.1910250220

Barak, S., Weiner, I., 2011. The M1/M4preferring agonist xanomeline reverses amphetamine-, MK801-and scopolamine-induced abnormalities of latent inhibition: Putative efficacy against positive, negative and cognitive symptoms in schizophrenia. Int. J. Neuropsychopharmacol. 14, 1233–1246. doi:10.1017/S1461145710001549

Belloy, M.E., Naeyaert, M., Abbas, A., Shah, D., Vanreusel, V., van Audekerke, J., Keilholz, S.D., Keliris, G.A., Van der Linden, A., Verhoye, M., 2018. Dynamic resting state fMRI analysis in mice reveals a set of Quasi-Periodic Patterns and illustrates their relationship with the global signal. Neuroimage 1–22. doi:10.1016/j.neuroimage.2018.01.075

Berens, P., Baclawski, K., Berens, P., Baclawski, K., 2009. CircStat: A MATLAB Toolbox for Circular Statistics. J. Stat. Softw. 30, 1–3. doi:10.1002/wics.10

Bertero, A., Liska, A., Pagani, M., Parolisi, R., Masferrer, M.E., Gritti, M., Pedrazzoli, M., Galbusera, A., Sarica, A., Cerasa, A., Buffelli, ario, Tonini, R., Buffo, A., Gross, C., Pasqualetti, M., Gozzi, A., 2018. Autism-associated 16p11.2 microdeletion impairs prefrontal functional connectivity in mouse and human. Brain 141, 2055–2065. doi:10.1093/brain/awy111

Biswal, B., Zerrin Yetkin, F., Haughton, V.M., Hyde, J.S., 1995. Functional connectivity in the motor cortex of resting human brain using echo planar mri. Magn. Reson. Med. 34, 537–541. doi:10.1002/mrm.1910340409

Bodick, N.C., Offen, W.W., Levey, A.I., Cutler, N.R., Gauthier, S.G., Satlin, A., Shannon, H.E., Tollefson, G.D., Rasmussen, K., Bymaster, F.P., Hurley, D.J., Potter, W.Z., Paul, S.M., 1997. Agonist, Cognitive Symptoms. Arch. Neurol. 54, 465–473.

Braun, U., Schäfer, A., Walter, H., Erk, S., Romanczuk-Seiferth, N., Haddad, L., Schweiger, J.I., Grimm, O., Heinz, A., Tost, H., Meyer-Lindenberg, A., Bassett, D.S., 2015. Dynamic reconfiguration of frontal brain networks during executive cognition in humans. Proc. Natl. Acad. Sci. 112, 11678–11683. doi:10.1073/pnas.1422487112

Breakspear, M., 2017. Dynamic models of large-scale brain activity. Nat. Neurosci. 20, 340–352. doi:10.1038/nn.4497

Bruinsma, T.J., Sarma, V. V., Oh, Y., Jang, D.P., Chang, S.Y., Worrell, G.A., Lowe, V.J., Jo, H.J., Min, H.K., 2018. The relationship between dopamine neurotransmitter dynamics and the blood-oxygen-level-dependent (BOLD) signal: A review of pharmacological functional magnetic resonance imaging. Front. Neurosci. 12, 1–8. doi:10.3389/fnins.2018.00238

Buckner, R.L., Andrews-Hanna, J.R., Schacter, D.L., 2008. The brain's default network: anatomy, function, and relevance to disease. Ann. N. Y. Acad. Sci. 1124, 1–38. doi:10.1196/annals.1440.011

Buxton, R.B., 2012. Dynamic models of BOLD contrast. Neuroimage 62, 953–961. doi:10.1016/j.neuroimage.2012.01.012

Buzsáki, G., Draguhn, A., 2004. Neuronal olscillations in cortical networks. Science (80-.). 304, 1926–1929. doi:10.1126/science.1099745

Cabral, J., Kringelbach, M.L., Deco, G., 2017a. Functional connectivity dynamically evolves on multiple time-scales over a static structural connectome: Models and mechanisms. Neuroimage 160, 84–96. doi:10.1016/j.neuroimage.2017.03.045

Cabral, J., Vidaurre, D., Marques, P., Magalhães, R., Silva Moreira, P., Miguel Soares, J., Deco, G., Sousa, N., Kringelbach, M.L., 2017b. Cognitive performance in healthy older adults relates to spontaneous switching between states of functional connectivity during rest. Sci. Rep. 7, 5135. doi:10.1038/s41598-017-05425-7

Calhoun, V.D., Adali, T., 2016. Time-Varying Brain Connectivity in fMRI Data: Whole-brain data-driven approaches for capturing and characterizing dynamic states. IEEE Signal Process. Mag. 33, 52–66. doi:10.1109/MSP.2015.2478915

Chang, C., Glover, G.H., 2010. Time-frequency dynamics of resting-state brain connectivity measured with fMRI. Neuroimage 50, 81–98. doi:10.1016/j.neuroimage.2009.12.011

Damoiseaux, J.S., Rombouts, S.A.R.B., Barkhof, F., Scheltens, P., Stam, C.J., Smith, S.M., Beckmann, C.F., 2006. Consistent resting-state networks across healthy subjects. Proc. Natl. Acad. Sci. 103, 13848–13853. doi:10.1073/pnas.0601417103

Deco, G., Tononi, G., Boly, M., Kringelbach, M.L., 2015. Rethinking segregation and integration: contributions of whole-brain modelling. Nat. Rev. Neurosci. 16, 430–439. doi:10.1038/nrn3963

Deshpande, G., Kerssens, C., Sebel, P.S., Hu, X., 2010. Altered local coherence in the default mode network due to sevoflurane anesthesia. Brain Res. 1318, 110–121. doi:10.1016/j.brainres.2009.12.075

Di Martino, A., Yan, G.-G., LI, Q., Denio, E., Castellanos, F.X., Bookheimer, S.Y., Dapretto, M., Deen, B., Delmonte, S., Dinstein, I., Erti-Wagner, B., Fair, D. a, Gallagher, L., Kennedy, D.P., Keown, C.L., Keysers, C., Lainhart, J.E., Lord, C., Luna, B., Menon, V., Minshew, N.J., Monk, C.S., Mueller, S., Mueller, R.-A., Nebel, M.B., Nigg, J.T., O'Hearn, K., Pelphrey, K.A., Peltier, S.J., Rudie, J.D., Sunaert, S., Thioux, M., Tyszka, J.M., Uddin, L.Q., Verhoeven, J.S., Wenderoth, N., Wiggins, J.L., Mostofsky, S.H., Milham, M.P., 2014. The Autism Brain Imaging Data Exchange: towards large-scale evaluation of the intrinseic brain architecture in autism. Mol. Psychiatry 19, 659–667. doi:10.1038/mp.2013.78.The

Ferrari, L., Turrini, G., Crestan, V., Bertani, S., Cristofori, P., Bifone, A., Gozzi, A., 2012. A robust experimental protocol for pharmacological fMRI in rats and mice. J. Neurosci. Methods 204, 9–18. doi:10.1016/j.jneumeth.2011.10.020

Fox, M.D., Raichle, M.E., 2007. Spontaneous fluctuations in brain activity observed with functional magnetic resonance imaging. Nat. Rev. Neurosci. 8, 700–711. doi:10.1038/nrn2201

Fox, M.D., Snyder, A.Z., Vincent, J.L., Corbetta, M., Van Essen, D.C., Raichle, M.E., 2005. From The Cover: The human brain is intrinsically organized into dynamic, anticorrelated functional networks. Proc. Natl. Acad. Sci. 102, 9673–9678. doi:10.1073/pnas.0504136102

Giorgi, A., Migliarini, S., Galbusera, A., Maddaloni, G., Mereu, M., Margiani, G., Gritti, M., Landi, S., Trovato, F., Bertozzi, S.M., Armirotti, A., Ratto, G.M., De Luca, M.A., Tonini, R., Gozzi, A., Pasqualetti, M., 2017. Brain-wide Mapping of Endogenous

Serotonergic Transmission via Chemogenetic fMRI. Cell Rep. 21, 910–918. doi:10.1016/j.celrep.2017.09.087

Glasser, M.F., Smith, S.M., Marcus, D.S., Andersson, J.L.R., Auerbach, E.J., Behrens, T.E.J., Coalson, T.S., Harms, M.P., Jenkinson, M., Moeller, S., Robinson, E.C., Sotiropoulos, S.N., Xu, J., Yacoub, E., Ugurbil, K., Van Essen, D.C., 2016. The Human Connectome Project's neuroimaging approach. Nat. Neurosci. 19, 1175–1187. doi:10.1038/nn.4361

Glerean, E., Salmi, J., Lahnakoski, J.M., Jääskeläinen, I.P., Sams, M., 2012. Functional Magnetic Resonance Imaging Phase Synchronization as a Measure of Dynamic Functional Connectivity. Brain Connect. 2, 91–101. doi:10.1089/brain.2011.0068

Gore, J.C.J.C., 2003. Principles and practice of functional MRI of the human brain. J. Clin. Invest. 112, 4–9. doi:10.1172/JCI200319010.Conventional

Goutte, C., Toft, P., Rostrup, E., Nielsen, F.Å., Hansen, L.K., 1999. On clustering fMRI time-series. Neuroimage 9, 298–310. doi:10.1006/nimg.1998.0391

Gozzi, A., Colavito, V., Seke Etet, P.F., Montanari, D., Fiorini, S., Tambalo, S., Bifone, A., Zucconi, G.G., Bentivoglio, M., 2012. Modulation of fronto-cortical activity by modafinil: A functional imaging and Fos study in the rat. Neuropsychopharmacology 37, 822–837. doi:10.1038/npp.2011.260

Gozzi, A., Schwarz, A.J., 2016. Large-scale functional connectivity networks in the rodent brain. Neuroimage 127, 496–509. doi:10.1016/j.neuroimage.2015.12.017

Grandjean, J., Preti, M.G., Bolton, T.A.W., Buerge, M., Seifritz, E., Pryce, C.R., Van De Ville, D., Rudin, M., 2017. Dynamic reorganization of intrinsic functional networks in the mouse brain. Neuroimage 152, 497–508. doi:10.1016/j.neuroimage.2017.03.026

Grant, M.K.O., 2005. Persistent Binding and Functional Antagonism by Xanomeline at the Muscarinic M5 Receptor. J. Pharmacol. Exp. Ther. 315, 313–319. doi:10.1124/jpet.105.090134

Greicius, M.D., Kiviniemi, V., Tervonen, O., Vainionpää, V., Alahuhta, S., Reiss, A.L., Menon, V., 2008. Persistent default-mode network connectivity during light sedation.

Hum. Brain Mapp. 29, 839–847. doi:10.1002/hbm.20537

Gutierrez-Barragan, D., Basson, M.A., Panzeri, S., Gozzi, A., 2018. Oscillatory brain states govern spontaneous fMRI network dynamics. bioRxiv 393389. doi:10.1101/393389

Havlicek, M., Roebroeck, A., Friston, K., Gardumi, A., Ivanov, D., Uludag, K., 2015. Physiologically informed dynamic causal modeling of fMRI data. Neuroimage 122, 355–372. doi:10.1016/j.neuroimage.2015.07.078

Hindriks, R., Adhikari, M.H., Murayama, Y., Ganzetti, M., Mantini, D., Logothetis, N.K., Deco, G., 2016. Can sliding-window correlations reveal dynamic functional connectivity in resting-state fMRI? Neuroimage 127, 242–256. doi:10.1016/j.neuroimage.2015.11.055

Huster, R.J., Debener, S., Eichele, T., Herrmann, C.S., 2012. Methods for Simultaneous EEG-fMRI: An Introductory Review. J. Neurosci. 32, 6053–6060. doi:10.1523/JNEUROSCI.0447-12.2012

Hutchison, R.M., Leung, L.S., Mirsattari, S.M., Gati, J.S., Menon, R.S., Everling, S., 2011. Resting-state networks in the macaque at 7T. Neuroimage 56, 1546–1555. doi:10.1016/j.neuroimage.2011.02.063

Hutchison, R.M., Womelsdorf, T., Allen, E.A., Bandettini, P.A., Calhoun, V.D., Corbetta, M., Della Penna, S., Duyn, J.H., Glover, G.H., Gonzalez-Castillo, J., Handwerker, D.A., Keilholz, S., Kiviniemi, V., Leopold, D.A., de Pasquale, F., Sporns, O., Walter, M., Chang, C., 2013. Dynamic functional connectivity: Promise, issues, and interpretations. Neuroimage 80, 360–378. doi:10.1016/j.neuroimage.2013.05.079

Jackson, A.F., Bolger, D.J., 2014. The neurophysiological bases of EEG and EEG measurement: A review for the rest of us. Psychophysiology 51, 1061–1071. doi:10.1111/psyp.12283

Jonckers, E., Shah, D., Hamaide, J., Verhoye, M., Van der Linden, A., 2015. The power of using functional fMRI on small rodents to study brain pharmacology and disease. Front. Pharmacol. 6, 1–19. doi:10.3389/fphar.2015.00231

Kaplan, R., Adhikari, M.H., Hindriks, R., Mantini, D., Murayama, Y., Logothetis, N.K., Deco, G., 2016. Hippocampal Sharp-Wave Ripples Influence Selective Activation of the Default Mode Network. Curr. Biol. 26, 686–691. doi:10.1016/j.cub.2016.01.017

Karahanoğlu, F.I., Van De Ville, D., 2015. Transient brain activity disentangles fMRI resting-state dynamics in terms of spatially and temporally overlapping networks. Nat. Commun. 6, 7751. doi:10.1038/ncomms8751

Keilholz, S.D., 2014. Review Article: The Neural Basis of Time-Varying Resting State Functional Connectivity. Brain Connect. 4, 769–779. doi:10.1089/brain.2014.0250

Keilholz, S.D., Pan, W.J., Billings, J., Nezafati, M., Shakil, S., 2017. Noise and non-neuronal contributions to the BOLD signal: applications to and insights from animal studies. Neuroimage 154, 267–281. doi:10.1016/j.neuroimage.2016.12.019

Klaassens, B.L., Rombouts, S.A.R.B., Winkler, A.M., van Gorsel, H.C., van der Grond, J., van Gerven, J.M.A., 2017. Time related effects on functional brain connectivity after serotonergic and cholinergic neuromodulation. Hum. Brain Mapp. 38, 308–325. doi:10.1002/hbm.23362

Kudela, M., Harezlak, J., Lindquist, M.A., 2017. Assessing uncertainty in dynamic functional connectivity. Neuroimage 149, 165–177. doi:10.1016/j.neuroimage.2017.01.056

Kuhn, H.W., 1955. The Hungarian method for the assignment problem. Nav. Res. Logist. Q. 2, 83–97. doi:10.1002/nav.3800020109

Lawrence, J.J., 2008. Cholinergic control of GABA release: emerging parallels between neocortex and hippocampus. Trends Neurosci. 31, 317–327. doi:10.1016/j.tins.2008.03.008

Li, X., Yu, B., Sun, Q., Zhang, Y., Ren, M., Zhang, X., Li, A., Yuan, J., Madisen, L., Luo, Q., Zeng, H., Gong, H., Qiu, Z., 2017. Generation of a whole-brain atlas for the cholinergic system and mesoscopic projectome analysis of basal forebrain cholinergic neurons. Proc. Natl. Acad. Sci. 115, 201703601. doi:10.1073/pnas.1703601115

Liang, Z., Li, T., King, J., Zhang, N., 2013. Mapping thalamocortical networks in rat brain

using resting-state functional connectivity. Neuroimage 83, 237–244. doi:10.1016/j.neuroimage.2013.06.029

Liang, Z., Liu, X., Zhang, N., 2015. Dynamic resting state functional connectivity in awake and anesthetized rodents. Neuroimage 104, 89–99. doi:10.1016/j.neuroimage.2014.10.013

Lindquist, M.A., 2008. The Statistical Analysis of fMRI Data. Stat. Sci. 23, 439–464. doi:10.1214/09-STS282

Liska, A., Bertero, A., Gomolka, R., Sabbioni, M., Galbusera, A., Barsotti, N., Panzeri, S., Scattoni, M.L., Pasqualetti, M., Gozzi, A., 2017. Homozygous Loss of Autism-Risk Gene CNTNAP2 Results in Reduced Local and Long-Range Prefrontal Functional Connectivity. Cereb. Cortex 1–13. doi:10.1093/cercor/bhx022

Liska, A., Galbusera, A., Schwarz, A.J., Gozzi, A., 2015. Functional connectivity hubs of the mouse brain. Neuroimage 115, 281–291. doi:10.1016/j.neuroimage.2015.04.033

Liska, A., Gozzi, A., 2016. Can mouse imaging studies bring order to autism connectivity chaos? Front. Neurosci. 10, 1–8. doi:10.3389/fnins.2016.00484

Liu, T.T., Nalci, A., Falahpour, M., 2017. The global signal in fMRI: Nuisance or Information? Neuroimage 150, 213–229. doi:10.1016/j.neuroimage.2017.02.036

Liu, X., Chang, C., Duyn, J.H., 2013. Decomposition of spontaneous brain activity into distinct fMRI co-activation patterns. Front. Syst. Neurosci. 7, 1–11. doi:10.3389/fnsys.2013.00101

Liu, X., De Zwart, J.A., Schölvinck, M.L., Chang, C., Ye, F.Q., Leopold, D.A., Duyn, J.H., 2018. Subcortical evidence for a contribution of arousal to fMRI studies of brain activity. Nat. Commun. 9, 1–10. doi:10.1038/s41467-017-02815-3

Liu, X., Duyn, J.H.H., 2013. Time-varying functional network information extracted from brief instances of spontaneous brain activity. Proc. Natl. Acad. Sci. 110, 4392–4397. doi:10.1073/pnas.1216856110

Liu, X., Yanagawa, T., Leopold, D.A., Chang, C., Ishida, H., Fujii, N., Duyn, J.H., 2015. Arousal transitions in sleep, wakefulness, and anesthesia are characterized by an orderly sequence of cortical events. Neuroimage 116, 222–231. doi:10.1016/j.neuroimage.2015.04.003

Logothetis, N.K., 2008. What we can do and what we cannot do with fMRI. Nature 453, 869–878. doi:10.1038/nature06976

Logothetis, N.K., Eschenko, O., Murayama, Y., Augath, M., Steudel, T., Evrard, H.C., Besserve, M., Oeltermann, A., 2012. Hippocampal–cortical interaction during periods of subcortical silence. Nature 491, 547–553. doi:10.1038/nature11618

Logothetis, N.K., J, P., M, A., T, T., A, O., 2001. Neurophysiological investigation of thebasis of the fMRI signal. Nature 1–8.

Logothetis, N.K., Wandell, B.A., 2004. Interpreting the BOLD Signal. Annu. Rev. Physiol. 66, 735–769. doi:10.1146/annurev.physiol.66.082602.092845

Majeed, W., Magnuson, M., Hasenkamp, W., Schwarb, H., Schumacher, E.H., Barsalou, L., Keilholz, S.D., 2011. Spatiotemporal dynamics of low frequency BOLD fluctuations in rats and humans. Neuroimage 54, 1140–1150. doi:10.1016/j.neuroimage.2010.08.030

Margulies, D.S., Vincent, J.L., Kelly, C., Lohmann, G., Uddin, L.Q., Biswal, B.B., Villringer, A., Castellanos, F.X., Milham, M.P., Petrides, M., 2009. Precuneus shares intrinsic functional architecture in humans and monkeys. Proc. Natl. Acad. Sci. 106, 20069–20074. doi:10.1073/pnas.0905314106

Matsui, T., Murakami, T., Ohki, K., 2018. Neuronal Origin of the Temporal Dynamics of Spontaneous BOLD Activity Correlation. Cereb. Cortex 1–13. doi:10.1093/cercor/bhy045

Matsui, T., Murakami, T., Ohki, K., 2016. Transient neuronal coactivations embedded in globally propagating waves underlie resting-state functional connectivity. Proc. Natl. Acad. Sci. 113, 6556–6561. doi:10.1073/pnas.1521299113

Melancon, B.J., Tarr, J.C., Panarese, J.D., Wood, M.R., Lindsley, C.W., 2013. Allosteric

modulation of the M1muscarinic acetylcholine receptor: Improving cognition and a potential treatment for schizophrenia and Alzheimer's disease. Drug Discov. Today 18, 1185–1199. doi:10.1016/j.drudis.2013.09.005

Michetti, C., Caruso, A., Pagani, M., Sabbioni, M., Medrihan, L., David, G., Galbusera, A., Morini, M., Gozzi, A., Benfenati, F., Scattoni, M.L., 2017. The Knockout of Synapsin II in Mice Impairs Social Behavior and Functional Connectivity Generating an ASD-like Phenotype. Cereb. Cortex 27, 5014–5023. doi:10.1093/cercor/bhx207

Mirza, N.R., Peters, D., Sparks, R.G., 2006. Xanomeline and the Antipsychotic Potential of Muscarinic Receptor Subtype Selective Agonists. CNS Drug Rev. 9, 159–186. doi:10.1111/j.1527-3458.2003.tb00247.x

Mitra, A., Raichle, M.E., 2016. How networks communicate: Propagation patterns in spontaneous brain activity. Philos. Trans. R. Soc. B Biol. Sci. 371. doi:10.1098/rstb.2015.0546

Mohajerani, M.H., McVea, D.A., Fingas, M., Murphy, T.H., 2010. Mirrored Bilateral Slow-Wave Cortical Activity within Local Circuits Revealed by Fast Bihemispheric Voltage-Sensitive Dye Imaging in Anesthetized and Awake Mice. J. Neurosci. 30, 3745–3751. doi:10.1523/JNEUROSCI.6437-09.2010

Montemurro, M.A., Rasch, M.J., Murayama, Y., Logothetis, N.K., Panzeri, S., 2008. Phase-of-Firing Coding of Natural Visual Stimuli in Primary Visual Cortex. Curr. Biol. 18, 375–380. doi:10.1016/j.cub.2008.02.023

Nasrallah, F.A.A., Tay, H.C., Chuang, K.H., 2014. Detection of functional connectivity in the resting mouse brain. Neuroimage 86, 417–424. doi:10.1016/j.neuroimage.2013.10.025

Ogawa, S., Lee, T.M., Kay, A.R., Tank, D.W., 1990. Brain magnetic resonance imaging with contrast dependent on blood oxygenation. Proc. Natl. Acad. Sci. U. S. A. 87, 9868–72. doi:10.1073/pnas.87.24.9868

Orth, M., Bravo, E., Barter, L., Carstens, E., Antognini, J.F., 2006. The differential effect of halothane and isoflurane on electroencephalogrphic responses to electrical

microstimulation of the reticular formation. Anesth. Analg. 102, 1709–1714. doi:10.1213/01.ane.0000205752.00303.94

Parkes, L., Fulcher, B., Yücel, M., Fornito, A., 2018. An evaluation of the efficacy, reliability, and sensitivity of motion correction strategies for resting-state functional MRI. Neuroimage 171, 415–436. doi:10.1016/j.neuroimage.2017.12.073

Poldrack, R.A., 2012. The future of fMRI in cognitive neuroscience. Neuroimage 62, 1216–1220. doi:10.1016/j.neuroimage.2011.08.007

Poorthuis, R.B., Enke, L., Letzkus, J.J., 2014. Cholinergic circuit modulation through differential recruitment of neocortical interneuron types during behaviour. J. Physiol. 592, 4155–4164. doi:10.1113/jphysiol.2014.273862

Popa, D., Popescu, A.T., Pare, D., 2009. Contrasting Activity Profile of Two Distributed Cortical Networks as a Function of Attentional Demands. J. Neurosci. 29, 1191–1201. doi:10.1523/JNEUROSCI.4867-08.2009

Power, J.D., Schlaggar, B.L., Petersen, S.E., 2014. Studying brain organization via spontaneous fMRI signal. Neuron 84, 681–696. doi:10.1016/j.neuron.2014.09.007

Preti, M.G., Bolton, T.A., Van De Ville, D., 2017. The dynamic functional connectome: State-of-the-art and perspectives. Neuroimage 160, 41–54. doi:10.1016/j.neuroimage.2016.12.061

Raichle, M.E., 2015. The Brain's Default Mode Network. Annu. Rev. Neurosci. 38, 433–447. doi:10.1146/annurev-neuro-071013-014030

Sakoğlu, Ü., Upadhyay, J., Chin, C.L., Chandran, P., Baker, S.J., Cole, T.B., Fox, G.B., Day, M., Luo, F., 2011. Paradigm shift in translational neuroimaging of CNS disorders. Biochem. Pharmacol. 81, 1374–1387. doi:10.1016/j.bcp.2010.12.029

Sato, A., Sato, Y., 1995. Cholinergic Neural Regulation of Regional Cerebral Blood Flow. Alzheimer Dis. Assoc. Disord. doi:10.1097/00002093-199505000-00007

Schwalm, M., Schmid, F., Wachsmuth, L., Backhaus, H., Kronfeld, A., Jury, F.A., Prouvot,

P.H., Fois, C., Albers, F., Van Alst, T., Faber, C., Stroh, A., 2017. Cortex-wide BOLD fMRI activity reflects locally-recorded slow oscillation-associated calcium waves. Elife 6, 1–27. doi:10.7554/eLife.27602

Schwarz, A.J., Gozzi, A., Reese, T., Heidbreder, C.A., Bifone, A., 2007. Pharmacological modulation of functional connectivity: the correlation structure underlying the phMRI response to d-amphetamine modified by selective dopamine D3receptor antagonist SB277011A. Magn. Reson. Imaging 25, 811–820. doi:10.1016/j.mri.2007.02.017

Sejnowski, T.J., Churchland, P.S., Movshon, J.A., 2014. Putting big data to good use in neuroscience. Nat. Neurosci. 17, 1440–1441. doi:10.1038/nn.3839

Sforazzini, F., Bertero, A., Dodero, L., David, G., Galbusera, A., Scattoni, M.L., Pasqualetti, M., Gozzi, A., 2016. Altered functional connectivity networks in acallosal and socially impaired BTBR mice. Brain Struct. Funct. 221, 941–954. doi:10.1007/s00429-014-0948-9

Sforazzini, F., Schwarz, A.J., Galbusera, A., Bifone, A., Gozzi, A., 2014. Distributed BOLD and CBV-weighted resting-state networks in the mouse brain. Neuroimage 87, 403–415. doi:10.1016/j.neuroimage.2013.09.050

Shah, D., Blockx, I., Guns, P.J., De Deyn, P.P., Van Dam, D., Jonckers, E., Delgado y Palacios, R., Verhoye, M., Van der Linden, A., 2015. Acute modulation of the cholinergic system in the mouse brain detected by pharmacological resting-state functional MRI. Neuroimage 109, 151–159. doi:10.1016/j.neuroimage.2015.01.009

Shannon, H.E., Hart, J.C., Bymaster, F.P., Calligaro, D.O., DeLapp, N.W., Mitch, C.H., Ward, J.S., Fink-Jensen, A., Sauerberg, P., Jeppesen, L., Sheardown, M.J., Swedberg, M.D.B., 1999. Muscarinic Receptor Agonists, Like Dopamine Receptor Antagonist Antipsychotics, Inhibit Conditioned Avoidance Response in Rats. J. Pharmacol. Exp. Ther. 290, 901 LP-907.

Shannon, H.E., Rasmussen, K., Bymaster, F.P., Hart, J.C., Peters, S.C., Swedberg, M.D.B., Jeppesen, L., Sheardown, M.J., Sauerberg, P., Fink-Jensen, A., 2000. Xanomeline, an M1/M4 preferring muscarinic cholinergic receptor agonist, produces antipsychotic-like

activity in rats and mice. Schizophr. Res. 42, 249–259. doi:10.1016/S0920-9964(99)00138-3

Shine, J.M., Koyejo, O., Bell, P.T., Gorgolewski, K.J., Gilat, M., Poldrack, R.A., 2015. Estimation of dynamic functional connectivity using Multiplication of Temporal Derivatives. Neuroimage 122, 399–407. doi:10.1016/j.neuroimage.2015.07.064

Si, W., Zhang, X., Niu, Y., Yu, H., Lei, X., Chen, H., Cao, X., 2010. A novel derivative of xanomeline improves fear cognition in aged mice. Neurosci. Lett. 473, 115–119. doi:10.1016/j.neulet.2010.02.031

Stanhope, K.J., Mirza, N.R., Bickerdike, M.J., Bright, J.L., Harrington, N.R., Hesselink, M.B., Kennett, G. a, Lightowler, S., Sheardown, M.J., Syed, R., Upton, R.L., Wadsworth, G., Weiss, S.M., Wyatt, a, 2001. The muscarinic receptor agonist xanomeline has an antipsychotic-like profile in the rat. J. Pharmacol. Exp. Ther. 299, 782–792.

Suetterlin, P., Hurley, S., Mohan, C., Riegman, K.L.H., Pagani, M., Caruso, A., Ellegood, J., Galbusera, A., Crespo-Enriquez, I., Michetti, C., Yee, Y., Ellingford, R., Brock, O., Delogu, A., Francis-West, P., Lerch, J.P., Scattoni, M.L., Gozzi, A., Fernandes, C., Basson, M.A., 2018. Altered neocortical gene expression, brain overgrowth and functional over-connectivity in chd8 haploinsufficient mice. Cereb. Cortex 28, 2192–2206. doi:10.1093/cercor/bhy058

Tagliazucchi, E., Balenzuela, P., Fraiman, D., Chialvo, D.R., 2012. Criticality in large-scale brain fmri dynamics unveiled by a novel point process analysis. Front. Physiol. 3 FEB, 1–12. doi:10.3389/fphys.2012.00015

Tagliazucchi, E., Siniatchkin, M., Laufs, H., Chialvo, D.R., 2016. The voxel-wise functional connectome can be efficiently derived from co-activations in a sparse spatio-temporal point-process. Front. Neurosci. 10, 1–13. doi:10.3389/fnins.2016.00381

Thompson, G.J., Riedl, V., Grimmer, T., Drzezga, A., Herman, P., Hyder, F., 2016. The Whole-Brain “Global” Signal from Resting State fMRI as a Potential Biomarker of Quantitative State Changes in Glucose Metabolism. Brain Connect. 6, 435–447.

doi:10.1089/brain.2015.0394

Turchi, J., Chang, C., Ye, F.Q., Russ, B.E., Yu, D.K., Cortes, C.R., Monosov, I.E., Duyn, J.H., Leopold, D.A., 2018. The Basal Forebrain Regulates Global Resting-State fMRI Fluctuations. Neuron 97, 940–952.e4. doi:10.1016/j.neuron.2018.01.032

Vanni, M.P., Chan, A.W., Balbi, M., Silasi, G., Murphy, T.H., 2017. Mesoscale Mapping of Mouse Cortex Reveals Frequency-Dependent Cycling between Distinct Macroscale Functional Modules. J. Neurosci. 37, 7513–7533. doi:10.1523/JNEUROSCI.3560-16.2017

Vincent, J.L., Patel, G.H., Fox, M.D., Snyder, A.Z., Baker, J.T., Van Essen, D.C., Zempel, J.M., Snyder, L.H., Corbetta, M., Raichle, M.E., 2007. Intrinsic functional architecture in the anaesthetized monkey brain. Nature 447, 83–86. doi:10.1038/nature05758

Wang, C., Ong, J.L., Patanaik, A., Zhou, J., Chee, M.W.L., 2016. Spontaneous eyelid closures link vigilance fluctuation with fMRI dynamic connectivity states. Proc. Natl. Acad. Sci. 113, 9653–9658. doi:10.1073/pnas.1523980113

Wang, D., Yang, L., Su, J., Niu, Y., Lei, X., Xiong, J., Cao, X., Hu, Y., Mei, B., Hu, J.F., 2011. Attenuation of neurodegenerative phenotypes in Alzheimer-like presenilin 1/presenilin 2 conditional double knockout mice by EUK1001, a promising derivative of xanomeline. Biochem. Biophys. Res. Commun. 410, 229–234. doi:10.1016/j.bbrc.2011.05.120

Wehling, M., 2011. Drug development in the light of translational science: Shine or shade? Drug Discov. Today 16, 1076–1083. doi:10.1016/j.drudis.2011.07.008

Wong, C.W., Olafsson, V., Tal, O., Liu, T.T., 2013. The amplitude of the resting-state fMRI global signal is related to EEG vigilance measures. Neuroimage 83, 983–990. doi:10.1016/j.neuroimage.2013.07.057

Woo, C.W., Chang, L.J., Lindquist, M.A., Wager, T.D., 2017. Building better biomarkers: Brain models in translational neuroimaging. Nat. Neurosci. 20, 365–377. doi:10.1038/nn.4478

Xiao, D., Vanni, M.P., Mitelut, C.C., Chan, A.W., Ledue, J.M., Xie, Y., Chen, A.C.N., Swindale, N. V., Murphy, T.H., 2017. Mapping cortical mesoscopic networks of single spiking cortical or sub-cortical neurons. Elife 6, 1–28. doi:10.7554/eLife.19976

Yamada, M., Basile, A.S., Fedorova, I., Zhang, W., Duttaroy, A., Cui, Y., Lamping, K.G., Faraci, F.M., Deng, C.X., Wess, J., 2003. Novel insights into M5muscarinic acetylcholine receptor function by the use of gene targeting technology. Life Sci. 74, 345–353. doi:10.1016/j.lfs.2003.09.022

Yamada, M., Lamping, K.G., Duttaroy, A., Zhang, W., Cui, Y., Bymaster, F.P., McKinzie, D.L., Felder, C.C., Deng, C.X., Faraci, F.M., Wess, J., 2001. Cholinergic dilation of cerebral blood vessels is abolished in M(5) muscarinic acetylcholine receptor knockout mice. Proc. Natl. Acad. Sci. U. S. A. 98, 14096–101. doi:10.1073/pnas.251542998

Yeo, B.T.T., Krienen, F.M., Sepulcre, J., Sabuncu, M.R., Lashkari, D., Hollinshead, M., Roffman, J.L., Smoller, J.W., Zollei, L., Polimeni, J.R., Fischl, B., Liu, H., Buckner, R.L., 2011. The organization of the human cerebral cortex estimated by intrinsic functional connectivity. J. Neurophysiol. 106, 1125–1165. doi:10.1152/jn.00338.2011.

Yousefi, B., Shin, J., Schumacher, E.H., Keilholz, S.D., 2018. Quasi-periodic patterns of intrinsic brain activity in individuals and their relationship to global signal. Neuroimage 167, 297–308. doi:10.1016/j.neuroimage.2017.11.043

Zerbi, V., Grandjean, J., Rudin, M., Wenderoth, N., 2015. Mapping the mouse brain with rs-fMRI: An optimized pipeline for functional network identification. Neuroimage 123, 11–21. doi:10.1016/j.neuroimage.2015.07.090

Zou, Q.H., Zhu, C.Z., Yang, Y., Zuo, X.N., Long, X.Y., Cao, Q.J., Wang, Y.F., Zang, Y.F., 2008. An improved approach to detection of amplitude of low-frequency fluctuation (ALFF) for resting-state fMRI: Fractional ALFF. J. Neurosci. Methods 172, 137–141. doi:10.1016/j.jneumeth.2008.04.012